Volume 1, Number 1, June 2010 ISSN 1847-6996

ETFOS
FACULTY OF ELECTRICAL ENGINEERING
Josip Juraj Strossmayer University of Osijek

IJECES International Journal of Electrical and Computer Engineering Systems

International Journal of Electrical and Computer Engineering Systems

ISSN: 1847-6996

INTERNATIONAL JOURNAL OF ELECTRICAL AND COMPUTER ENGINEERING SYSTEMS

Published by Faculty of Electrical Engineering, Josip Juraj Strossmayer University of Osijek, Croatia.

Osijek Croatia | Volume 1, Number 1, June 2010 | Pages 1-54

CONTACT
International Journal of Electrical and Computer Engineering Systems (IJECES)

Faculty of Electrical Engineering,
Josip Juraj Strossmayer
University of Osijek, Croatia

Kneza Trpimira 2b
31000 Osijek, Croatia
Phone: +38531224600
Fax: +38531224605
e-mail: ijeces@etfos.hr

PUBLISHER
Faculty of Electrical Engineering,
Josip Juraj Strossmayer
University of Osijek, Croatia.

Print:

Grafika d.o.o.
Grafičko nakladnička djelatnost
Strossmayerova 295, 31000 Osijek, Croatia
Tel: +385 31/310-300
Tel/Fax: +385 31/310-303

All papers published in the journal have been reviewed.

Journal is referred in:
to be announced.

Bibliographic Information
Commenced in 2010.
ISSN: 1847-6996
e-ISSN: 1847-7003
Published: semiannually
Circulation: 300

IJECES online
http://www.etfos.hr/ijeces

Subscription Information

The annual subscription rate is 50€ for individuals, 25€ for students and 150€ for libraries.

Subscriptions are payable to:

Faculty of Electrical Engineering,
Josip Juraj Strossmayer
University of Osijek, Croatia.
Kneza Trpimira 2b
31000 Osijek, Croatia
Giro account: 2390001 - 1100016777,
Croatian Postal Bank

TABLE OF CONTENTS

EDITORIAL PREFACE

Integrodifferential Equations for Multiscale Wavelet Shrinkage: The Discrete Case 1
Stephan Didas | Gabriele Steidl | Joachim Weickert

Advanced Scientific Visualization, a Multidisciplinary Technology Based on Engineering and Computer Science..... 19
Dean Vučinić

Radiation Pattern of Waveguide Antenna Arrays on Spherical Surface - Experimental Results..... 31
Slavko Rupčić | Vanja Mandrić | Davor Vinko

WSN Implementation in the Greenhouse Environment Using Mobile Measuring Station 37
Simon János | Goran Martinović | István Matijevics

Power Loss Minimizing Control of Cascaded Multilevel Inverter with Efficient Hybrid Carrier Based Space Vector Modulation..... 45
Chinnathambi Govindaraju | Kaliaperumal Baskaran

About this Journal 54

IJECES Copyright Transfer Form

EDITORIAL PREFACE

Welcome to the inaugural issue of the International Journal of Electrical and Computer Engineering Systems (IJECES). The journal is published by the Faculty of Electrical Engineering, Josip Juraj Strossmayer University of Osijek. Through synergy, over the past 30 years of scientific, professional and educational activities, Faculty of Electrical Engineering in Osijek has been a significant institution in the field of research and higher education with 140 employees, out of whom there are more than 90 researchers, more than 20 associates, and more than 2300 students enrolled in 8 courses of study in the fields of electrical and computer engineering, including Bachelor and Master level study programs, postgraduate specialist study programs, and PhD study programs. Participation in numerous scientific and professional research activities and projects, international cooperation with about 25 scientific and research institutions in Croatia and abroad, and the knowledge that, in addition to application, publication of research results plays a very important role in scientific-research work, were the reasons taken into consideration in the establishment of our journal.

The International Journal of Electrical and Computer Engineering Systems publishes original scientific research in the form of full papers, case studies, reviews and surveys. It covers theory and application of electrical and computer engineering, synergy of computer systems and computational methods with electrical and electronic systems, as well as interdisciplinary research. Topics of interest include, but are not limited to: Power systems, Renewable electricity production, Power electronics, Electrical drives, Industrial electronics, Communication systems, Advanced modulation techniques, RFID devices and systems, Signal and data processing, Image processing, Multimedia systems, Microelectronics, Instrumentation and measurement, Control systems, Robotics, Modeling and simulation, Modern computer architectures, Computer networks, Embedded systems, High-performance computing, Parallel and distributed computer systems, Human-computer systems, Intelligent systems, Multi-agent and holonic systems, Real-time systems, Software engineering, Internet and web applications and systems, Applications of computer systems in engineering and related disciplines, Mathematical models of engineering systems, Engineering management, and Engineering education.

With the inaugural issue and our first five articles therein, we encompassed many different topics in the field of electrical and computer engineering systems. The first article, by S. Didas, G. Steidl and J. Weickert, investigates the relations between wavelet shrinkage and integro-differential equations for image simplification and denoising in a discrete case. Authors extend ideas that a wavelet transform can be understood as a derivative operator in connection with convolution with a smoothing kernel. By using tensor product wavelets and special shrinkage rules, this approach is extended to more than one spatial dimension. The second article, by D. Vučinić, addresses scientific visualization and corresponding tools which, by combined use, eliminate many well known problems of sharing, accessing and exchanging design models and the related information content. It is shown that object-oriented methodology is a well adapted approach to stream the software development process of future engineering applications. In the third article, by S. Rupčić, V. Mandrić and D. Vinko, the radiation pattern of two experimental models of circular waveguide antenna arrays on spherical surface is obtained experimentally and compared with theoretical patterns. Analysis was made by means of the developed moment method (MoM) program. The fourth article, by S. Janos, G. Martinović and I. Matijevics, describes a wireless sensor networks system in greenhouse environment. Developed and optimized autonomous measuring robot system and algorithms enable monitoring of all necessary parameters for creating optimal environment in the greenhouse. The fifth article, by C. Govindaraju and K. Baskaran, discusses a power loss minimization technique for a cascaded multilevel inverter using a hybrid carrier based space vector modulation. This article combines the features of carrier based space vector modulation and the fundamental frequency modulation strategy and this is implemented by using a DSP and a CPLD. The inverter offers lower harmonic distortion and operates with equal thermal stress among the power devices.

Finally, I would like to thank the authors for their valuable contributions and the reviewers for their time and efforts in providing many valuable suggestions and comments. We believe that with the joint efforts IJECES will become a recognizable point of reference when it comes to publication of research results.

This inaugural issue of IJECES is dedicated to the 32nd anniversary of the Faculty of Electrical Engineering, a constituent part of Josip Juraj Strossmayer University of Osijek.

Editors-in-Chief:

Radoslav Galić
Goran Martinović

Integrodifferential Equations for Multiscale Wavelet Shrinkage: The Discrete Case

Stephan Didas
Fraunhofer-Institut für Techno- und Wirtschaftsmathematik (ITWM)
Abteilung Bildverar-beitung, D-67663 Kaiserslautern, Germany
stephan.didas@itwm.fraunhofer.de

Gabriele Steidl
Faculty of Mathematics and Computer Science
University of Mannheim, D-68131 Mannheim, Germany
steidl@math.uni-mannheim.de

Joachim Weickert
Mathematical Image Analysis Group, Department of Mathematics and Computer Science
Saarland University, D-66041 Saarbrücken, Germany
weickert@mia.uni-saarland.de

Abstract *– We investigate the relations between wavelet shrinkage and integrodifferential equations for image simplification and denoising in the discrete case. Previous investigations in the continuous one-dimensional setting are transferred to the discrete multidimentional case. The key observation is that a wavelet transform can be understood as a derivative operator in connection with convolution with a smoothing kernel. In this paper, we extend these ideas to a practically relevant discrete formulation with both orthogonal and biorthogonal wavelets. In the discrete setting, the behaviour of smoothing kernels for different scales is more complicated than in the continuous setting and of special interest for the understanding of the filters. With the help of tensor product wavelets and special shrinkage rules, the approach is extended to more than one spatial dimension. The results of wavelet shrinkage and related integrodifferential equations are compared in terms of quality by numerical experiments.*

Keywords *– Image denoising, wavelet shrinkage, integrodifferential equations*

1. INTRODUCTION

Since the beginning of the 1990s, wavelet shrinkage and nonlinear diffusion filtering are two established classes of methods for signal and image simplication and denoising [36, 12, 27, 38].

The idea behind wavelet shrinkage is to denoise an image by performing very simple pointwise operations in a suitable multiresolution representation of the data [36]. This representation is obtained by using the wavelet transform. Depending on the application, the use of different types of wavelets might be suitable. Via the concept of multiresolution analysis [19, 20, 22] the shrinkage technique is closely related to earlier signal processing methods like filter banks and subband coding [5, 6, 23, 29, 34, 33].

Nonlinear diffusion filtering simplifies and denoises an image by solving a partial dierential equation which is typically done without changing the spatial representation of the image. In this setting, first or higher order derivatives of the image are used to formalise the desired smoothness and to detect and eliminate the noise [27, 38, 18, 10].

The close relationship between both methods is emphasized, for example, by the fact that wavelet shrinkage can also be understood as energy minimisation [3, 4, 2]. This fact already relates it to the context of scale-spaces [16, 40, 27, 1] and methods based on partial differential equations (PDEs). In the discrete setting, translationally invariant wavelet shrinkage on the finest scale is even equivalent to total variation regularization and diffusion [30].

The connections between multiscale wavelet shrinkage and corresponding integrodifferential equations in the continuous one-dimensional setting have been the topic of an earlier publication by the authors [9]. The

goal of this paper is to transfer the ideas and results from the continuous to the practically relevant discrete setting. Since the dilation operation on the wavelets can only be approximated on a discrete grid, the formulation is slightly more technical here. Moreover, we will not restrict ourselves to orthogonal wavelets, but also have a look at biorthogonal ones allowing for more general integrodifferential equations. Preliminary results concerning this transfer have been presented at a conference [8]. In addition, we will transfer the one-dimensional case to two dimensions using tensor product wavelets and special shrinkage rules to increase rotational invariance. We also discuss in detail the behavior of the appearing smoothing kernels at different scales. Numerical experiments will be shown to compare the resulting methods in terms of denoising quality.

This paper is organised as follows: Section 2 introduces some notations used throughout the paper. Sections 3 and 4 describe classical wavelet shrinkage and nonlinear diffusion filtering in a discrete setting. The factorisation of a discrete wavelet into a convolution kernel and a derivative approximation is derived in Section 5. In Section 6, this idea is used to derive relations between discrete wavelet shrinkage and integrodifferential equations. Section 7 shows how these ideas can be generalised two higher dimensions. Numerical experiments in Section 8 display the behaviour of the presented filters in practice. The paper is concluded with a summary in Section 9.

2. PRELIMINARIES AND NOTATIONS

Let us start with the notations used throughout this paper. Let

$$f \in \ell^2(Z) := \{(f_n)_{n\in Z} \mid \sum_{n=-\infty}^{\infty} f_n^2 < \infty\} \tag{1}$$

be a real signal of infinite length. Then

$$\hat{f}(\omega) := \sum_{n=-\infty}^{\infty} f_n \exp(-in\xi)$$
$$\text{and} \quad F(z) := \sum_{n=-\infty}^{\infty} f_n z^{-n} \tag{2}$$

denote the *Fourier-* and *the z-transform* of *f*, respectively. The importance of the z-transform in this context results from the fact that it allows for an easy formulation of convolutions as multiplications of formal Laurent series. More precisely, the k-th component of the *convolution a * f* given by

$$(a * f)_k := \sum_{j\in Z} a_j f_{k-j} \tag{3}$$

corresponds to the coefficient of z^{-k} in *A(z)F(z)*.

In practice, we will work with signals of finite length *N* and assume *N*-periodic extensions of the signals. Then the *k*-th component of the cyclic convolution *a * f* of vectors $a, f \in R^N$ given by

$$(a * f)k := \sum_{j=0}^{N-1} a_j f(k-j) \bmod N \tag{4}$$

corresponds to the coefficient of z^{-k} in A(z)F(z) mod $z^N - 1$. On the other hand, the cyclic convolution of $a, f \in R^N$ can be expressed as multiplication of f with the circulant matrix corresponding to a [15]:

$$A := \begin{pmatrix} a_0 & a_1 & a_2 & \dots & a_{N-1} \\ a_{N-1} & a_0 & a_1 & \dots & a_{N-2} \\ a_{N-2} & a_{N-1} & a_0 & \dots & a_{N-3} \\ \vdots & \vdots & \vdots & \ddots & \vdots \\ a_1 & a_2 & a_3 & \dots & a_0 \end{pmatrix} \in R^{N,N}. \tag{5}$$

Each circulant matrix can be written as

$$A := \sum_{j=0}^{N-1} a_j C^j,$$
$$\text{where} \quad C := \begin{pmatrix} 0 & 1 & 0 & \dots & 0 \\ 0 & 0 & 1 & \dots & 0 \\ \vdots & \vdots & \vdots & \ddots & \vdots \\ 0 & 0 & 0 & \dots & 1 \\ 1 & 0 & 0 & \dots & 0 \end{pmatrix} \tag{6}$$

denotes the so-called *basic circulant permutation matrix*. Multiplication with *C* performs a periodic left-shift of a vector.

In the following we will often use some vector $a \in R^N$ in connection with its corresponding *N*-dimensional circulant matrix $A = \sum_{j=0}^{N-1} a_j C^j$ and its **z**-transform $A(z) = \sum_{j=0}^{N-1} a_j z^{-j}$. Circulant N x N-matrices can be diagonalised by the same matrix, namely the *N*-th Fourier matrix. Hence, multiplication of circulant matrices is commutative.

3. DISCRETE WAVELET SHRINKAGE

In this section, we review the three steps of wavelet shrinkage in the discrete setting [36]: Figure 1 shows the corresponding filter bank for wavelet shrinkage on the finest scale, where the z-transform notation of the filters is used.

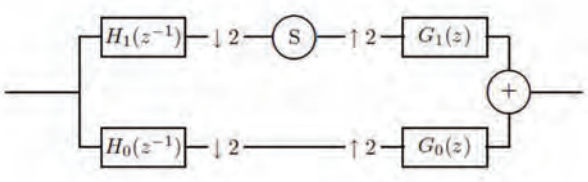

Fig. 1. Filter bank for wavelet shrinkage on the finest scale.

1. Analysis: In the analysis step, the initial signal is transferred to a wavelet coefficient representation. This decomposition is done with the help of the analysis filters h_0 and h_1 which can be obtained as scaling coefficients of the corresponding scaling function. Filters h_0 and h_1 play the role of a low-pass filter and the corresponding high-pass filter, respectively. In addition, both channels are sampled down by leaving out all components with an odd index. This is indicated in the filter bank with the symbol $\downarrow 2$.

2. Shrinkage: The wavelet coefficients of the signal are shrunken towards zero in this step while the low-frequency components are kept. This is modelled as applying a nonlinear *shrinkage function* $\mathrm{S}: \mathrm{R} \to \mathrm{R}$ to each of the wavelet coefficients.

3. Synthesis: In this step, the resulting signal is synthesised from the wavelet coefficients. First, upsampling is used by introducing zeros between each pair of neighbouring signal components. This is written as $\uparrow 2$ here. For the synthesis, the filter pair g_0 and g_1 is used.

We note that the analysis filters h_0 and h_1 are mirrored in our notation. To ensure a perfect reconstruction of the signal, the analysis and the synthesis filters have to satisfy the following properties, [35, 31, 21]:

$$\mathrm{G}_0(\mathrm{z})\mathrm{H}_0(\mathrm{z}^{-1}) + \mathrm{G}_1(\mathrm{z})\mathrm{H}_1(\mathrm{z}^{-1}) \tag{7}$$

$$\mathrm{G}_0(\mathrm{z})\mathrm{H}_0(-\mathrm{z}^{-1}) + \mathrm{G}_1(\mathrm{z})\mathrm{H}_1(-\mathrm{z}^{-1}) \tag{8}$$

For filters of finite length, one can further show (see [35, p. 120] or [21, Theorem 7.9], for example) that there are numbers $\alpha \neq 0$ and $\mathrm{k} \in \mathrm{Z}$ such that

$$\mathrm{G}_0(\mathrm{z}) = \frac{2}{\alpha}\mathrm{z}^{2\mathrm{k}+1}\mathrm{H}_1(-\mathrm{z}^{-1})$$
$$\text{and} \quad \mathrm{G}_1(\mathrm{z}) = -\frac{2}{\alpha}\mathrm{z}^{2\mathrm{k}+1}\mathrm{H}_0(-\mathrm{z}^{-1}). \tag{9}$$

For simplicity, without loss of generality, we assume that $\alpha = 2$ and $k = 0$. This gives us simple relations between analysis and synthesis filters:

$$\mathrm{G}_0(\mathrm{z}) = \mathrm{z}\mathrm{H}_1(-\mathrm{z}^{-1}),\ \mathrm{G}_1(\mathrm{z}) = -\mathrm{z}\mathrm{H}_0(-\mathrm{z}^{-1}). \tag{10}$$

It immediately follows that

$$\mathrm{H}_0(\mathrm{z}) = \mathrm{z}\mathrm{G}_1(-\mathrm{z}^{-1}). \tag{11}$$

These equations hold for the general biorthogonal case with filters of finite length. In order to have orthonormal filters, we have an additional requirement that

$$\mathrm{G}_\mathrm{i}(\mathrm{z}) = \mathrm{H}_\mathrm{i}(\mathrm{z}) \ \text{ for } \ \mathrm{i} \in \{0, 1\} \tag{12}$$

which allows us to determine all four filters with one prototype.

To make wavelet methods compatible to PDE approaches we need a translation invariant wavelet shrinkage process. This can be obtained by skipping the down- and up-sampling procedure as shown in Figure 1. For the synthesis, the result has to be multiplied by 1/2 at each scale. This is also known as *algorithme à trous*, cf. Holschneider et al. [14, 21]. We see that the analysis and synthesis filters are widened by inserting zeros into the filters

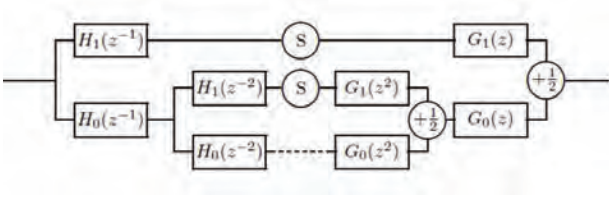

Fig. 2. Filter bank for translational invariant wavelet shrinkage with multiple scales using the algorithme à trous

4. DISCRETE HIGHER ORDER NONLINEAR DIFFUSION

Next, let us have a look at discretisations of nonlinear diffusion which we will need in this section.

Here we use a discretisation of the nonlinear higher order diffusion equation

$$\partial_\mathrm{t}\mathrm{u} = (-1)^{\mathrm{p}+1}\partial_\mathrm{x}^\mathrm{p}\mathrm{g}((\partial_\mathrm{x}^\mathrm{p}\mathrm{u})^2)\partial_\mathrm{x}^\mathrm{p}\mathrm{u} \tag{13}$$

with initial condition $\mathrm{u}(\cdot, 0) = \mathrm{f}$ as described in [10, 11], for example. Here, $\partial_\mathrm{x}^\mathrm{p}$ denotes the partial derivative of order *p* with respect to the variable *x*.

We restrict our attention to *N*-periodic signals on the interval [0, *N* - 1]. To discretise this equation, we consider the sampled version $\mathrm{u} \in \mathrm{R}^\mathrm{N}$ of *u* at an equidistant grid {*jh* : *j* = 0, ..., *N* - 1} with spatial step size *h* = 1.

To approximate the spatial derivatives in (13), we use a forward difference as approximation of the first derivative. It can be expressed in matrix-vector form as $\partial_\mathrm{x} \sim \mathrm{Du}$, where

$$\mathrm{D} := \begin{pmatrix} -1 & 1 & 0 & \dots & 0 \\ 0 & -1 & 1 & \dots & 0 \\ \vdots & \ddots & \ddots & \ddots & \vdots \\ 0 & \dots & 0 & -1 & 1 \\ 1 & 0 & \dots & 0 & -1 \end{pmatrix} = \mathrm{C} - \mathrm{I} \tag{14}$$

and in terms of the *z*-transform as $D(z)u(z) \bmod (z^N - 1)$ with $D(z) = z^{-1} - 1$. Then the transposed matrix D^T corresponds to the *z*-transform $D^T(z) = z - 1$ and yields an approximation of the negated first derivative with a

backward difference. Further D^p and $(D^T)^p$serve as approximations of p-th derivatives with an appropriate sign. For time discretisation we use a simple Euler forward scheme. Then the discrete iterative scheme can be written as

$$\begin{aligned} u^0 &= f \\ u^{k+1} &= u^k - \tau (D^T)^p \Phi_{D^p}(u^k) D^p u^k, \; k \in N. \end{aligned} \tag{15}$$

The diagonal matrix $\Phi_{D^p}(u^k) := \operatorname{diag}(|(D^p u^k)_j|)_{j=0,N-1}$ stands for multiplication by the nonlinear diffusivity function. In our computations we use the Perona-Malik function [27] defined as

$$g(s^2) = \left(1 + \frac{s^2}{\lambda^2}\right)^{-1}. \tag{16}$$

See for example [26] for a list of other possible diffusivity functions.

5. DISCRETE WAVELETS AND CONVOLUTION KERNELS

In this section, we formulate the key idea of factorizing discrete wavelets into derivative approximations of smoothing kernels. We make the assumption that the wavelet has p vanishing moments to relate the wavelet transform to an approximation of the p-th derivative. In the discrete setting, this condition reads: A signal $f \in \ell^2(Z)$ is said to have $p \in N$ *vanishing moments* if

$$\begin{aligned} &\sum_{n=-\infty}^{\infty} n^j f_n = 0 \\ &\text{for } \; j \in \{0, p-1\} \\ &\text{and } \; \sum_{n=-\infty}^{\infty} n^p f_n 0. \end{aligned} \tag{17}$$

Let us now factorise the z-transform of a wavelet with p vanishing moments such that we obtain a derivative approximation filter and a convolution or smoothing kernel. Since the number of vanishing moments is directly connected with regularity properties, such factorizations are often used in the design of wavelets (see [7, 31, 21, 17], for example). It should also be noticed that the number of vanishing moments of the filter coefficients is the same as the number of (continuous) vanishing moments of the continuous wavelet function; see [21, Theorem 7.4].

Proposition 5.1 (Wavelet Filter Factorisation)

Let $f \in \ell^2(Z)$ be a filter of finite length and p vanishing moments. Then its z-transform can be decomposed as

$$F(z) = (z-1)^p K(z), \; K(1) = 0, \tag{18}$$

where K^H and K^G are the z-transforms of two smoothing kernels k^H and k^G of the synthesis and analysis wavelet. For orthogonal wavelets, we simply have $K^H(z) = K^G(z)$ and $p = q$. With the two relations (10) and (11) between low- and highpass we see that for the lowpass filters H_0 and G_0, the following relations hold:

Proof: Since f has finite length, the Fourier transform $\hat{f} \in C^\infty$ is infinitely many times differentiable. The j-th derivative of $\hat{f}$ at the point 0 is then

$$\hat{f}^{(j)}(0) = (-i)^j \sum_{n=-\infty}^{\infty} n^j f_n \tag{19}$$

which is the j-th moment of f times the nonzero constant $(-i)^j$. Our assumption about f then reads $\hat{f}^{(j)} = 0$ for $j \in \{0, p-1\}$. This means the Fourier transform of f is a trigonometric polynomial which has a zero of order p in 0. Thus it can be factorised as

$$\hat{f}(\xi) = (\exp(i\xi) - 1)^p K(\exp(i\xi)) \tag{20}$$

with a suitable (Laurent-) polynomial K. Replacing $\exp(i\xi)$ by z directly yields the desired factorisation $F(z) = (z-1)^p K(z)$ of the z-transform.

With the help of this proposition, we can understand the convolution with a wavelet as a derivative approximation of a presmoothed signal. We remember that $z - 1$ is the z-transform of the finite difference matrix D^T approximating the negated first derivative. Thus $(z-1)^p$ can be used as approximation of $(-1)^p$ times the p-th derivative. This reasoning of understanding the wavelet as a derivative of a smoothing kernel is in accordance with the approach in the previous section and the continuous considerations in [9]. For details on such factorizations, see [21, Section 7.2] for orthogonal wavelets and [21, Section 7.4.2] for the biorthogonal case, for example. Let p and q be the number of vanishing moments of our analysis and synthesis highpass filters H_1 and G_1. Then Proposition 5.1 allows us to write the filters as

$$\begin{aligned} H_1(z) &= (z-1)^p K^H(z) \\ \text{and} \quad G_1(z) &= (z-1)^q K^G(z) \end{aligned} \tag{21}$$

where K is the z-transform of the corresponding filter k which will be understood as a smoothing kernel.

Although it is standard in wavelet analysis, we attach a simple proof in order to make the paper more self-contained:

$$H_0(z) = (-1)^q z (z^{-1} + 1)^q K^G(-z^{-1}), \tag{22}$$

$$G_0(z) = (-1)^p z (z^{-1} + 1)^p K^H(-z^{-1}). \tag{23}$$

To make these formulae a bit more intuitive, let us now give some examples of kernels K^H and K^G for commonly used orthogonal wavelets on the finest scale:

Example 5.2 *(Discrete Wavelets and Convolution Kernels)*

(a) Haar Wavelet: For the discrete Haar wavelet, we have $\mathrm{H_1(z)} = \frac{1}{\sqrt{2}}(\mathrm{z}-1)$. The kernel on the finest scale is in this case just a scalar factor $\mathrm{K^H(z)} = \frac{1}{\sqrt{2}}$.

(b) Daubechies Wavelets: The Daubechies wavelet [7] with $p = 2$ is represented by the filter

$$H_1(z) = \frac{1}{4\sqrt{2}}(\sqrt{3} - 1 + (3 - \sqrt{3})z - \\ - (3 + \sqrt{3})z^2 + (1 + \sqrt{3})z^3) \tag{24}$$

which can be factorised as $H_1(z) = (z-1)^2 K^H(z)$ leading to

$$K^H(z) = \frac{1}{4\sqrt{2}}(\sqrt{3} - 1 + (\sqrt{3} + 1)z). \tag{25}$$

Let us briefly say a few words about the differences between our idea and previous approaches to relations between shrinkage on the finest scale and nonlinear diffusion. In contrast to the idea in this paper, Weickert et al. [39] have directly considered the wavelet filter H_1 as stencil for a derivative approximation. With a Taylor expansion, one can directly prove that any filter with p vanishing moments yields an approximation of the p-th derivative up to a constant factor. This works well as long as only the finest scale is considered, but it does not help to explain what happens on coarser scales. Here, we try to model coarser scales by separating the derivative approximation from the smoothing kernel which yields a coarse scale approximation of our signal. In the continuous setting considered in [9], the smoothing kernel is a function for which the scaling operation is invertible without loss of information. In contrast to this, the discrete wavelets on coarser scales treated in this paper can change their appearance due to discretisation effects.

Following [35, Section 3.3], we introduce *wavelets on coarser scales*: starting from the filters G_0 and G_1 on the finest scale, we define the wavelet filters $G_0^{(\sigma)}$ and $G_1^{(\sigma)}$ on coarser scales $\sigma \in \mathbb{N}$ as

$$G_0^{(\sigma)}(z) = \prod_{r=0}^{\sigma-1} G_0(z^{2^r}) \\ \text{and} \quad G_1^{(\sigma)}(z) = G_1(z^{2^{\sigma-1}}) G_0^{(\sigma-1)}(z), \tag{26}$$

and use the same formulae for $H_0^{(\sigma)}$ and $H_1^{(\sigma)}$.

The exponents 2r come from the fact that the algorithme à trous inserts the corresponding number of zeros between two samples of the filter at scale r. In addition, we have to multiply the z-transforms of all filters lying on the path from the input to the middle of the filter bank for H_i in Figure 1, or from the middle to the output for G_i, $i = 0,1$.

Having these formulae at hand we can rewrite the filter bank in Figure 1 with $m + 1$ different paths as shown in Figure 3.

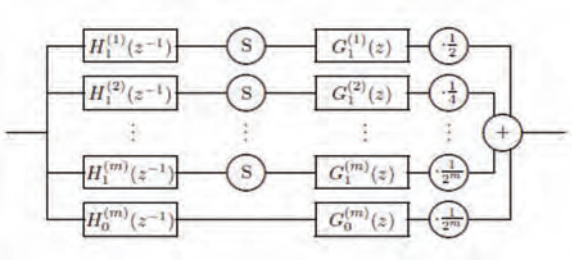

Fig. 3. Filter bank for translation invariant wavelet shrinkage, written with multiple channels.

Now we are interested in the changes of the shape of the convolution kernels corresponding to the wavelets when the scale increases. Our starting point are the relations (26), and we firstly consider the scaling coefficients using the factorisation (23):

$$G_0^{(\sigma)}(z) = \prod_{r=0}^{\sigma-1} G_0(z^{2^r}) \\ = \prod_{r=0}^{\sigma-1} \left((-1)^p z^{2^r} (z^{-2^r} + 1)^p K^H(-z^{-2^r})\right) \\ = (-1)^{\sigma p} z^{2^\sigma - 1} \left(\sum_{r=0}^{2^\sigma - 1} z^{-r}\right)^p \prod_{r=0}^{\sigma-1} K^H(-z^{-2^r}) \tag{27}$$

We see that the scaling filter on larger scales can be decomposed into four parts: The sign given by $(-1)^{\sigma p}$ and the pure shift $z^{(2^\sigma)-1}$ do not change the shape of the convolution kernel. This shape is determined by the rightmost two factors: The second one is a product of the kernels k^H with alternating signs and with inserted zeros. This is actually the wavelet-dependent part. The first factor is independent of the wavelet: It is the p times convolution of a box filter of width 2^σ with itself. This can be understood as a discrete B-spline kernel of order p.

Let us see how this decomposition looks for the wavelet coefficients:

$$G_1^{(\sigma)}(z) = G_1(z^{2^{\sigma-1}}) G_0^{(\sigma-1)}(z) \tag{28}$$

$$= (z^{2^{\sigma-1}} - 1)^q K^G(z^{2^{\sigma-1}}) G_0^{(\sigma-1)}(z) \tag{29}$$

$$= (z-1)^q \left(\sum_{r=0}^{2^{\sigma-1}-1} z^r\right)^q K^G(z^{2^{\sigma-1}}) G_0^{(\sigma-1)}(z) \tag{30}$$

$$= (z-1)^q (-1)^{(\sigma-1)p} \left(z^{-2^{\sigma-1}+1}\right)^{p-1} \left(\sum_{r=0}^{2^{\sigma-1}-1} z^r\right)^{p+q} \cdot \\ \cdot K^G(z^{2^{\sigma-1}}) \prod_{r=0}^{\sigma-2} K^H(-z^{-2^r}). \tag{31}$$

Let us also analyse the ingredients of this product: The first factor $(z - 1)^q$ tells us that the wavelet can be understood as an approximation of the q-th derivative (with sign $(- 1)^q$). It is the z-transform of the finite difference matrix $(D^T)^q$ defined above. Again, the sign and the shift do not change the shape of the convolution kernel. As for the scaling function, we also find a spline kernel of order $p + q$ and a wavelet-dependent part.

Let us now give some examples of commonly used wavelets to see how the related convolution kernels look like:

Example 5.3 *(Haar Wavelet on Coarser Scales)*

We have already seen that for a Haar wavelet we have $p = q = 1$ and the kernels $K^G(z) = K^H(z) = \frac{1}{\sqrt{2}}$ are just constants. Thus the wavelet on scale σ can be seen as

$$G_1^{(\sigma)}(z) = (-1)^{(\sigma-1)}(z-1)\frac{1}{2^{\frac{\sigma}{2}}}\left(\sum_{r=0}^{2^{\sigma-1}-1} z^r\right)^2. \tag{32}$$

This means that in complete analogy to the continuous case, the discrete Haar wavelet is the derivative approximation of a hat function. This hat is created by multiplying a box filter by itself. An example for the scale $\sigma = 8$ is shown in Figure 4.

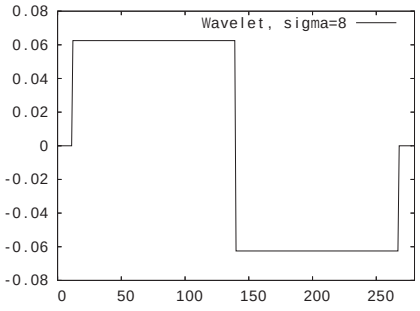

a)

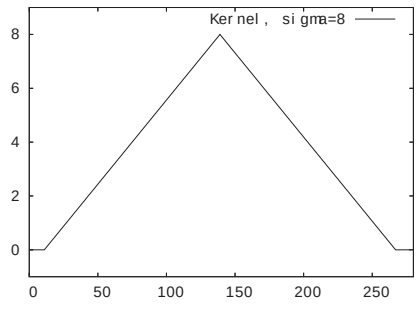

b)

Fig. 4. Convolution kernel corresponding to the Haar wavelet. *a)* Haar wavelet on scale 8. *b)* Corresponding smoothing kernel: a hat function.

Example 5.4 *(Daubechies Wavelets on Coarser Scales)*

For some representatives of the family of Daubechies wavelets [7], we display the corresponding kernels obtained by numerical calculations in Figure 4. One can see that the smoothing kernels have a shape similar to a Gaussian kernel with a perturbation at the right side where they even change the sign. Daubechies has proven that the Haar wavelets are the only symmetric or antisymmetric orthonormal wavelets with compact support [7], and so it is clear that the corresponding kernels of Daubechies wavelets of higher order cannot be symmetric.

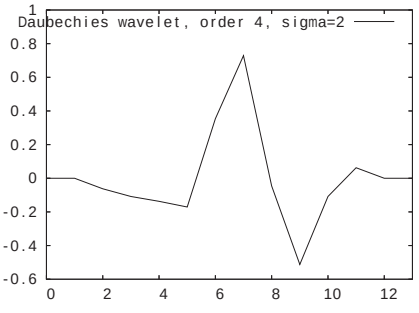

a)

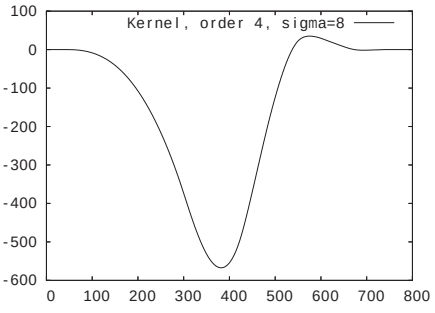

b)

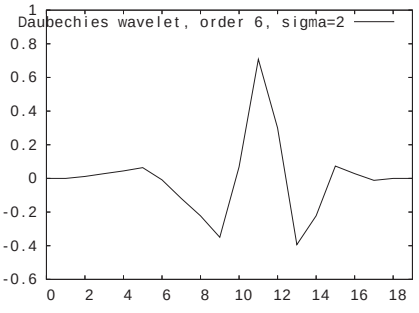

c)

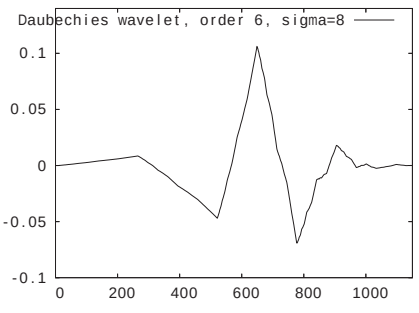

d)

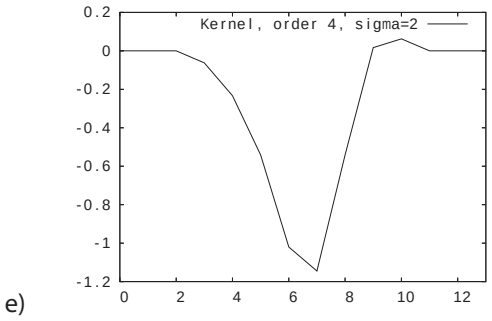

e)

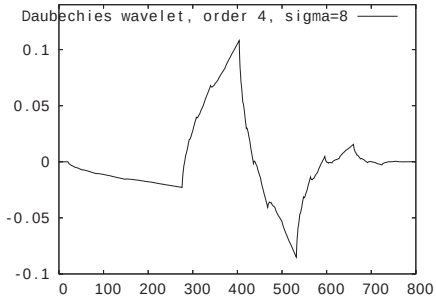

f)

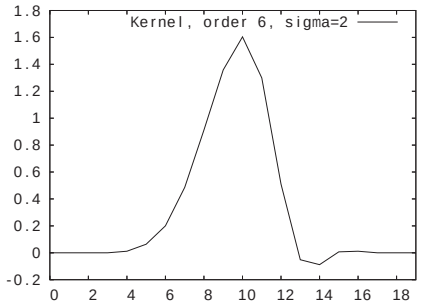

g)

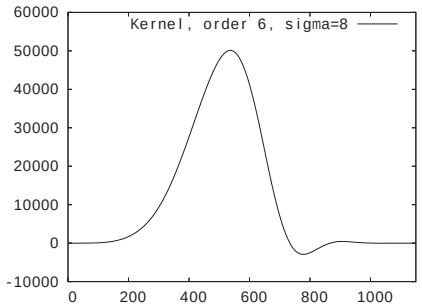

h)

Fig. 5. Convolution kernels corresponding to Daubechies wavelets on larger scales. *a), b), c), d):* Daubechies wavelets of orders 4 and 6 on scales 2 and 8. *e), f), g), h)* Corresponding smoothing kernels. The scaling comes from the fact that wavelets are normalised with respect to the ℓ^2-norm.

The following two examples consider the convolution kernels corresponding to biorthogonal filter pairs. These filters can be symmetric or antisymmetric with compact support. Hence, the convolution kernels can be symmetric.

Example 5.5 *(Compactly Supported Spline Wavelets)*

Figure 5 presents the compactly supported spline wavelet filters h_1 and g_1 with 3 and 7 vanishing moments. Details on these filters can be found in [21, p.~271], for example. We see that the corresponding kernel to h_1 has negative parts while the kernel derived from g_1 is positive and resembles a Gaussian kernel.

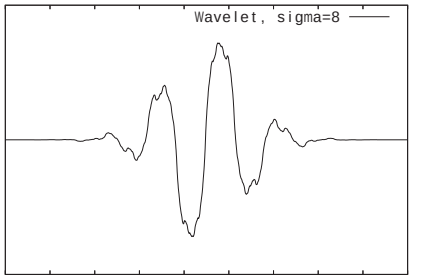

a)

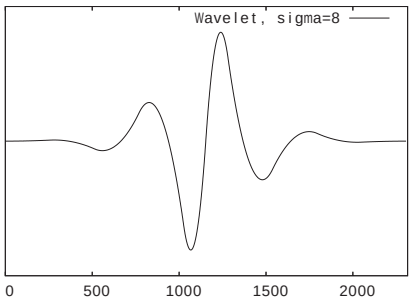

b)

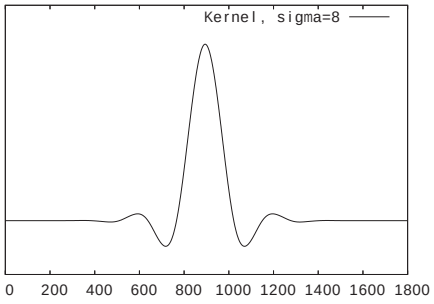

c)

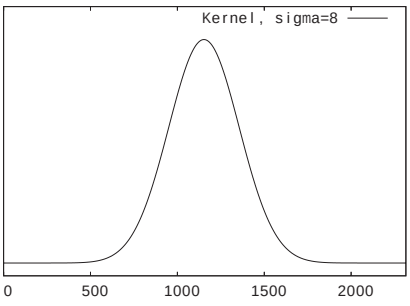

d)

Fig. 6. Convolution kernels corresponding to compactly supported spline wavelets on scale 8. *a)* Filter h_1 with 3 vanishing moments. *b)* Filter g_1 with 7 vanishing moments. *c), d)* Corresponding smoothing kernels.

Example 5.6 *(Perfect Reconstruction Filters of Most Similar Length)*

These biorthogonal filters are displayed in Figure 6 and details can be found in [21, p.~273], for example. The filter corresponding to g_1 has some small negative parts.

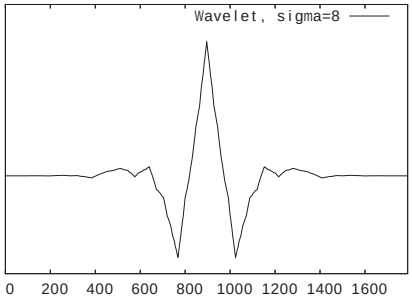

a)

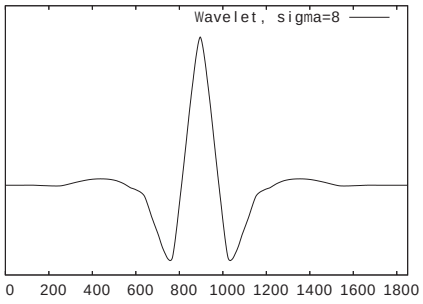

b)

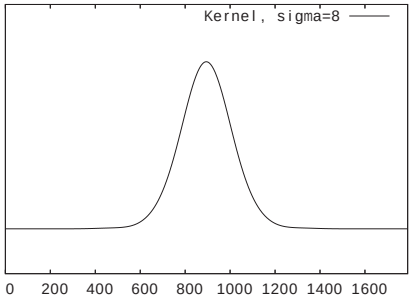

c)

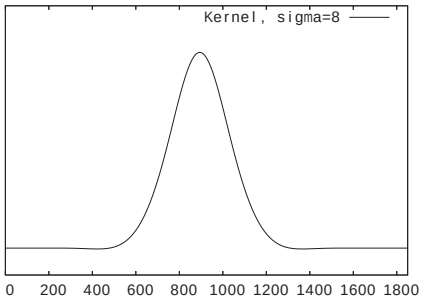

d)

Fig. 7. Convolution kernels corresponding to perfect reconstruction filters of most similar length on scale 8. *a), b)* Analysis and synthesis filter. *c), d)* Corresponding smoothing kernels.

Regardless of the shape of convolution kernels, it will be important for our considerations in the next section that we can write the analysis and the synthesis wavelet as

$$G_1^{(\sigma)}(z) = (1-z)^q K^{G,(\sigma)}(z)$$
$$\text{and} \quad H_1^{(\sigma)}(z) = (1-z)^p K^{H,(\sigma)}(z). \tag{33}$$

We use notions $K^{G,(\sigma)}$ and $K^{H,(\sigma)}$ to denote the corresponding convolution kernels on scale σ. With the finite difference matrices introduced in (14), we can rewrite (33) in matrix notation as

$$G_1^{(\sigma)} = (D^q)^T K^{G,(\sigma)}$$
$$\text{and} \quad H_1^{(\sigma)} = (D^p)^T K^{H,(\sigma)}. \tag{34}$$

We will use these equations in the next section to rewrite iterated wavelet shrinkage as discretisation of an integrodifferential equation.

6. RELATIONS BETWEEN BOTH METHODS

In this section, let $f, u \in \mathbb{R}^N$ be vectors and $H_i^{(\sigma)}, G_i^{(\sigma)}, i = 0,1$ denote the N x N circulant matrices corresponding to the filters $H_i^{(\sigma)}(z), G_i^{(\sigma)}(z)$ modulo z^N - 1. Then we can rewrite wavelet shrinkage according to Figure 3 as

$$u = \sum_{\sigma=1}^{m} \frac{1}{2^\sigma} G_1^{(\sigma)} S\big((H_1^{(\sigma)})^T f\big) + \quad G$$
$$+ \frac{1}{2^m} G_0^{(m)} (H_0^{(m)})^T f. \tag{35}$$

Analysis matrices are transposed to reflect the fact that we have used $H_i(z^{-1})$ for $i = 0,1$ for the analysis part of our filter banks in Figures 1, 2, and 3. The function S is meant to act componentwise on the vector entries.

Without shrinking the coefficients, the filter bank will allow for a perfect reconstruction, which means that

$$u = \sum_{\sigma=1}^{m} \frac{1}{2^\sigma} G_1^{(\sigma)} S\big((H_1^{(\sigma)})^T f\big) + \quad G$$
$$+ \frac{1}{2^m} G_0^{(m)} (H_0^{(m)})^T f. \tag{36}$$

for all $f \in \mathbb{R}^N$. Similarly to [26, 9], we use

$$S(x) = (1 - \tau g(|x|))x \tag{37}$$

to rewrite our shrinkage function with the help of a function g which will play the role of diffusivity later on. This leads to pairs of shrinkage functions and diffusivities which are studied in detail in [26]. Inserting (37) into (35) we obtain

$$u = \sum_{\sigma=1}^{m} \frac{1}{2^\sigma} G_1^{(\sigma)} (H_1^{(\sigma)})^T f + \frac{1}{2^m} G_0^{(m)} (H_0^{(m)})^T f$$
$$-\tau \sum_{\sigma=1}^{m} \frac{1}{2^\sigma} G_1^{(\sigma)} \Phi((H_1^{(\sigma)})^T f)(H_1^{(\sigma)})^T f \tag{38}$$

where Φ is a diagonal matrix such that $\Phi(v) := diag(|v_j|^2)_{j\in J}$. By property (36) the first part is just a reconstruction of the initial signal *f*, and we obtain

$$\Phi(v) := diag(|v_j|^2)_{j\in J} \tag{39}$$

for one multilevel shrinkage step. Iterating these multilevel shrinkage steps leads to the scheme

$$u^0 = f$$
$$u^{k+1} = u^k - \tau \sum_{\sigma=1}^{m} \frac{1}{2^\sigma} G_1^{(\sigma)} \Phi((H_1^{(\sigma)})^T u^k)(H_1^{(\sigma)})^T u^k,$$
$$k \in \mathbb{N} \tag{40}$$

which has a similar structure as the discretisation of the nonlinear diffusion equation (15). Using (34), the iteration rule can be written as

$$u^{k+1} = u^k - \tau \sum_{\sigma=1}^{m} \frac{1}{2^\sigma} (D^q)^T K^{G,(\sigma)} \Phi(D^p (K^{H,(\sigma)})^T u^k) \cdot \cdot D^p (K^{H,(\sigma)})^T u^k. \tag{41}$$

A continuous equivalent, the integrodifferential equation

$$u^{k+1} = u^k - \tau(-1)^{p+1} \int_0^\infty \sigma^{2p} \partial_x^p \theta_\sigma * \left(g\left(\sigma^p \partial_x^p \tilde{\theta}_\sigma\right)(\partial_x^p \tilde{\theta}_\sigma * u)\right) \frac{d\sigma}{\sigma^2} \tag{42}$$

with a smoothing kernel θ_σ and its mirrored version $\tilde{\theta}_\sigma$ has been derived in [9]. It becomes evident that (41) can be considered as a discrete version of this integrodifferential equation. As in the continuous case, in our discrete setting we also see two differences between discrete wavelet shrinkage (41) and nonlinear diffusion filtering (15); namely, all derivatives are presmoothed and we sum over all scales σ. In contrast to continuous considerations, we have worked with two different kernels to allow for biorthogonal wavelets. This can lead to partial differential equations with different orders of the inner and the outer derivative.

In the PDE-based image processing context, similar ideas, but without presmoothing, have been used in the filters of Tumblin and Turk [32] and Wei [37]. They proposed to use evolution equations of the form

$$u_t = -div(g(m)\nabla\Delta u) \tag{43}$$

where *m* is the squared gradient norm or the squared Frobenius norm of the Hessian matrix of *u*. In this respect these approaches even go one step further: They do not only allow the derivative orders in front of the nonlinear function and behind to be different, but the argument can also be a third order one, while *m* depends on first or second order derivatives. By the construction (41) this is not included in our framework since the argument of diffusivity is always the same as its multiplier.

Remark 6.1 *(Orthogonal Wavelets)*

In the case of orthogonal wavelets, (41) simplifies to

$$u^{k+1} = u^k - \tau \sum_{\sigma=1}^{m} \frac{1}{2^\sigma} (D^p)^T K^{H,(\sigma)} \Phi(D^p (K^{H,(\sigma)})^T u^k) * * D^p (K^{H,(\sigma)})^T u^k. \tag{44}$$

Besides smoothing kernels and the sum over all scales, this is identical to an explicit discretisation of a higher order nonlinear diffusion equation. Since the outer matrices are the adjoints of the inner ones, this approach can be understood as arising from an energy function of the form

$$E(u) = \sum_{i\in J} (u_i - f_i)^2 + \alpha \sum_{\sigma=1}^{m} \frac{1}{2^\sigma} \sum_{i\in J} \Psi(D^p K^{H,(\sigma)} u)_i^2 \tag{45}$$

with $\Psi'(s^2) = g(s^2)$. Continuous analoga to this equation can be found in [9, 4], for example. For biorthogonal wavelets such a formulation does not exist.

7. GENERALISATION TO HIGHER DIMENSIONS

So far, the ideas in this paper have been considered in one spatial dimension only. Let us turn to the two-dimensional case. For one single scale of Haar wavelet shrinkage, relations to nonlinear diffusion equations have been discussed by Mrázek and Weickert [25]. Here we follow the strategy sketched in [25], but apply it not only to one scale of Haar wavelet shrinkage, but to multiple ones with general biorthogonal filters.

It is common to use tensor product wavelets for processing of two-dimensional images; see [21, Subsections 7.7.2 and 7.7.3] or [13, Section 7.5], for example. With the one-dimensional analysis scaling coefficients h_0 and wavelet coefficients h_1, the tensor product analysis filters h_s, h_h, h_v, and h_d in 2-D read

$$
\begin{aligned}
h_s(i,j) &:= h_0(i)h_0(j),\\
h_h(i,j) &:= h_1(i)h_0(j),\\
h_v(i,j) &:= h_0(i)h_1(j),\\
h_d(i,j) &:= h_1(i)h_1(j).
\end{aligned}
\tag{46}
$$

Here, the subscript *s* stands for a scaling function, *h* for the horizontal, *v* for the vertical, and *d* for the diagonal wavelet. The same definition applies for the synthesis coefficients with *g* instead of *h*. It is a classical result that these filters on multiple scales yield a biorthogonal family in 2-D. In analogy to (36), the perfect reconstruction property for *m* scales in 2-D can be formulated as

$$
\begin{aligned}
f = \sum_{\sigma=1}^{m} \frac{1}{4^{\sigma}} \sum_{\delta \in \{h,v,d\}} G_{\delta}^{(\sigma)} (H_{\delta}^{(\sigma)})^T f \; + \\
+ \frac{1}{4^{m}} G_s^{(m)} (H_s^{(m)})^T f.
\end{aligned}
\tag{47}
$$

Then one step of shrinkage reads

$$
\begin{aligned}
u = \sum_{\sigma=1}^{m} \frac{1}{4^{\sigma}} \sum_{\delta \in \{h,v,d\}} G_{\delta}^{(\sigma)} S^{\delta} H_{\delta}^{(\sigma)T} f \; + \\
+ \frac{1}{4^{m}} G_s^{(m)} (H_s^{(m)})^T f
\end{aligned}
\tag{48}
$$

with shrinkage functions S^h, S^v, and S^d applied to the corresponding wavelet coefficients.

To give a motivation for using different shrinkage functions S^{δ} in the three directions, we have a look at the approximation properties of the wavelet coefficients in 2-D. Convolution of an image with the filters given above can also be understood as a derivative approximation with presmoothing where the derivative order and the smoothing kernel depend on h_1 and h_0. For example, let *p* be the number of vanishing moments of h_1. Convolution of a discrete image *u* with h_h and h_v approximates presmoothed *p*-th derivatives of *u* with shrinkage functions S^h, S^v, and S^d applied to the corresponding wavelet coefficients.

To give a motivation for using different shrinkage functions S^{δ} in the three directions, we have a look at the approximation properties of the wavelet coefficients in 2-D. Convolution of an image with the filters given above can also be understood as a derivative approximation with presmoothing where the derivative order and the smoothing kernel depend on h_1 and h_0. For example, let *p* be the number of vanishing moments of h_1. Convolution of a discrete image *u* with h_h and h_v approximates presmoothed *p*-th derivatives of *u* in *x*- and *y*-direction. The filter h_d yields the approximation of the derivative $\partial_x^p \partial_y^p u$ with additional smoothing. That means this derivative in diagonal direction has twice the order than the other ones. This fact suggests to follow the shrinkage rule described in [24] to improve rotational invariance. Inspired by nonlinear diffusion filtering, it is suggested in [24] to couple the horizontal and vertical coefficients in the argument of the shrinkage function and not to shrink the diagonal ones at all. Let w_h, w_v, and w_d stand for wavelet coefficients in horizontal, vertical and diagonal direction at a given scale and position. The corresponding shrinkage functions applied to the horizontal, vertical and diagonal coefficients can be written as:

$$
\begin{aligned}
S^h(w_h, w_v) &:= w_h(1 - \tau g(w_h^2 + w_v^2)),\\
S^v(w_h, w_v) &:= w_d(1 - \tau g(w_h^2 + w_v^2))
\end{aligned}
\tag{49}
$$

$$
S^d(w_d) := w_d \tag{50}
$$

In contrast to [24], we avoid the additional factor 4 in front of the function *g* here. This factor can be explained as a compensation of the factor 1/4 appearing in (47) and (48) together with the fact that only the finest scale is considered in [24]. We avoid the factor here since we work on multiple scales and prefer to use the same shrinkage function on all scales.

With these shrinkage functions and the perfect reconstruction property (47), wavelet shrinkage (48) can be transformed into

$$
\begin{aligned}
u = f - \tau \sum_{\sigma=1}^{m} \frac{1}{4^{\sigma}} (G_h^{(\sigma)} \Phi_h^{(\sigma)} (H_h^{(\sigma)})^T f + G^{\sigma} \Phi \\
+ G_v^{(\sigma)} \Phi_v^{(\sigma)} (H_v^{(\sigma)})^T f)
\end{aligned}
\tag{51}
$$

Here, $\Phi_h^{(\sigma)}$ and $\Phi_v^{(\sigma)}$ represent a pointwise multiplication of the wavelet coefficients in horizontal and vertical direction on scale σ with diffusivity *g* in (49) and (50). Note that this diffusivity depends on the sum of the squared horizontal and vertical wavelet coefficients at the corresponding position and scale. Understood as discretisation of an integrodifferential equation, one would use it iteratively yielding

$$
\begin{aligned}
u^{k+1} = u^k - \tau \sum_{\sigma=1}^{m} \frac{1}{4^{\sigma}} (G_h^{(\sigma)} \Phi_h^{(\sigma)} (H_h^{(\sigma)})^T u^k + G^{\sigma} \Phi \\
+ G_v^{(\sigma)} \Phi_v^{(\sigma)} (H_v^{(\sigma)})^T u^k)
\end{aligned}
\tag{52}
$$

This is a 2-D analogue of (41).

Example 7.1 *(Orthogonal Wavelets in 2-D)*

Let us consider the case of orthogonal wavelets, i. e., $G_h = H_h$ and $G_v = H_v$, with *p* vanishing moments. If we neglect presmoothing introduced by the wavelets, the shrinkage process is obviously connected to a continuous equation of the form

$$
\begin{aligned}
\partial_t u = (-1)^{p+1} (\partial_x^p g(|\partial_x^p u|^2 + |\partial_y^p u|^2) \partial_x^p u + \partial \; g \\
+ \partial_y^p g(|\partial_x^p u|^2 + |\partial_y^p u|^2) \partial_y^p u)
\end{aligned}
\tag{53}
$$

which only considers the derivatives with respect to the coordinate axes. For $p = 1$, this is the classical Perona-Malik equation. For higher derivative orders $p > 1$, it only involves the derivatives of order p in coordinate directions and no mixed derivatives.

8. NUMERICAL EXPERIMENTS

In this section we want to investigate experimentally the differences between nonlinear diffusion filtering and our discrete version of the integrodifferential equations related to wavelet shrinkage described in this paper. These experiments should help to understand the meaning of larger scales for the iterative denoising process. As a reference we use nonlinear diffusion filtering since it is equivalent to the integrodifferential equation on the finest scale only, and successively add larger scales. In 1-D, we perform detailed qualitative comparisons for denoising of a signal with additive Gaussian noise. Experiments for image simplification in 2-D show that the same effects appear for higher spatial dimensions. All implementations have been written in C.

Let us first describe our experiments in 1-D: Figure 7 shows our test signal piecepoly taken from the Wavelab library[1] and its noisy version with additive Gaussian noise of standard deviation 20.

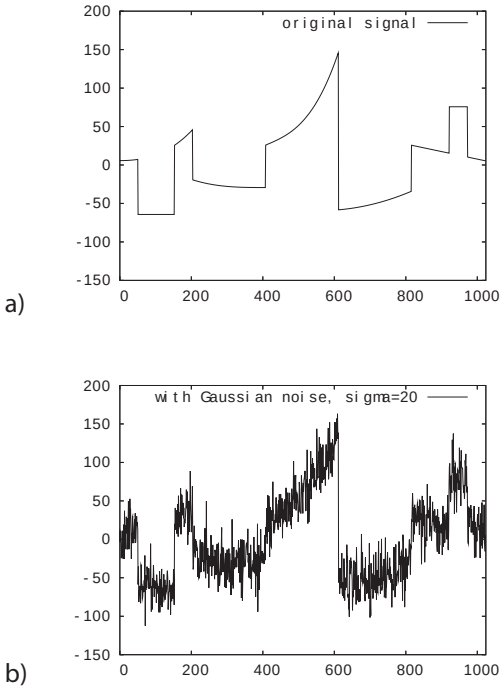

Fig. 8. Test signals. *a)* Piecewise polynomials signal with 1024 pixels. *b)* With additive Gaussian noise, standard deviation 20. .

1 Wavelab is available at http://www-stat.stanford.edu/wavelab/.

In our first experiment, we compare the quality of presmoothed iterative denoising methods on a single scale σ given by the equation

$$u^{k+1} = u^k - \tau (D^p)^T K^{H,(\sigma)} \Phi^\sigma * \\ * (D^p (K^{H,(\sigma)})^T u^k) D^p (K^{H,(\sigma)})^T u^k. \quad (54)$$

In our experiments, we have used the order $p = 1$ and the hat function as kernel in the matrices K^H. As we have seen in Section 5, this corresponds to Haar wavelets. The kernel length is $l = 2\sigma$. Moreover, we have applied the Perona-Malik diffusivity in the diagonal matrix Φ. Notice that $\sigma = 1$ corresponds to classical diffusion filtering. We have used one single scale for presmoothing, and thus in contrast to (41), there is no sum and no weight factor on the right-hand side. The parameters have been optimised in order to obtain minimal errors in both the ℓ^1- and ℓ^2-norms. The optimal parameters and the corresponding mimimal error measures can be found in Table 0. We see that the minimal errors are obtained for classical nonlinear diffusion filters without presmoothing.

Table 1: Error norms for denoising results with presmoothed diffusion and one single scale.

Scale σ	l^1-error per pixel		
	error	λ	iterations
1	2.740	1.02	4593
2	5.087	0.10	247000
3	6.515	0.10	351000

Scale σ	l^2-error per pixel		
	error	λ	iterations
1	0.141	1.67	1265
2	0.227	0.10	233000
3	0.285	0.10	263000

To visualise the differences some of the corresponding signals are displayed in Figure 8. It is clearly visible that using single-scale presmoothing kernels for all derivatives leads to artefacts. The process is not able to remove the noise on the small scales which leads to oscillations. Only the general shape of the signal is restored for larger scales. This is in accordance with the results reported by Scherzer and Weickert [28].

a)

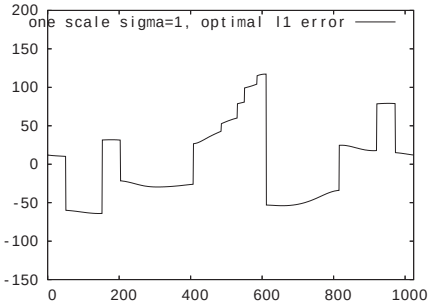

b)

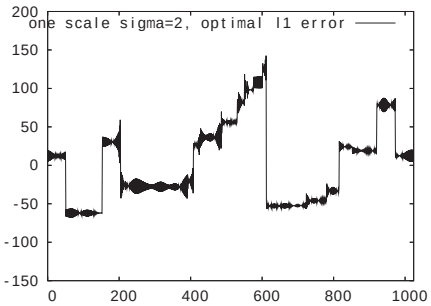

c)

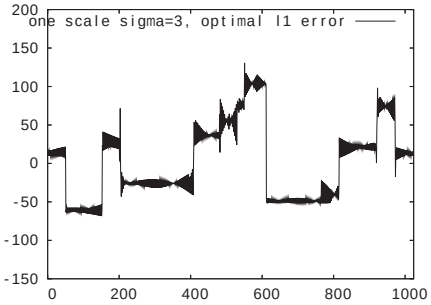

Fig. 9.a Denoising results with presmoothed diffusion and one single scale σ. Results with optimal ℓ^1-error. *a)* σ = 1. *b)* σ = 2. *c)* σ = 3.

a)

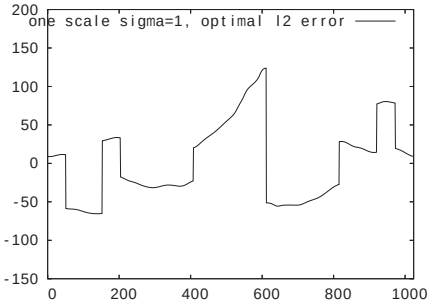

b)

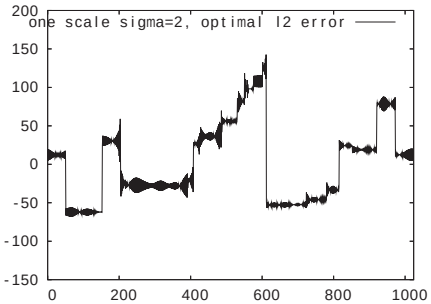

c)

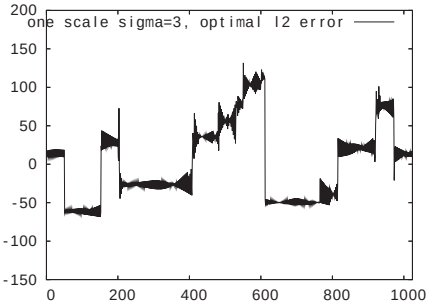

Fig. 9.b Denoising results with presmoothed diffusion and one single scale σ. Results with optimal ℓ^2-error. *a)* σ = 1. *b)* σ = 2. *c)* σ = 3.

In our second experiment, we do not only filter with one larger scale, but involve all dyadic scales $\sigma = 2^l$ for $l = 0, \ldots, k$ and use (44) for filtering. The corresponding optimal error measures are shown in Table 1. We have used a time step size $\tau = 1/2$. We see that involving larger scales does not influence the minimal error as severly as in the first experiment. For the ℓ^1-error, it is even possible to obtain better values by using $k = 2$. We notice that using only the finest scale requires half the number of iterations than in the first experiment: This is caused by the additional factor 1/2 in (44) on the finest scale which was not present in the last experiment. The necessary number of iterations reduces by two orders of magnitude by involving larger scales. This can be understood as an approximative numerical method for speeding up the process.

Table 2: Error norms for denoising results using presmoothed diffusion on dyadic scales.

Largest scale	l^1-error per pixel		
$\sigma = 2^k$	**error**	**λ**	**iterations**
$k = 0$	2.740	1.02	9197
$k = 1$	2.824	1.47	1904
$k = 2$	**2.717**	**2.39**	**495**
$k = 3$	2.791	4.02	153
$k = 4$	3.000	6.36	53
$k = 5$	3.184	8.95	27

Largest scale	l^2-error per pixel		
$\sigma = 2^k$	**error**	**λ**	**iterations**
$k = 0$	**0.140**	**1.67**	**2604**
$k = 1$	0.142	2.11	677
$k = 2$	145.03	3.57	200
$k = 3$	0.143	4.95	95
$k = 4$	0.146	5.84	61
$k = 5$	0.150	6.47	48

The corresponding signals are shown in Figure 10. We see that for larger scales, some smaller artefacts appear. Nevertheless, it seems that the presence of smaller scales on the right-hand side can help to suppress most of them.

a)

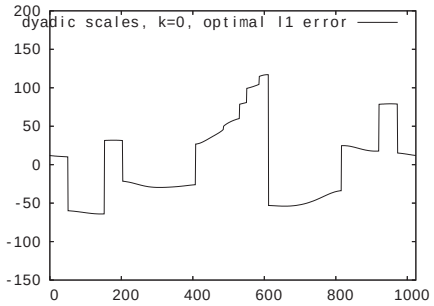

b)

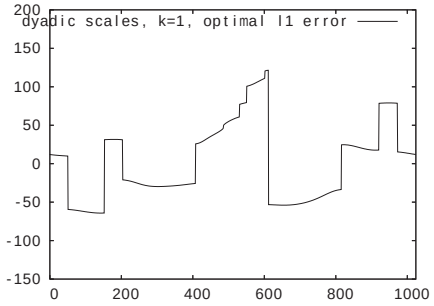

c)

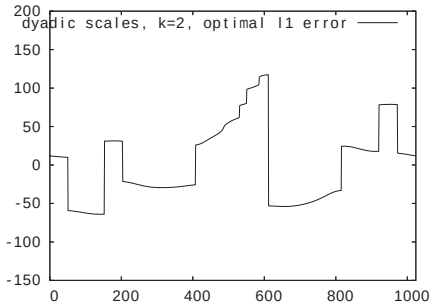

d)

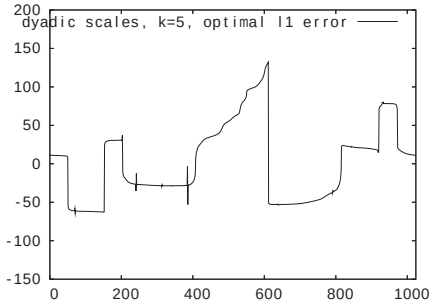

Fig. 10.a Denoising results with presmoothed diffusion and dyadic scale up to $\sigma = 2^k$. Results with optimal ℓ^1-error. *a)* $k = 0$. *b)* $k = 1$. *c)* $k = 2$. *d)* $k = 5$.

a)

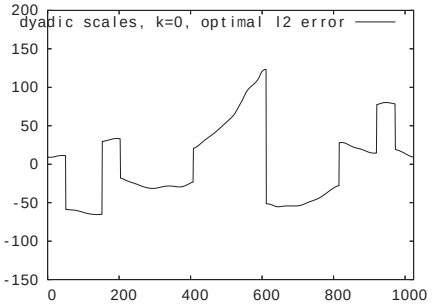

b)

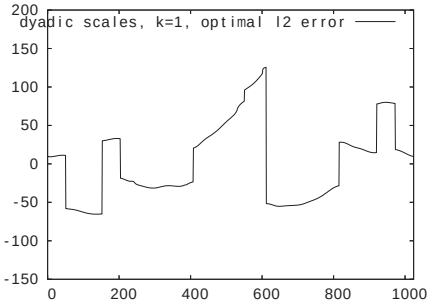

c)

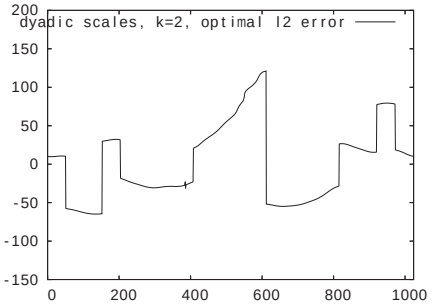

d)

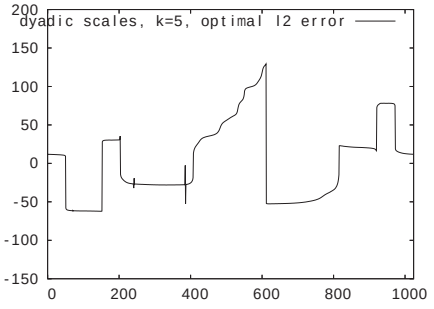

Fig. 10.b Denoising results with presmoothed diffusion and dyadic scale up to $\sigma = 2^k$. Results with optimal ℓ^2-error. *a)* $k = 0$. *b)* $k = 1$. *c)* $k = 2$. *d)* $k = 5$.

In our 2-D experiment, we also display results for smoothing on one larger scale and on all dyadic scales. For one larger scale, we use the filter

$$u^{k+1} = u^k - \tau\big(K_h^{(\sigma)}\Phi_h^{(\sigma)}(K_h^{(\sigma)})^T u^k + K^{\sigma}\Phi + K_v^{(\sigma)}\Phi_v^{(\sigma)}(K_v^{(\sigma)})^T u^k\big) \quad (55)$$

This corresponds to (52) where the factor and the sum on the right-hand side are left out. We use $p = 1$ and hat functions in the directions of the derivative and box filters in the other direction which implements tensor product Haar wavelets. Figure 11 shows the resulting images if we fix all parameters and only vary the scale. We see that using larger scales only introduces artefacts in the image which can be compared to those appearing also in a 1-D case.

For involving all scales we directly use (52). Some results for involving all dyadic scales up to a certain order are displayed in Figure 12. Here we see that more and more small details are removed by using larger scales while the artefacts are suppressed.

Fig. 11. Image simplification results with presmoothed diffusion and one single scale σ, Perona-Malik diffusivity $g(s^2) = 1/(1 + s^2/\lambda^2)$ with $\lambda = 10$, and stopping time $t = 5$. a) Original image, 512 x 512 pixels. b) $\sigma = 1$, c) $\sigma = 2$, d) $\sigma = 3$.

For involving all scales we directly use (52). Some results for involving all dyadic scales up to a certain order are displayed in Figure 12. Here we see that more and more small details are removed by using larger scales while the artefacts are suppressed.

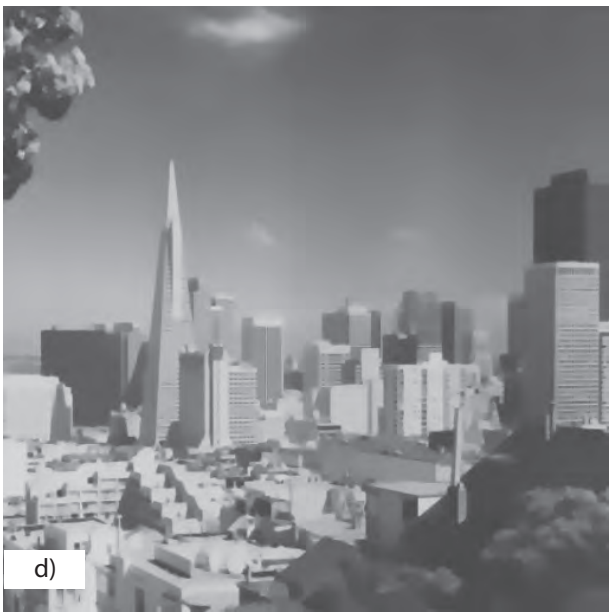

Fig. 12. Image simplification results with presmoothed diffusion, $g(s^2) = (1 + s^2/\lambda^2)^{-1}$ for $\lambda = 10$, stopping time $t = 20$, and dyadic scales up to $\sigma = 2^k$. *a)* Original image, 512 x 512 pixels, *b)* $k = 0$, *c)* $k = 1$, *d)* $k = 5$.

9. CONCLUSION

In this paper, we have investigated the relation between discrete multiscale wavelet shrinkage on the one hand and discretised nonlinear diffusion filters of arbitrary order and their variational counterparts on the other. To this end, we exploited the fact that the wavelet transform using wavelets with a finite number of vanishing moments represents smoothed derivative operators. The resulting discrete integrodifferential equations differ from their nonlinear diffusion counterparts by additional presmoothing of derivatives and integration over a larger number of scales. The shape of the corresponding convolution kernels changes for coarser scales in the discrete setting due to sampling. We have extended considerations from orthogonal to biorthogonal wavelets: Here, the corresponding discrete versions of integrodifferential equations are no longer related to diffusion equations, but to more general PDE models like the methods by Tumblin and Turk [32] or Wei [37]. Using tensor product wavelets and special shrinkage rules to improve the rotation invariance, the relations have been carried over to the 2-D setting. Numerical experiments have shown that presmoothed nonlinear diffusion on one single larger scale gives worse results than classical nonlinear diffusion. However, involving all dyadic scales up to a certain order, as done in wavelet shrinkage, almost keeps the good quality and significantly reduces the number of required iterations. In this sense, discrete multiscale wavelet shrinkage can be understood as a numerical method for discrete integrodifferential equations.

ACKNOWLEDGEMENTS

We gratefully acknowledge partly funding by the Deutsche Forschungsgemeinschaft (DFG), project WE 2602/2-3.

REFERENCES

[1] Y. Bao and H. Krim, *Towards bridging scale-space and multiscale frame analyses,* in Wavelets in Signal and Image Analysis, A. A. Petrosian and F. G. Meyer, eds., vol. 19 of Computational Imaging and Vision, Kluwer, Dordrecht, 2001, ch. 6, pp. 169-192.

[2] K. Bredies, D. A. Lorenz and P. Maass, *Mathematical concepts of multiscale smoothing*, Applied and Computational Harmonic Analysis, 19 (2005), pp. 141-161.

[3] A. Chambolle, R. DeVore, N.-Y. Lee and B. J. Lucier, *Nonlinear wavelet image processing: Variational problems, compression, and noise removal through wavelet shrinkage*, IEEE Transactions on Image Processing, 7 (1998), pp. 319-335.

[4] A. Chambolle and B. L. Lucier, *Interpreting translation-invariant wavelet shrinkage as a new image smoothing scale space*, IEEE Transactions on Image Processing, 10 (2001), pp. 993-1000.

[5] R. E. Crochiere and L. R. Rabiner, *Digital coding of speech in sub-bands*, Bell Systems Technical Journal, 55 (1976), pp. 1069-1085.

[6] A. Croisier, D. Esteban and C. Galand, *Perfect channel splitting by use of interpolation / decimation / tree decomposition techniques,* in International Conference on Information Sciences and Systems, Patras, Greece, Aug. 1976, pp. 443-446.

[7] I. Daubechies, Ten Lectures on Wavelets, SIAM, Philadelphia, 1992.

[8] S. Didas, G. Steidl, and J. Weickert, *Discrete multiscale wavelet shrinkage and integrodifferential equations,* in Optical and Digital Image Processing - Photonics Europe, P. Schelkens, T. Ebrahimi, G. Cristobal, and F. Truchetet, eds., vol. 7000 of Proceedings of SPIE, 2008, pp. 70000S-1 { 70000S-12.

[9] S. Didas and J. Weickert, *Integrodifferential equations for continuous multiscale wavelet shrinkage,* Inverse Problems and Imaging, 1 (2007), pp. 47-62.

[10] S. Didas, J. Weickert and B. Burgeth, *Stability and local feature enhancement of higher order nonlinear diffusion filtering*, in Pattern Recognition, W. Kropatsch, R. Sablatnig, and A. Hanbury, eds., vol. 3663 of Lecture Notes in Computer Science, Springer, 2005, pp. 451-458.

[11] S. Didas, J. Weickert and B. Burgeth, *Properties of higher order nonlinear diffusion filtering*, Journal of Mathematical Imaging and Vision, 35 (2009), pp. 208-226.

[12] D. L. Donoho and I. M. Johnstone, *Ideal spatial adaption by wavelet shrinkage*, Biometrica, 81 (1994), pp. 425-455.

[13] R. C. Gonzalez and R. E. Woods, *Digital Image Processing*, Prentice Hall, second ed., 2002.

[14] M. Holschneider, R. Kronland-Martinet, J. Morlet and P. Tchamitchian, *A real-time algorithm for signal analysis with the help of the wavelet transform*, in Wavelets, Time-Frequency Methods and Phase Space, J. M. Combes, A. Grossmann, and P. Tchamitchian, eds., Springer, Berlin, 1989, pp. 286-297.

[15] R. A. Horn and C. R. Johnson, *Matrix Analysis*, Cambridge University Press, 1985.

[16] T. Iijima, *Basic theory on normalization of pattern (in case of typical one-dimensional pattern),* Bulletin of the Electrotechnical Laboratory, 26 (1962), pp. 368-388. (In Japanese).

[17] A. K. Louis, P. Maa , and A. Rieder, *Wavelets*, B. G. Teubner Stuttgart, second ed., 1998.

[18] M. Lysaker, A. Lundervold and X.-C. Tai, *Noise removal using fourth-order partial differential equation with applications to medical magnetic resonance images in space and time*, IEEE Transactions on Image Processing, 12 (2003), pp. 1579-1590.

[19] S. Mallat, *Multiresolution approximations and wavelet orthonormal bases of L2(R),* Transactions of the Americal Mathematical Society, 315 (1989), pp. 69-87.

[20] S. Mallat, *A theory for multiresolution signal decomposition: the wavelet representation*, IEEE Transactions on Pattern Analysis and Machine Intelligence, 11 (1989), pp. 674-693.

[21] S. Mallat, *A Wavelet Tour of Signal Processing*, Academic Press, San Diego, second ed., 1999.

[22] Y. Meyer, *Wavelets and Operators*, vol. 37 of Cambridge Studies in Advanced Mathematics, Cambridge University Press, 1992.

[23] F. Mintzer, *Filters for distortion-free two-band multirate filter banks*, IEEE Transactions on Acoustics, Speech, and Signal Processing, 33 (1985), pp. 626-630.

[24] P. Mrazek and J. Weickert, *Rotationally invariant wavelet shrinkage*, in Pattern Recognition, B. Michaelis and G. Krell, eds., vol. 2781 of Lecture

Notes in Computer Science, Springer, Berlin, 2003, pp. 156-163.

[25] P. Mrazek and J. Weickert, *From two-dimensional nonlinear diffusion to coupled Haar wavelet shrinkage*, Journal of Visual Communication and Image Representation, 18 (2007), pp. 162-175.

[26] P. Mrazek, J. Weickert and G. Steidl, *Diffusion-inspired shrinkage functions and stability results for wavelet denoising*, International Journal of Computer Vision, 64 (2005), pp. 171-186.

[27] P. Perona and J. Malik, *Scale space and edge detection using anisotropic diffusion*, IEEE Transactions on Pattern Analysis and Machine Intelligence, 12 (1990), pp. 629-639.

[28] O. Scherzer and J. Weickert, *Relations between regularization and diffusion filtering*, Journal of Mathematical Imaging and Vision, 12 (2000), pp. 43.-63.

[29] M. Smith and T. Barnwell III, *Exact reconstruction techniques for tree structures subband coders*, IEEE Transactions on Acoustics, Speech, and Signal Processing, 34 (1986), pp. 434-441.

[30] G. Steidl, J. Weickert, T. Brox, P. Mrazek and M. Welk, *On the equivalence of soft wavelet shrinkage, total variation diffusion, total variation regularization, and SIDEs*, SIAM Journal on Numerical Analysis, 42 (2004), pp. 686-713.

[31] G. Strang and T. Nguyen, *Wavelets and Filter Banks*, Wellesley-Cambridge Press, 1997.

[32] J. Tumblin and G. Turk, LCIS: *A boundary hierarchy for detail-preserving contrast reduction*, in SIGGRAPH '99: Proceedings of the 26th Annual Conference on Computer Graphics and Interactive Techniques, ACM Press/Addison-Wesley Publishing Co., 1999, pp. 83-90.

[33] M. Vetterli, *Multidimensional subband coding: some theory and algorithms*, Signal Processing, 6 (1984), pp. 97-112.

[34] M. Vetterli, *Filter banks allowing perfect reconstruction*, Signal Processing, 10 (1986), pp. 219-244.

[35] M. Vetterli and J. Kovačević, *Wavelets and Subband Coding*, Prentice-Hall, Upper Saddle River, 1995.

[36] J. B. Weaver, Y. Xu, D. M. Healy and L. D. Cromwell, *Filtering noise from images with wavelet transforms*, Magnetic Resonance in Medicine, 21 (1991), pp. 288-295.

[37] G. W. Wei, *Generalized Perona-Malik equation for image restoration*, IEEE Signal Processing Letters, 6 (1999), pp. 165-167.

[38] J. Weickert, *Anisotropic Diffusion in Image Processing*, B. G. Teubner, Stuttgart, 1998.

[39] J. Weickert, G. Steidl, P. Mrazek, M. Welk and T. Brox, *Diffusion filters and wavelets: What can they learn from each other?*, in Handbook of Mathematical Models in Computer Vision, N. Paragios, Y. Chen, and O. Faugeras, eds., Springer, New York, 2006, pp. 3-16.

[40] A. P. Witkin, *Scale-space Filtering*, in Proc. Eighth International Joint Conference on Artificial Intelligence, vol. 2, Karlsruhe, Germany, August 1983, pp. 945-951.

Advanced Scientific Visualization, a Multidisciplinary Technology Based on Engineering and Computer Science

Dean Vucinic
Department of Mechanical Engineering, Vrije Universiteit Brussel
Pleinlaan 2, B- 1050 Brussels, Belgium
dean.vucinic@vub.ac.be

Abstract *– Today's visualization tools are equipped with highly interactive visual aids, which allow analysis and inspection of complex numerical data generated from high-bandwidth data sources such as simulation software, experimental rigs, satellites, scanners, etc. Such tools help scientists and engineers in data extraction, visualization, interpretation and analysis tasks, enabling them to experience a high degree of interaction and effectiveness in solving their design problems, which become more and more complex day by day. As the variety of today's visualization tools is diversifying, there is a need for their simultaneous use within different engineering software when solving multidisciplinary engineering problems. It is evident that such tools have to be available for a combined use, in order to eliminate many well known problems of sharing, accessing and exchanging design models and the related information content. It is shown that Object-Oriented methodology is a well adapted approach to stream the software development process of future engineering applications. The three European projects ALICE, LASCOT and SERKET are given as examples in which the evolving computer software technologies have been researched and demonstrated to address the evolution of the visualization software in engineering and for information visualization in general.*

Keywords *– scientific visualization, object orientation, multidisciplinary engineering*

1. VISUALIZATION SOFTWARE

Scientific visualization (SV) [1] is performed through specialized software [2], which combines visualization techniques to display and analyze scientific data. The scientific visualization methodology defines methods to manipulate and convert data into comprehensible images [3]. The scientific visualization process starts with transformation of data sets into geometric abstractions, which are further processed in displayable images, created by computer graphics algorithms [4]. Finally, human vision, possessing the highest bandwidth of human's information input, is exploited to understand the computer generated images.

In order to develop SV Software it is necessary to combine advanced Computer Graphics (CG) and User Interface (UI) technologies with engineering content. Thus, we need to consider and integrate the mentioned methodical domains, when addressing the software development of SV tools, as part of an integrated computational environment, see Figure 1, in order to efficiently support scientists/engineers at their work in the research laboratories and industry. In industry, visualization is used to gain a more quantitative understanding of the simulated phenomena (ex aerospace product design). The results of visualization are also used in management and commercial presentations. In contrast to industry, in a research laboratory, scientists develop codes and try to understand qualitatively how simulation algorithms behave. In this context, they tend to use SV as a debugging tool. In both cases, the computational environment includes software that supports a geometrical definition (as in CAD systems), mesh generation (pre-processing), supervision of the simulation (co-processing) and display and/or analysis of results (post-processing).

Interactive visualization accelerates the problem solving design cycle by allowing the user to 'jump' at will between the various phases, so as to optimize his/her analysis tasks. The user conducts an investigation in a highly interactive manner; he/she can easily compare variants of a simulation/analysis and may intuitively develop a deep understanding of the simulation and of calculation details. An example of an integrated environment application is the 'Virtual Wind Tunnel' [5], which reproduces a laboratory experiment in a virtual reality environment, where a virtual model can be created and put to test with dramatic cost and time savings compared to what is done in the 'real' laboratory.

SV software has progressed enormously during the past two decades. One reason is the exponential increase of the computer processing power, which has led to today's low-cost PCs clusters, providing as much

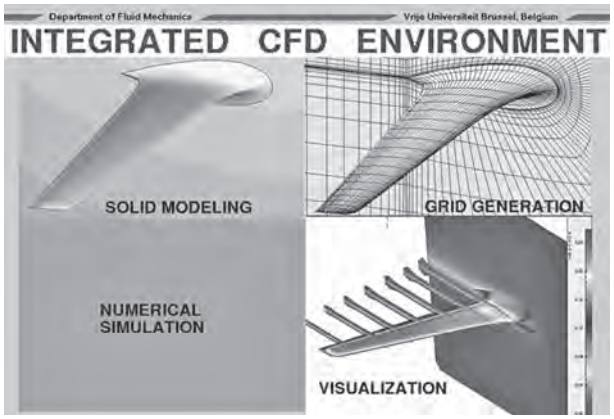

Fig. 1. Integrated Computational Environment

power as the high-end mainframes of some years ago. Development of advanced SV tools is no longer the prerogative of specialized labs with costly computer equipment. Yet, there is an undiminished demand for new visualization-enabled software, driven by continuous hardware changes and the emergence of new software platforms. Interactive visualization remains a key element of advanced engineering/scientific software, and their design must account for this fact. There are presently many commercial interactive visualization products on the market which provide SV functionality with increasing success. Such visualization systems are widely used in application areas as diverse as nuclear energy exploration and atmospheric research. In the field of engineering, such products are commonly used to visualize flow patterns and stress fields, and generally to study large multi-dimensional data sets. SV applications are used in many industries including aerospace, medicine, power production, shipbuilding, geophysics, automotive, electronics, oil, agriculture, food production, etc. SV applications are now ubiquitous in engineering and science, be it in:

- Fluid Mechanics,
- Structural Analysis,
- Electromagnetics,
- Thermodynamics,
- Nuclear Physics, etc.

For the sake of completeness, let us mention that SV has been (and is) instrumental in advancing the state of the art in industrial applications involving fluid flow modeling, such as:

- Aerodynamics of trains, cars and airplanes.
- Hydrodynamics of ships and floating structures.
- Flow in turbo-machinery and torque converters.
- Cryogenic rockets, combustion chambers simulations.
- Flow in manifold, pipes and machinery.
- Medical researches, circulation of blood in veins.

It is evident that advances in engineering software are driven by demands from many application areas, which in turn places requirements on the associated visualization software. Today, visualization software solutions with interactive 3D graphics capabilities can be categorized into four groups:

1. Visualization Applications
2. Modular Visualization Environments
3. Visualization Toolkits
4. Integrated Modeling Environments

A. Visualization Applications

Stand-alone visualization applications are software solutions, which offer direct functionality to the user, who is responsible for defining the data set required to be loaded for performing the visualization task. Some of the well known visualization software tools for the CFD and Finite Elements Analysis (FEA) are given in the following list:

- EnSight from CEI [6],
- FieldView from Intelligent Light's [7, 8],
- TecPlot from Amtec Engineering Inc. [9],
- CFView from NUMECA [10],
- PLOT 3D, NASA [11],
- VISUAL2-3 from MIT [12],
- ParaView from VTK [13],
- VisIt from Lawrence Livermore National Lab [14]

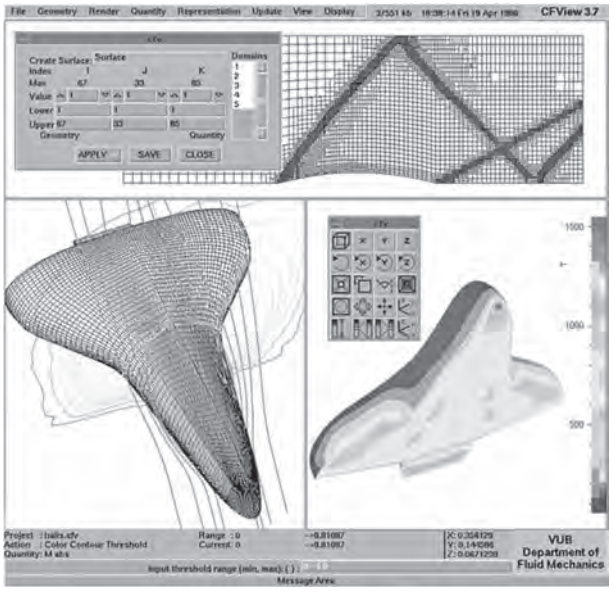

Fig. 2.: CFView the scientific visualization system

Such programs are appropriate for users who need off-the-shelf visualization functionality. Such software implements the 'event-driven' programming paradigm which is suitable where all functions are launched by the user interacting with the Graphical User Interface (GUI). This is the case for CFView [2]; see Figure 2, a scientific visualization application developed by the author over the 1988-98 period. CFView started as an academic application in 1988 and it was continuously upgraded in the following years. In the mid 90's, CFView was taken over by the VUB spin-off company NUMECA and integrated in 'FINE', that nicely illustrates the variety of visualization tasks that need to be performed to solve an engineering problem.

B. Modular Visualization Environments

Modular Visualization Environments (MVE) are programs often known as 'visualization programming environments'. Examples are [15]:

- Advanced Visual Systems AVS [16],
- Iris Data Explorer from Silicon Graphics [15, 17],
- OpenDX, the IBM's Data Explorer [18],
- PV Wave from Visual Numeric [19].

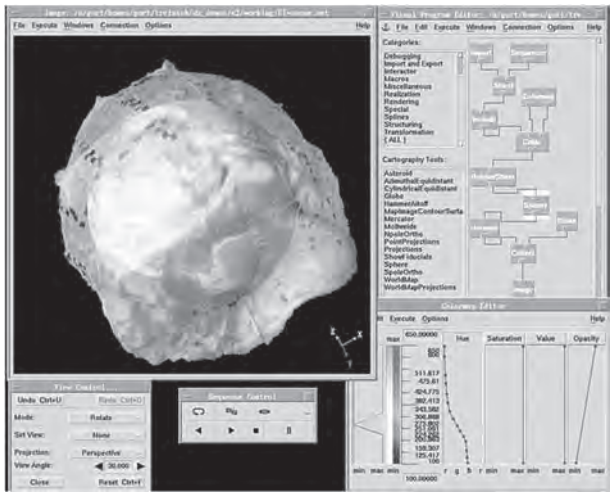

Fig. 3. The OpenDX Application Builder

Their most significant characteristic is the visual programming paradigm. Visual programming intends to give users an intuitive GUI for them to build customized visualization applications. The user graphically manipulates programming modules displayed as boxes, which encapsulate the available functionality. By interconnecting boxes, the user defines the data stream from one module to another, creating thereby the application. The MVE can be viewed as a 'visualization network' with predefined building blocks, which often needs to be quite elaborate in order to be useful to the user. The freedom given to the users to design their own visualization applications is the strength of so-called 'application builders'. This class of software implements the 'data flow paradigm', with a drawback that iterative and conditional constructs are difficult to implement. For example, PV Wave uses an interactive fourth-generation programming language (4GL) for application development, which supports conditional logic, data sub-setting and advanced numerical functionality in an attempt to simplify the use of such constructs in a visual programming environment. The interactive approach is usually combined with a script-oriented interface, and such products are not easy to use 'right out of the box' and have a longer learning curve than stand-alone applications.

There is an ongoing debate on whether the 'best' way to procure visualization software is to use stand-alone applications or to build applications using MVEs. Time has shown that both approaches are equally accepted as there is no alternative. The suggested visualization solution is a compromise between the previous and this one. For example, the GUI of CFView looks very much like the one of a stand-alone visualization application; internally though, CFView is an object-oriented system which has a flexible, modular architecture of the application builder. This is to say that a new component can be integrated in the core application structure with a minimum coding effort; also, the resulting effects from the modification propagation are kept limited.

A. Visualization Toolkits

Visualization Toolkits are general-purpose object-oriented visualization libraries, usually present as background components of SV applications. They emerged in the mid 1990's, and the two representative examples are VTK[20] and VisAD[21]:

The Visualization ToolKit (VTK) is an open-source software system for 3D computer graphics, image processing and visualization, now used by thousands of researchers and developers in the world. VTK consists of a C++ class library and several interpreted interface layers including Tcl/Tk, Java, and Python. VTK supports a wide variety of visualization algorithms (including scalar, vector, tensor, texture and volumetric methods), advanced modeling techniques (such as implicit modeling, polygon reduction, and mesh smoothing, cutting, contouring and Delaunay triangulation). In addition, dozens of imaging algorithms have been directly integrated to allow the user to mix 2D imaging / 3D graphics algorithms and data.

The VISualization for Algorithm Development (VisAD) is a Java component library for interactive and collaborative visualization and analysis of numerical data. VisAD is implemented in Java and supports distributed computing at the lowest system levels using Java RMI distributed objects. VisAD's general mathematical data model can be adapted to virtually any numerical data that supports data sharing among different users, different data sources and different scientific disciplines, and that provides transparent access to data independent of storage format and

location (i.e. memory, disk or remote). A general display model supports interactive 3D, see Figure 4, data fusion, multiple data views, direct manipulation, collaboration, and virtual reality. The display model has been adapted to Java3D and Java2D, and virtual reality displays.

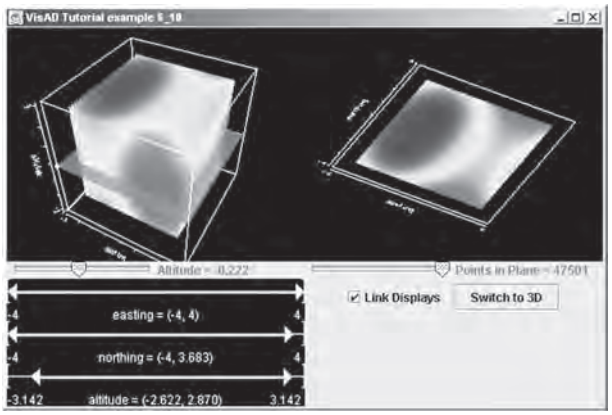

Fig. 4. VisAD application example

B. Integrated Modeling Environments

Integrated Modeling Environments (IME) is software that combines two or more engineering applications and visualization systems to solve a multi-disciplinary problem. For example, the naval architect shapes the ship hull in order to reduce the ship's hydrodynamic drag, while the stress engineer calculates the ship's steel structure. Both use visualization to analyze the data generated by the hydrodynamics and stress calculation solvers. The visualization software may be able to process the CFD flow-field solver data and the FEA stress-field solver data in a unified manner, giving the two engineers the possibility to work in a compatible way, interfacing simultaneously 3D representations of hydrodynamic and structural problems. An example of such integration is the Product Life-cycle Modeling (PLM) developed by Dassault Systèmes and the CFD solver technology developed by ANSYS, Inc., where the FLUENT CFD flow modeling approach is integrated in CATIA CAD tools throughout the whole product lifecycle [22].

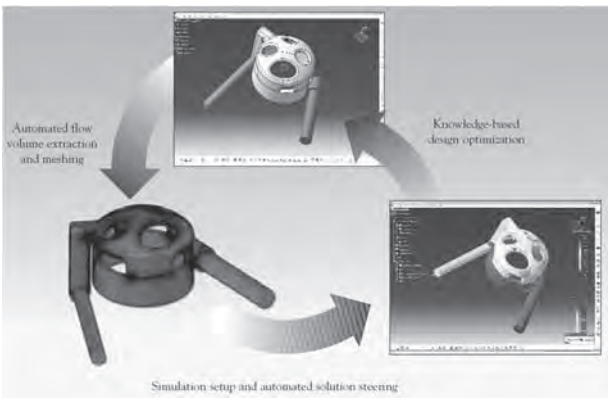

Fig. 5. The integrated modeling environment from Dassault Systèmes and ANSYS, Inc.

2. OBJECT ORIENTED METHODOLOGY

Computer hardware has improved drastically in quality and performance in the last 30 years, much faster than software quality and complexity. The trend is drawn qualitatively in Figure 6. The main reason for this situation is to be found in the reusability of hardware components (chips), which are the cheap and reliable building blocks of hardware systems, small and large. To date, software components with similar properties simply do not exist, and reusable software 'chips' are not commercially available. The effort to design and produce such software would be too large, and standardization is not pursued by software makers who keep customers captive with proprietary software and computer platforms. As a result, software production cannot keep pace with hardware technology, a situation often recognized as symptomatic of a 'software crisis'. The key idea is to try and produce visualization software that could intrinsically evolve as fast and as cheaply as hardware.

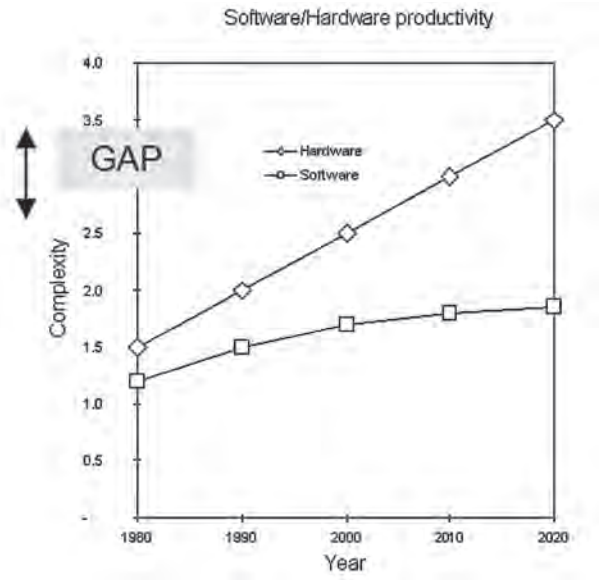

Fig. 6. Comparison of Hardware/Software productivity

In this respect *Object Oriented Methodology* (*OOM*) for constructing software components is a well adopted approach to be considered, as it is a fairly universal approach that can be applied to solve many types of complex problems. The goal of *OOM* is to reduce the system complexity by decomposing it in manageable components called *objects*. Experience has shown that solving problems in a piece-wise manner leads to better quality and easily scalable solutions. The system is 'cut' into component pieces represented by 'objects' that interact through well-defined interfaces, by exchanging information through *messages*. An interesting feature of *OOM* is that objects can be created and developed independently, even with no a priori knowledge of the application in which the objects will be used. The existence of an object is independent of any specific applica-

tion. An interesting consequence of having many reusable software objects would be that it would then make sense to get hardware designed to fit the available software (and not the reverse as is the case today). The principles of software reusability and portability are fundamental to foster software productivity. Reusability is an intrinsic feature of all *OO* software and their efficient exploitation promotes the computer network to become a commercial market place, as the Internet, in which such general-purpose and specialized software components need to be available, validated and marketed [23].

The OO approach has led to the emergence of *Object Oriented Programming* (*OOP*) with specialized *OO* programming languages, such as *Smalltalk [24], CLOS, Eiffel [25-27], Objective C [28], C++ [29], Java, C#* and other derivatives, which apply encapsulation and inheritance mechanisms to enhance software **modularity** and improve component **reusability**. It is important to stress that the greatest benefit of *OOM* is obtained when *OOM* covers the full software life-cycle, from the requirements specification phase to the software delivery phase. When an application is created applying *OOM*, reusability in different development phases can be expected. First, the *OOP* brings in object-oriented libraries, which provide components validated in previously developed applications. Second, software design of previously modeled software could be reused through the established design patterns. Previously developed components may be reused for a new application which does not need to be designed from scratch, which is an obvious advantage. Improvements that could be brought to the existing, re-used objects would also improve the 'older' applications that use the same objects.

It is interesting to note that the *OOP* paradigm has shifted the emphasis of software design **from algorithms to data** (object, class) **definitions** [30-32]. The object-oriented approach can be summarized in three steps. The system is first decomposed into a number of objects characterizing the problem space. The properties of each object are then defined by a set of methods. Possibly, the commonality between objects is established through inheritance. Actions on these objects and access to encapsulated data can be done randomly rather than in a sequential order. Moreover, reusable and extensible class libraries can be created for general use. These are the features which make *OOP* very attractive for the development of software, in particular for interactive software.

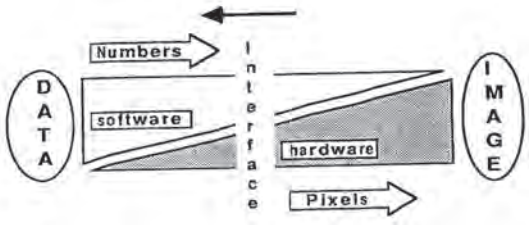

Fig. 7. Graphics Engine as a combined software/hardware solution

It should be mentioned that *OOM* does not directly reduce the cost of software development; however, it markedly improves the quality of the code by assuring consistent object interfaces across different applications. Estimated software construction times are often incorrect. **Time** and **resource** allocation tend to be largely underestimated in software projects, not uncommonly by factors of 2 to 5, especially where innovative features are to be developed. Unfortunately, for software construction planning we do not have an underlying engineering, scientific or mathematical model to calculate the software development time required, when starting a new software development process. The theoretical basis of how to best construct software does not exist. The ability to plan project costs, schedule milestones, and diagnose risk is ultimately based on experience, and could be only valid for a very similar application done in the past and applying the same development environment.

It is also important to ensure the production of **portable** code, i.e. a code that can run without need of adaptation on computing platforms other than its 'native' platform. Porting, adapting software to a computer system other than the one for which it was originally designed, can be a tedious and costly process. Portability can be improved by adopting standards supported by various hardware/system platforms. For example, one may adopt the OpenGL standard which is supported by graphic boards. This ensures that only a small kernel of code must be modified before recompilation for another hardware platform. A graphics engine typically processes floating-point input data to generate graphics. An example of graphics data models are lines and polygons. Hence, one assumes that line drawing and polygon filling are functions provided by the graphics engine, and one needs not be concerned with developing low-level graphics routines. One can therefore focus on generating the data sets needed to 'feed' the graphics engine.

To develop the visualization software, our approach must be 'multi-disciplinary' in the sense that it puts together an application engineer and a computer specialist in order to develop different application layers, as shown in Figure 8. The software development environment needs to enable evolution of the software under development and has to provide a framework for porting applications across different hardware/operating systems/windowing systems. Also, it has to simplify the process of creating interactive graphical applications, enabling the application engineer to have the application software layer under control and hide the lower software layers of the system, as depicted in Figure 8. Thus, the object-oriented approach is appropriate to introduce necessary abstraction levels and for organizing the inherent complexity present in the development of the scientific visualization software.

The fundamental concept in *OOM* is the "*object*"; it is the elementary 'building block' for mapping scientific and engineering concepts to their software equivalents. The object is an abstract construct, which ap-

proximates (in a simplified manner) the understanding of the real concept under consideration, which is often quite complex. Consider, for example, how physics of fluid flows is described in terms of numerical equations and how these equations are modeled by software objects. These objects are useful because they are identifiable elements with a well-defined purpose: each object performs a given function by encompassing a certain mathematical or physical 'intelligence' For example, an object modeling a second-order differential equation, or an object modeling the viscosity of a liquid at a given temperature, etc. such that it can be 'reused' by the software engineer with no need to understand the internal working details of the object. The obvious reused object in real life is a car. We need it to go from one place to another, but we do not need to know how it is built. We use it, and this is the way software engineers are supposed to reuse objects.

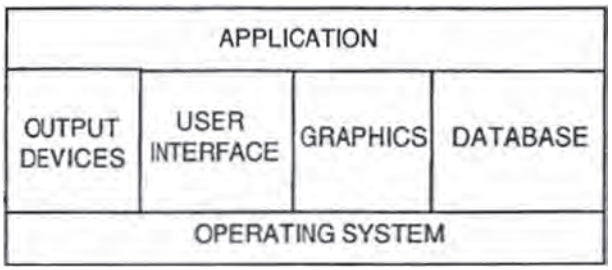

Fig. 8. Software components distribution

The fundamental concept in *OOM* is the "*object*"; it is the elementary 'building block' for mapping scientific and engineering concepts to their software equivalents. The object is an abstract construct, which approximates (in a simplified manner) the understanding of the real concept under consideration, which is often quite complex. Consider, for example, how physics of fluid flows is described in terms of numerical equations and how these equations are modeled by software objects. These objects are useful because they are identifiable elements with a well-defined purpose: each object performs a given function by encompassing a certain mathematical or physical 'intelligence' For example, an object modeling a second-order differential equation, or an object modeling the viscosity of a liquid at a given temperature, etc. such that it can be 'reused' by the software engineer with no need to understand the internal working details of the object. The obvious reused object in real life is a car. We need it to go from one place to another, but we do not need to know how it is built. We use it, and this is the way software engineers are supposed to reuse objects.

The *software model* is a fundamental element in *OOM* software development. The model describes the knowledge mapped in the software in a formal, unambiguously defined manner. Such a precise specification is both a documentation and a communication tool between developers and users; recall that the term 'developer' includes application analysts, software designers and coding programmers (see Figure 9).

In the software development process, the analyst creates an abstract model that will be partially or fully implemented. The designer uses that model as a basis to add specific classes and attributes to be mapped onto one or more OOP languages. The designer specifies the detailed data structure and functional operations/processes, which are required by the application specification

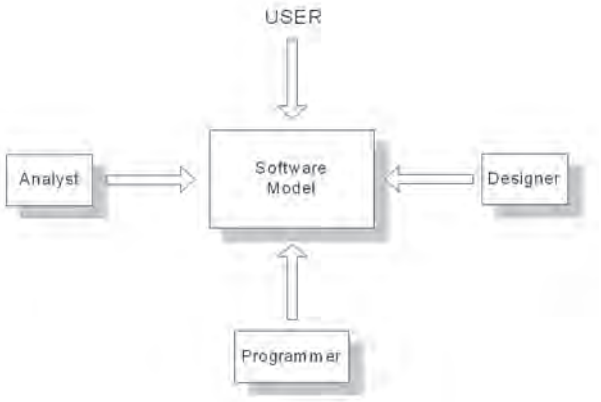

Fig. 9. Software model as communication media in the software development process

Finally, the programmer receives the analyst's and the designer's models for implementation into source code. The source code is compiled to produce the executable software. Software modeling is then an iterative and incremental process which maps abstract concepts into formal constructs that eventually become reusable software entities.

In *OOM*, the object model comprises a data model and a functional model. Specification of an object includes a description of its behavior and the data necessary and sufficient to support its expected functionality. The data model describes pertinent data structures, relations between the objects and the constraints imposed on the objects. The functional model describes objects' behavior in terms of operations. From the data model point of view, the primary concern is to represent the structures of data items important to the scientific visualization process and the associated relationships.

3. THREE EUROPEAN PROJECTS

The three European projects ALICE, LASCOT and SERKET are given as examples in which the evolving computer software technologies have been researched and demonstrated to address the evolution of the visualization software in engineering and for information visualization in general.

A. Alice – QFView – towards the transparent visualization of numerical and experimental data sets

The development of QFView in the ESPRIT-IV "ALICE" project (EP-28168) extended author's research towards using the World Wide Web for designing and building up distributed, collaborative scientific environments [33, 34]. QFView was developed in a web-oriented client-server architecture (e.g. Java, JDBC) which allowed openness and modularity, as well as improved flexibility and integration of visualization components (current and future). A core element was creation of a central database where very large data sets were imported, classified and stored for re-use. The distributed nature of QFView allows the user to extract, visualize and compare data from the central database using World Wide Web access. QFView integrates experimental and computational data processing (e.g. flow field mappings with flow field visualization), see Figure 10.

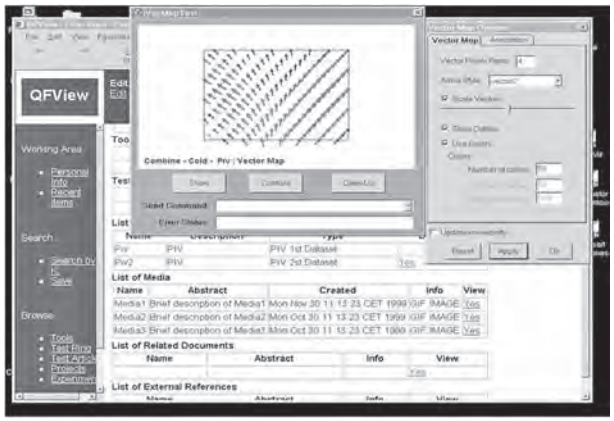

Fig. 10. QFView Web Interface

B. LASCOT –Visualization as a decision-making aid

The LASCOT project [35] is part of the EUREKA/ITEA initiative. The Information Technology European Advancement (ITEA) program for research and development in middleware is jointly promoted by the Public Authorities in all EU Members States and some large European industrial companies.

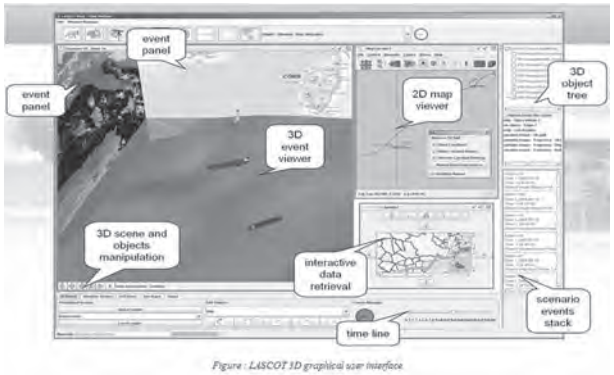

Fig. 11. LASCOT 3D graphical user interface

The goal of LASCOT was to design, develop and demonstrate the potential benefits of distributed collaborative decision-support technology to the "future cyber-enterprise in the global economy" demonstrating the following issues:

- Support access to traditional information systems and to Web data;
- Enable situation assessment and provide decision-support facilities as well as simulation and validation facilities to support business decisions;
- Include current, enhanced-as-required security tools;
- Make use of visualization technology for critical tasks such as decision-making and knowledge management;
- Produce an online learning application to facilitate embedding of the platform by the users.

C. SERKET – Security situation awareness

The SERKET project [36] explored a solution to the issue of security in public areas and events by developing an innovative system whereby dispersed data from a variety of different devices are automatically correlated, analyzed and presented to security personnel as 'the right information at the right time'. The aim was to design and develop an open-software platform that can be deployed at low cost.3D software development in SERKET is centered on the visualization and presentation engine, with special attention placed on the application of X3D (*eXtensible 3D*) and XML (*eXtensible Markup Language*) standards. The graphical middleware correlates, combines, annotates and visualizes sensor data and related metadata (the application context is security). Using sensor data analyzed by other processing and data fusion components, the graphical middleware builds 3D scenes which represent the objects detected by the sensors and the operational status of sensors at their locations. Objects in the 3D scenes are annotated with metadata and/or with links to metadata describing the security context in relation to the displayed 3D objects. The 3D display of the situation removes ambiguous and provides a highly understandable overview of the situation to the security end-user, who is able to switch between different levels of viewing details and select desired viewpoints at each level (locations of video cameras define the available viewpoints). The 3D model of situation-security awareness is parameterized in space and time as shown in Figure 13.

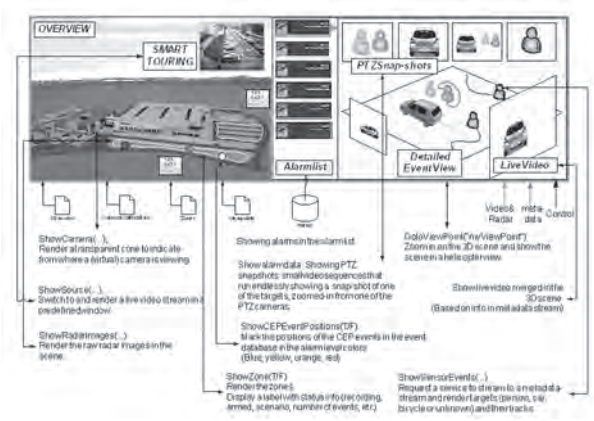

Fig. 12. The SERKET application

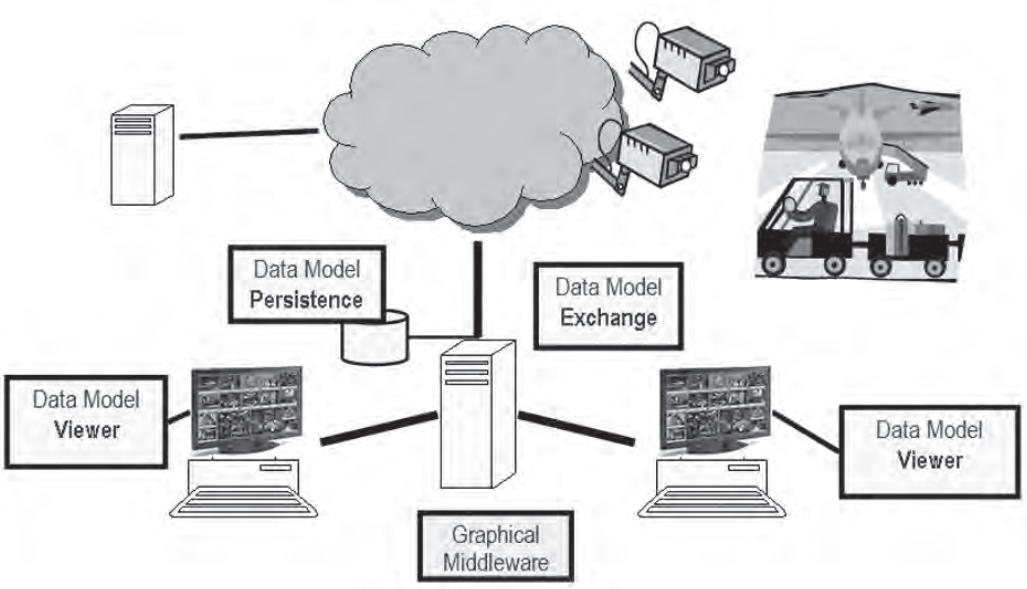

Fig. 13. The SERKET architecture overview

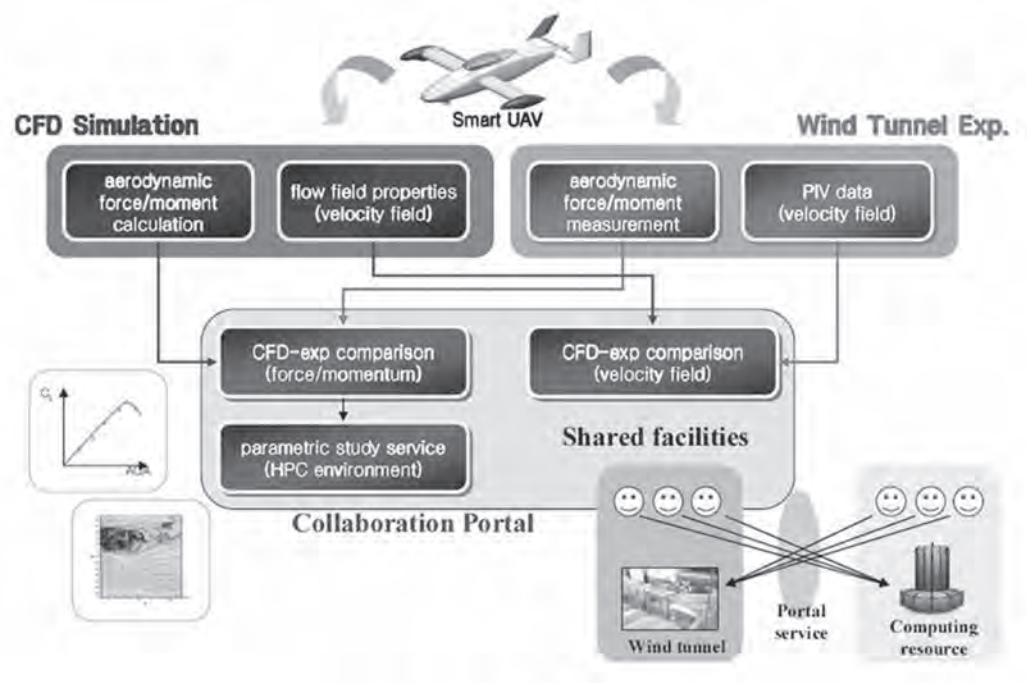

Fig. 14. Example of an Integrated Modeling Environment [37]

4. TOWARDS INTEGRATED MULTI-DISCIPLINARY ENVIRONMENTS

Today's trend in software development is towards more intelligent, multi-disciplinary systems. Such systems are expected to capture engineering intelligence and put in the hands of the engineer advanced tools for designing new products or performing investigations. The Integrated Modeling Environment (IME) [38] concept is quite recent, yet its roots can be found in 1st-generation CAD-CAM tools. An IME system attempts to offer to the engineer a homogeneous working environment with a single interface from which various simulation codes and data sets can be accessed and used. In the fluid mechanics application area, an IME system needs to integrate the latest CFD and EFD 'good working practice'; the system must be constantly updated so that at any time it runs on the most-recent software/hardware platform, see Figure 14.

An IME system consists of an Internet portal from which the investigator is able to access information/ knowledge /databases and processing functions, at any time and wherever they are located/stored. He/she has access to accurate and efficient simulation services, for example to several *CFD* solvers. Calculations can be performed extremely fast and cheaply where solvers are implemented as parallel code, and grid computing resources are available. Results obtained can be compared with separate experimental results and other computations; this can be done efficiently by accessing databases that manage large collections of archived results. The possibilities for benchmarking and exchanging knowledge and opinions between investigators are virtually infinite in an IME environment. Clearly though, a prerequisite for an *IME* environment to work is its adoption by its user community, which agrees on a specific codex that enables and guarantees openness and collaboration. Typically, an *IME* system will open Web-access to:

- Computational Services: selection of simulation software and access to processing and storage resources,
- Experimental Services: access to experimental databases with a possibility to request new measurements,
- Collaborative Services: chat and video-conferencing, with usage of shared viewers (3D interactive collaboration).

Visualization is required to support many tasks in *IME* software. This poses the problem of building/selecting data models that can be used by visualization components to present the information correctly to the users, whilst offering to them tools for real-time interaction in a natural, intuitive manner. The *IME* can include wall-displays connected to high-performance, networked computing resources. Such systems and architectures are no longer a mere vision: they are becoming reality, which opens new challenges for scientific visualization software researchers and developers. In Figure 15 and Figure 16 large multi-tiled display walls driven by a system for parallel rendering running on clusters of workstations (e.g. Chromium [39]) can adequately satisfy the requirements of high resolution large-scale visualization systems.

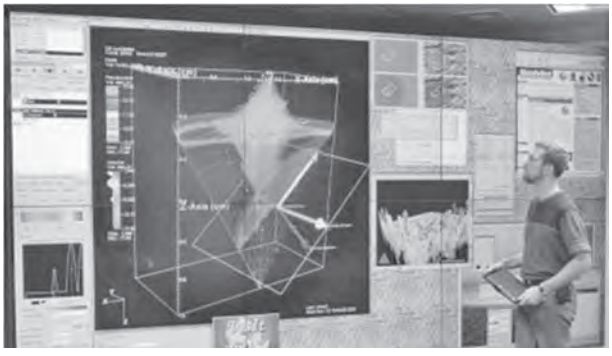

Fig. 15. Scientific visualization with Chromium

Fig. 16. NASA Space Station on display wall

5. CONCLUSION

Innovation in visualization systems poses simultaneous challenges of: building better, faster and cheaper computer-aided solutions to ever more complex scientific, engineering and other multi-disciplinary problems; developing sophisticated methodologies and algorithms; harnessing the power of upcoming technologies; re-using and leveraging the power of legacy systems and solutions; and working in increasingly shorter design and production cycles.

The paper addresses author's research over many years, in which the continuous intention was to combine engineering and computer science domains, trying to contribute to the improvements in software development methodology for constructing scientific visualization software, whose role in the multidisciplinary engineering environment today has become an obvious prerequisite. The paper describes the problem of advancing the state-of-the-art of scientific visualization systems using object-oriented methodologies and programming techniques, which are found appropriate for designing and building interactive visualization systems that meet all the requirements placed on them by engineering disciplines: correctness, accuracy, flexibility, performance, as well as by computer science disciplines: compatibility, reusability, portability. In particular, we have shown the three European project examples whose high degree of interactivity and user-friendliness can be achieved with such software solutions. More importantly, we have provided evidence that scientific visualization has deeply changed the very nature of the investigative process itself by allowing the researcher to explore and view the physical world in an intuitive, interactive and deeply illuminating manner.

The next generation engineering visualization tools will more and more associate semantic information to 3D models. They will engage web-based software standards like X3D (*eXtensible 3D)* and Semantic Web, in order to enhance visualization and manipulation of the graphical content in a distributed engineering network. The envisaged software architecture will support ontologies: to interface knowledge-based systems, to promote a web-based software solution and to enable automation of perpetual engineering tasks.

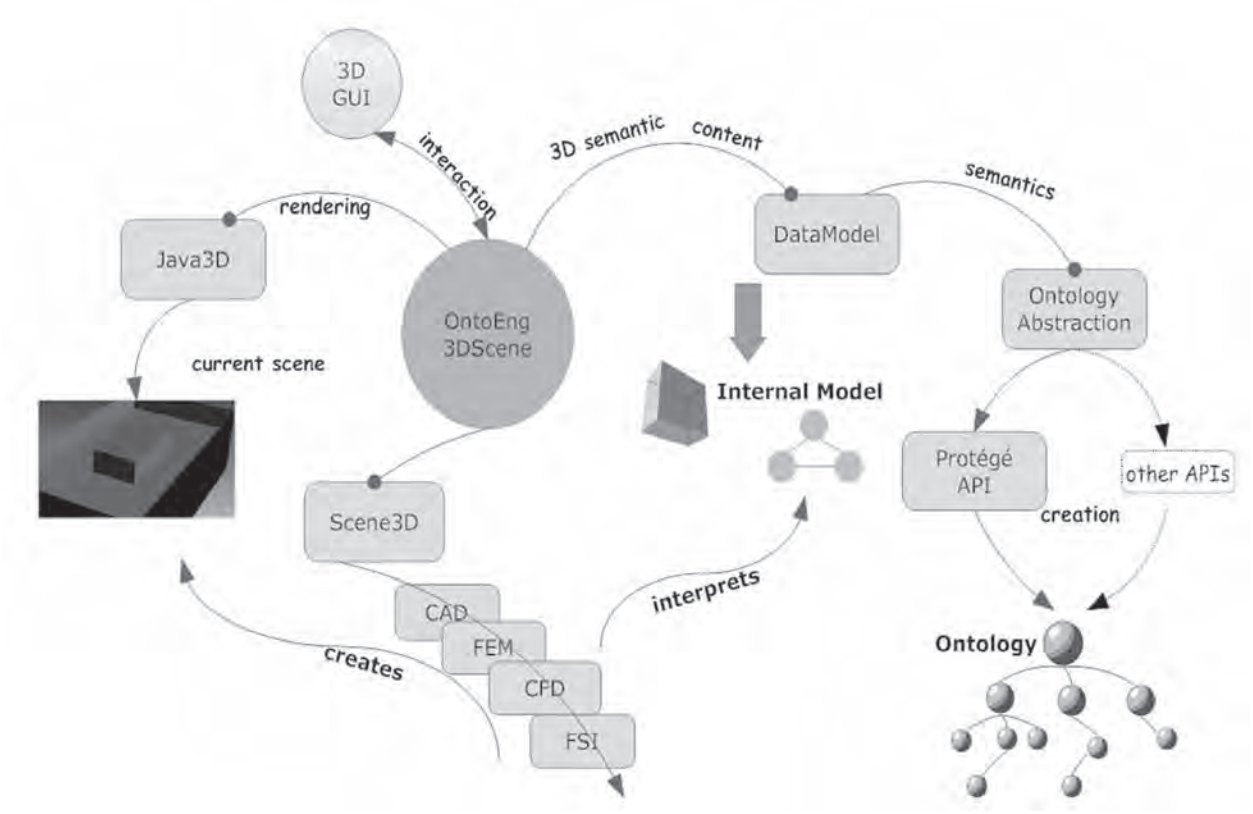

Fig. 17. Architecture overview of the ontology based visualization [40]

ACKNOWLEDGMENT

This paper would not have been created if the long-lasting research and development activity of Dean Vucinic had not been supported by the European Commission (EC) for the ALICE project (EP-28168) (1988-2001) and the Belgian national authorities (IWT) in collaboration with the EC for the ITEA projects LASCOT (2003-2005) and SERKET (2006-2007), what is gratefully acknowledged by the author.

REFERENCES

[1] M. Göbel, H. Müller, B. Urban, Visualization in scientific computing. Vienna; New York: Springer-Verlag, 1995.

[2] D. Vucinic, M. Pottiez, V. Sotiaux, C. Hirsch, "CFView - An Advanced Interactive Visualization System based on Object-Oriented Approach," in AIAA 30th Aerospace Sciences Meeting Reno, Nevada, 1992.

[3] D. Vucinic, "Development of a Scientific Visualization System", in Department of Mechanical Engineering, PhD Thesis: Vrije Universiteit Brussel, 2007.

[4] J. D. Foley, Computer graphics: principles and practice, 3rd ed.: Addison-Wesley Publ., 2006.

[5] A. B. Hanneman, R. E. Henderson, "Visualization, Interrogation, and Interpretation of Computed Flow Fields – Numerical Experiments," in AIAA Modeling and Simulation Technologies Conference, Denver, CO: AIAA-2000-4089, 2000.

[6] "Ensight, CEI Products Overview - extreme simulation software", in http://www.ensight.com/product-overview.html: Computational Engineering International (CEI) develops, markets and supports software for visualizing engineering and scientific data, 2007.

[7] E. Duque, S. Legensky, C. Stone, R. Carter, "Post-Processing Techniques for Large-Scale Unsteady CFD Datasets", in 45th AIAA Aerospace Sciences Meeting and Exhibit Reno, Nevada, 2007.

[8] S. M. Legensky, "Recent advances in unsteady flow visualization", in 13th AIAA Computational Fluid Dynamics Conference Snowmass Village, CO, 1997.

[9] D. E. Taflin, "TECTOOLS/CFD - A graphical interface toolkit for network-based CFD", in 36th Aerospace Sciences Meeting and Exhibit Reno, NV, 1998.

[10] "CFView a visualization system from Numeca," http://www.numeca.com, 2007.

[11] P. P. Walatka, P. G. Buning, L. Pierce, P. A. Elson, "PLOT3D User's Manua," NASA TM-101067 March 1990.

[12] R. Haimes, M. Giles, "Visual3 - Interactive unsteady unstructured 3D visualization", in 29th Aerospace Sciences Meeting Reno, NV, 1991.

[13] "ParaView – Parallel Visualization Application", in http://www.paraview.org, 2004.

[14] B. J. Whitlock, "Visualization with VisIt", California, Lawrence Livermore National Laboratory: http://www.llnl.gov/visit/home.html, 2005.

[15] J. Walton, "NAG's IRIS Explorer", in Visualization Handbook, C. R. J. a. C. D. Hansen, Ed.: Academic Press, 2003.

[16] C. Upson, "Scientific visualization environments for the computational sciences", in COMPCON Spring '89. Thirty-Fourth IEEE Computer Society International Conference: Intellectual Leverage, Digest of Papers., 1989, pp. 322-327.

[17] D. Foulser, "IRIS Explorer: A Framework for Investigation", Computer Graphics, vol. 29(2), pp. 13-16, 1995.

[18] "OpenDX is the open source software version of IBM's Visualization Data Explorer", http://www.opendx.org/, 2007.

[19] "PV-WAVE, GUI Application Developer's Guide", USA: Visual Numerics Inc., 1996.

[20] W. Schroeder, K. W. Martin, B. Lorensen, The visualization toolkit, 2nd ed. Upper Saddle River, NJ: Prentice Hall PTR, 1998.

[21] W. Hibbard, "VisAD: Connecting people to computations and people to people", in Computer Graphics 32, 1998, pp. 10-12.

[22] "Fluent for Catia V5, Rapid Flow Modeling for PLM", http://www.fluentforcatia.com/ffc_brochure.pdf, 2006.

[23] B. J. Cox, A. J. Novobilski, Object-oriented programming: an evolutionary approach, 2nd ed. Reading, Mass.: Addison-Wesley Pub. Co., 1991.

[24] A. Goldberg, D. Robson, Smalltalk-80: the language. Reading, Mass.: Addison-Wesley, 1989.

[25] B. Meyer, Reusable software: the Base object-oriented component libraries. Hemel Hempstead: Prentice Hall, 1994.

[26] B. Meyer, Eiffel: the language. New York: Prentice Hall, 1992.

[27] B. Meyer, Object-oriented software construction. London: Prentice-Hall International, 1988.

[28] L. J. Pinson, R. S. Wiener, Objective-C : object-oriented programming *techniques*. Reading, Mass.: Addison-Wesley, 1991.

[29] B. Stroustrup, *The C++ Programming Language*, Special Edition ed.: Addison Wesley, 1997.

[30] G. D. Reis, B. Stroustrup, "Specifying C++ concepts", in *Conference record of the 33rd ACM SIGPLAN-SIGACT symposium on Principles of programming languages,* Charleston, South Carolina, USA: ACM Press, 2006.

[31] B. Stroustrup, "Why C++ is not just an object-oriented programming language", in *Addendum to the proceedings of the 10th annual conference on Object-oriented programming systems, languages, and applications (Addendum),* Austin, Texas, United States: ACM Press, 1995.

[32] R. Wiener, "Watch your language!," *Software, IEEE,* vol. 15, pp. 55-56, 1998.

[33] D. Vucinic, J. Favaro, B. Sünder, I. Jenkinson, G. Tanzini, B. K. Hazarika, M. R. d'Alcalà, D. Vicinanza, R. Greco, A. Pasanisi, "Fast and convenient access to fluid dynamics data via the World Wide Web", in *ECCOMAS European Congress on Computational Methods in Applied Sciences and Engineering 2000,* Barcelona, Spain, 2000.

[34] D. Vucinic, M. R. Barone, B. Sünder, B. K. Hazarika, G. Tanzini, "QFView - an Internet Based Archiving and Visualization System", in *39th Aerospace Sciences Meeting & Exhibit,* Reno, Nevada, 2001.

[35] "LASCOT project - home page", in *http://www.bull.com/lascot/index.html*, Bull, Ed., 2005.

[36] "SERKET project - home page," http://www.research.thalesgroup.com/software/cognitive_solutions/Serket/index.html, Ed.: Thales Research & Technology, 2006.

[37] M.-J. Jeong, K. W. Cho, K.-Y. Kim, "e-AIRS: Aerospace Integrated Research Systems", in *The 2007 International Symposium on Collaborative Technologies and Systems (CTS'07),* Orlando, Florida, USA, 2007.

[38] C. M. Stone, C. Holtery, "The JWST integrated modeling environment", 2004, pp. 4041-4047, Vol.6.

[39] G. Humphreys, M. Houston, Y.-R. Ng, R. Frank, S. Ahern, P. Kirchner, J. T. Klosowski, "Chromium: A Stream Processing Framework for Interactive Rendering on Clusters", in *SIGGRAPH*, 2002.

[40] D. Vucinic, M. Pesut, A. Aksenov, Z. Mravak, C. Lacor, "Towards Interoperable X3D Models and Web-based Environments for Engineering Optimization Problems", in *International Conference on Engineering Optimization,* Rio de Janeiro, Brazil, 2008.

Radiation Pattern of Waveguide Antenna Arrays on Spherical Surface - Experimental Results

Slavko Rupčić, Vanja Mandrić, Davor Vinko
J.J.Strossmayer University of Osijek, Faculty of Electrical Engineering, Osijek, Croatia
slavko.rupcic@etfos.hr, vanja.mandric@etfos.hr, davor.vinko@etfos.hr

Abstract *– In this paper, the radiation pattern of two experimental models of circular waveguide antenna arrays on spherical surface is obtained experimentally and compared with theoretical patterns. We have omitted the phase delay of feed system signals because we have only compared measured and theoretical results in order to verify theoretical results, without trying to improve the best radiation characteristics of developed experimental models. Analysis was made with a developed moment method (MoM) program. The spectral-domain approach to the analysis of the spherical antenna arrays is briefly presented in the paper. Measurements were not performed in a well-defined anechoic environment.*

Keywords *– radiation pattern, differential radiation pattern, antenna array, spherical array, waveguide*

1. INTRODUCTION

An array of antennas disposed on the surface of a sphere is of importance because such an array provides wide hemispherical scan coverage with low grating lobe levels. Spherical array antennas combine the capabilities of array antennas with the optimal geometry to achieve omni-directional coverage.

Thus, spherical arrays are an attractive solution and an optimal choice for satellite tracking, telemetry and command applications.

At the present time little information is available on the radiation characteristics of spherical antenna arrays.

The array was modeled using a previously presented computer program based on the method of moments in spectral domain [8].

In the process of verifying theoretical results we built two experimental models and validated theoretical results by comparing the results to the measurements performed on the developed laboratory models.

We also discuss the results of an experimental investigation of two spherical arrays consisting of circular waveguide elements with apertures on a hemispherical ground plane.

2. FAR FIELD CALCULATION

Conformal antennas and periodic structures are frequently analyzed by means of the electric field integral equation and the moment method. The kernel of the integral operator is Green's function, which is different for different structures.

An electrical field radiated by the current shell on the spherical surface in homogeneous media is:

$$\mathbf{E}(r,\theta,\varphi)=\sum_{m=-\infty}^{\infty}\sum_{n=|m|}^{\infty}\overline{\overline{\mathbf{L}}}(n,m,\theta)\cdot\overline{\overline{\tilde{\mathbf{G}}}}\ (n,m,r\,|r_s)\tilde{\mathbf{M}}(r,n,m)\ e^{jm\varphi} \quad (1)$$

where $\overline{\overline{\tilde{\mathbf{G}}}}(n,m,r|r_s)$ is a spectral domain dyadic Green's function for a grounded spherical surface and $\overline{\overline{\mathbf{L}}}(n,m,\theta)$ is the kernel of the vector-Legendre transformation. $\tilde{\mathbf{M}}(r,n,m)$ is a spectral domain equivalent magnetic current placed at the open of each waveguide [5], [6].

The appropriate spectral-domain Green's function of a multilayer spherical structure is calculated using the G1DMULT algorithm [1], [2].

The radiation pattern of the array is obtained as a superposition of fields excited by each waveguide aperture (placed on a spherical surface at the point with coordinate (α_n,β_n)) :

$$E_{\theta,\alpha_n,\beta_n}(\theta,\phi)=-\frac{\cos\theta\sin\alpha_n\cos(\phi-\beta_n)-\sin\theta\cos\alpha_n}{\sin\theta'}E_\theta(\theta',\phi')$$

$$-\frac{\sin\alpha_n\sin(\phi-\beta_n)}{\sin\theta'}E_\phi(\theta',\phi) \quad (2)$$

$$E_{\varphi,\alpha_n,\beta_n}(\theta,\varphi)=\frac{\sin\alpha_n\sin(\varphi-\beta_n)}{\sin\theta'}E_\theta(\theta',\varphi')$$

$$-\frac{\cos\theta\sin\alpha_n\cos(\varphi-\beta_n)-\sin\theta\cos\alpha_n}{\sin\theta'}E_\varphi(\theta',\varphi') \quad (3)$$

where α_n and β_n are the θ and ϕ coordinate of each antenna element in the global coordinate system [3], [4].

We introduced local coordinate systems with the origin located at the center of each antenna element (shown in Fig.1).

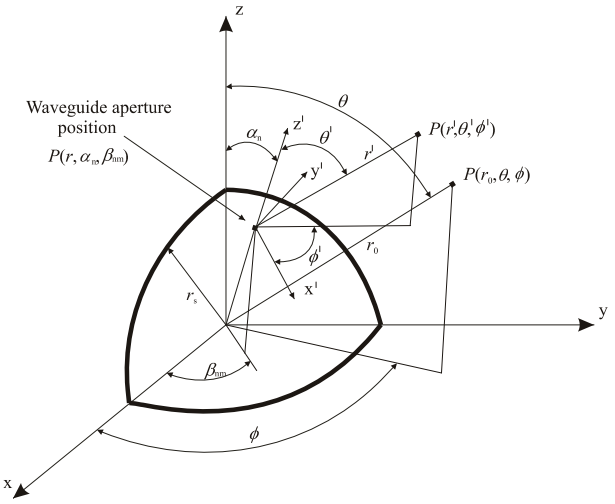

Fig. 1. Global and local coordinate system.

The complete pattern expression of the field produced by the array is given as:

$$\mathbf{E}(\theta,\varphi) = \sum_{n,m} \mathbf{E}_{\alpha_n \beta_{nm}}(\theta,\varphi) \tag{3}$$

3. EXPERIMENTAL MODELS OF A SPHERICAL ARRAY

The considered antennas are designed with circular waveguides used as antenna elements placed on the spherical structure. The antenna elements are placed at equidistant position on the (grounded) surface of the icosahedron.

The first array (MODEL I – shown in Fig. 2.) design specifications are:

- first waveguide position: α_1=0, β_{11}=0;
- second waveguide position: α_2=18°, β_{21}=90°;
- radii: r_s=69 cm and r_w=6 cm.

The second array (MODEL II – shown in Fig. 3.) design specifications are:

- first waveguide position: α_1=0, β_{11}=0;
- second ring waveguide position: α_2=56°, β_{21}=36°, β_{22}=108°, β_{23}=180°, β_{24}=252°, β_{25}=324°
- radii: r_s=30 cm and r_w=6 cm.

Further, normalized free-space radiation patterns were calculated and measured at the frequency f = 1.75 GHz .

Fig. 2. Spherical experimental model (MODEL I) with two waveguides (α_1=0 ^{0}, β_{11}=0 ^{0}, α_2=18 ^{0}, β_{21}=90 ^{0}).

Fig. 3. Spherical experimental model (MODEL II) with six waveguides (α_1=*0* ^{0}, β_{11}=*0* ^{0}, α_2=*56* ^{0}, β_{21}=*36* ^{0}, β_{22}=*108*^{0}, β_{23}=*180*^{0}, β_{24}=*252*^{0}, β_{25}=*324*^{0}).

4. THEORETICAL AND MEASURED RESULTS

Consider an antenna arrays transmitting a wave into the far field region where strength of its field is to be measured. All the array elements (waveguides) are excited in same phase with uniform amplitude. The antenna arrays were oriented in a fixed position and both E- and H- plane patterns have been recorded. The radiation patterns produced by two experimental models were measured over the azimuthal angle ranging from -90^0 to 90^0.

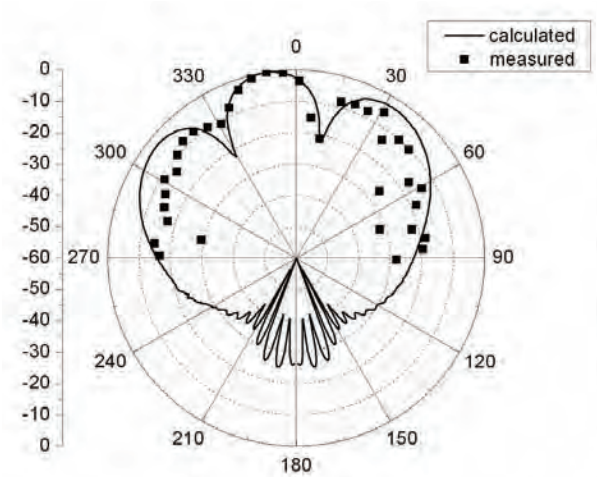

(a)

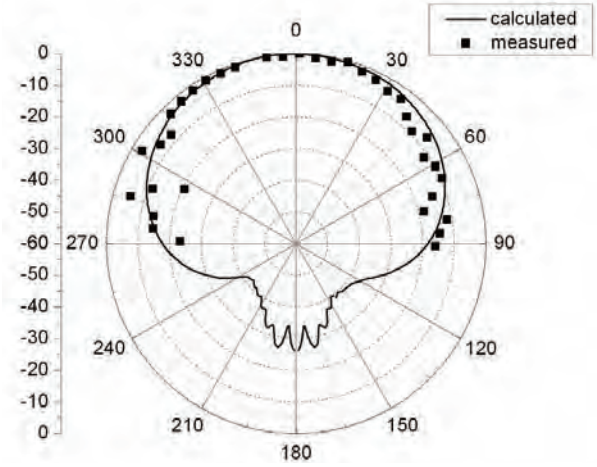

(b)

Fig. 4. Normalized radiation pattern of two waveguide - fed aperture arrays on a spherical surface – MODEL I:
a) H - plane;
b) E – plane; ($\alpha_1=0^0$, $\beta_{11}=0^0$, $\alpha_2=18^0$, $\beta_{21}=90^0$) [8].

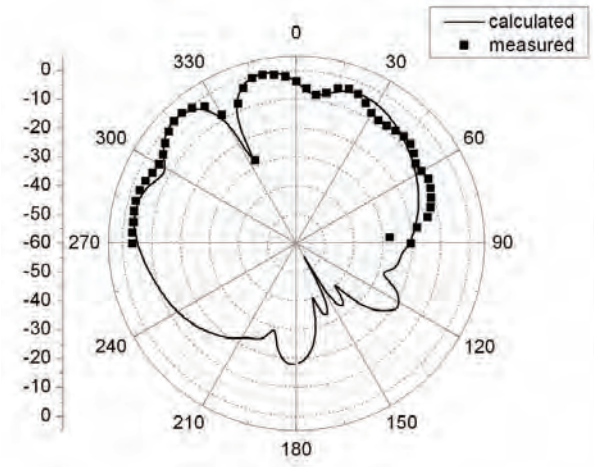

(a)

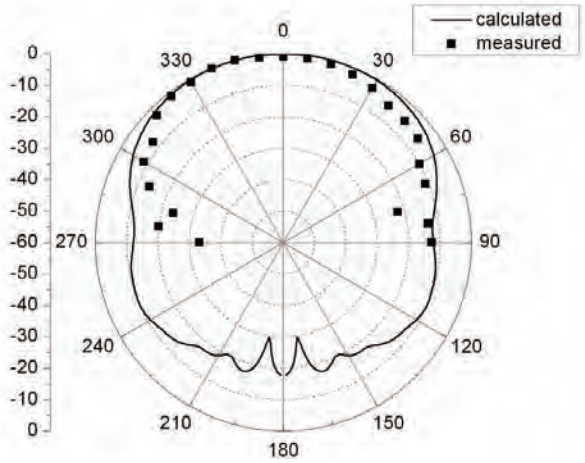

(b)

Fig. 5. Normalized differential radiation pattern of two waveguide - fed aperture arrays on a spherical surface – MODEL II:
a) E –plane;
b) H - plane. ($\alpha_1=0^0$, $\beta_{11}=0^0$, $\alpha_2=56^0$, $\beta_{21}=180^0$) [7].

As expected, the main beam peak of the radiation pattern is on a half value of the second waveguide position angle $\theta_{np}=\frac{\alpha_2}{2}=9^\circ$ (or precisely -9^0).

Theoretical and measured free-space normalized radiation patterns of two waveguide antennas (MODEL I) on the spherical surface are shown in Fig. 4.

Figures 5., 6. and 7. show free-space normalized radiation patterns of antenna arrays (MODEL II) with a different number of elements (waveguides) which are activated (two, three and six waveguides, respectively).

As can be seen in Figure 5., the notch-peak of the differential radiation pattern is on a half value of the second waveguide position angle $\theta_{np}=\frac{\alpha_2}{2}=28^\circ$ (or precisely -28^0).

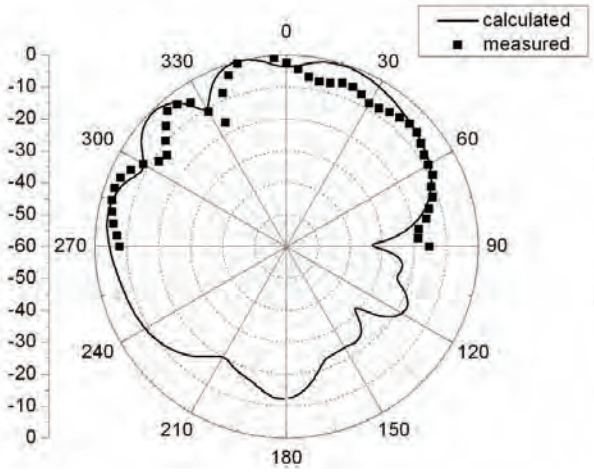

(a)

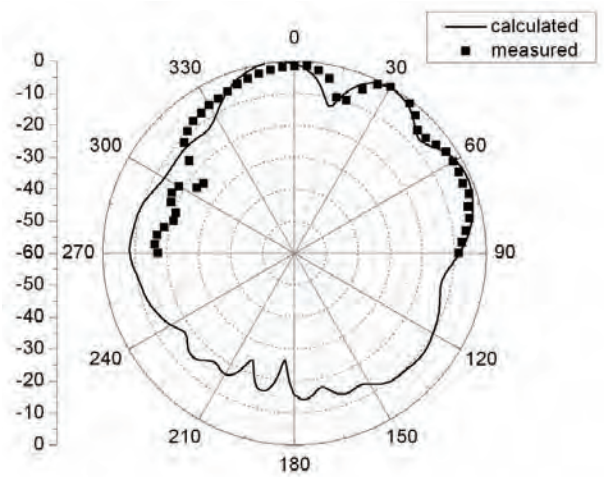

(b)

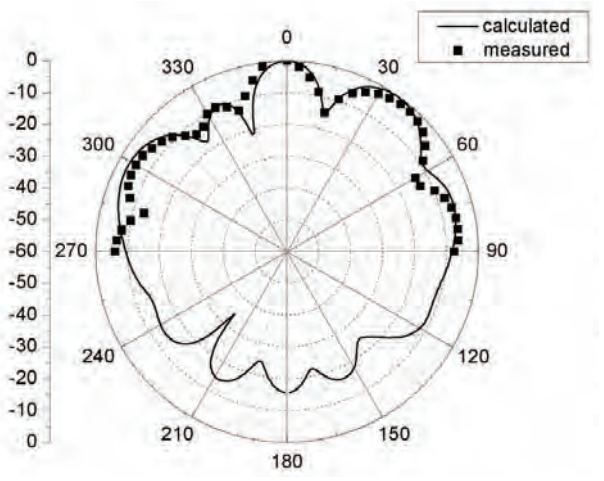

(a)

Fig. 6. Radiation pattern of a spherical array consisting of three waveguide-fed aperture arrays on a spherical surface – MODEL II:
a) E - plane;
b) H – plane(excited waveguides on positions: $\alpha_1=0^0$, $\beta_{11}=0^0$, $\alpha_2=56^0$, $\beta_{21}=108^0$, $\beta_{22}=180^0$) [8].

Moreover, we achieve a very good agreement between the theoretical and the measured normalized radiation pattern regarding the main beam and side lobes. What has to be mentioned here is that the grating lobe amplitude is lower than the main beam but not enough. The reason is that the antenna elements are not phased such that the pattern produced by an array has maximum along the direction θ_{max} and φ_{max} and the inter-element distances are not optimal.

Prior to the statistical analysis the measurement interval ($-90 \leq \theta \leq 90$) is dissected into two intervals:

1. **main beam (notch-peak) interval**: maximum radiation direction angle (main beam) $\pm 30^0$ (Figures 4., 6., and 7.) and notch peak angle $\pm 30^0$ (Fig. 5.);
2. **other interval**: outside of the main beam interval.

Tables 1, 2, 3 and 4 show descriptive statistics for the average difference of theoretical and measured results. As can be seen, the maximal absolute average difference in the main beam intervals ranges between 0.65 and 1.99 dB, except for Fig.6a where the difference is 3.81 dB. The average difference in other intervals ranges between 2.0 and 7.0 dB.

The results indicate that the amount of errors (measurement errors, method errors and laboratory model errors), defined as the absolute difference of theoretical and measured results and analyzed by statistic parameters, does not have important effects on radiation of these spherical arrays. Furthermore, the measured results suggest that the developed theoretical model and computer program are performed very well.

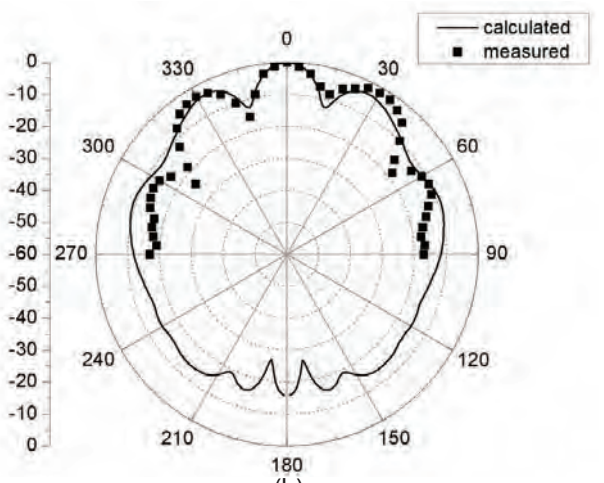

(b)

Fig. 7. Radiation pattern of six waveguide-fed aperture arrays on a spherical surface – MODEL II:
a) E - plane;
b) H – plane ($\alpha_1=0^0$, $\beta_{11}=0^0$, $\alpha_2=56^0$, $\beta_{21}=36^0$, $\beta_{22}=108^0$, $\beta_{23}=180^0$, $\beta_{24}=252^0$, $\beta_{25}=324^0$).

5. CONCLUSION

In this paper, we have shown the radiation pattern of two spherical antenna arrays. Analysis of the arrays was made with the developed moment method program.

The results obtained from the theoretical investigation are verified by comparison with measured results.

The errors in the measured results appear due to experimental model errors, diffraction from the edges of the semi-spherical surface and reflections inside the measurement room which is not a well-defined anechoic chamber.

Descriptive statistic parameters confirmed a very good agreement between theoretical and measured normalized radiation patterns.

REFERENCES

[1] P.-S. Kildal and J. Sanford, "Analysis of conformal antennas by using spectral domain techniques for curved structures," *Proceedings of COST 245 - ESA workshop on active antennas*, Noordwijk, pp. 17-26, 1996.

[2] Z. Sipus, P.-S. Kildal, R. Leijon and M. Johansson, "An algorithm for calculating Green's functions for planar, circular cylindrical and spherical multilayer substrates," *Applied Computational Electromagnetics Society Journal*, Vol. 13, pp. 243-254,1998.

[3] D. L. Sengupta, T. M. Smith and R. W. Larson, "Radiation Characteristics of Spherical Array of Circularly Polarized Elements", *IEEE Trans. on Antennas and Propagation*, Vol. 16, pp. 2-7, Jan. 1968.

[4] D. L. Sengupta, J.E.Ferris and T. M. Smith, "Experimental Study of a Spherical Array of Circularly Polarized Elements", Proceedings of the *IEEE* , pp. 2048-2051, Nov. 1968.

[5] Z. Sipus, S. Rupcic, M. Lanne and L. Josefsson, "Analysis of Circular and Spherical Array of Waveguide Elements Covered with Radome", *Proceedings of IEEE International Symposium on Antennas and Propagation, Boston,* USA, pp. II 350-353, 2001.

[6] N. Burum, S. Rupcic and Z. Sipus, "Theoretical and Experimental Study of Spherical Arrays", *IEEE MELECON 2004, Dubrovnik,* Croatia, pp. II 503-506, 2004.

[7] S. Rupcic and V. Mandric, "Effect of Experimental Model Errors on Radiation Pattern of a Spherical Aperture Antennas Array", ELMAR 2008, Zadar, Croatia, pp. 240 - 245, 2008.

[8] S. Rupcic,, "Circular Waveguide Antenna Arrays on Spherical Structures", PhD Thesis, *University of Zagreb, Faculty of Electrical Engineering and Computing,* Zagreb, 2009.

Tab. 1. Descriptive statistics for the absolute difference of theoretical and measured results of a spherical array consisting of two waveguide-fed apertures – MODEL I.

Fig.4a)					
INTERVALS (deg)	**MEAN (dB)**	**STD (dB)**	**MEDIAN (dB)**	**P25 (dB)**	**P75 (dB)**
-90≤θ≤+90	5.14954	4.95528	4.11	1.34	7.39
-39≤θ≤+27	1.99663	2.36085	1.04	0.35	3.24
-90≤θ<-39 and +27<θ≤+90	7.0687	5.16822	6.16	3	8.79
Fig.4b)					
-90≤θ≤+90	2.29205	2.55099	1.41	0.51	3.18
-30≤θ≤+30	0.65217	0.45205	0.46	0.47	1.055
-90≤θ<-30 and +30<θ≤+90	3.0792	2.77085	2.14	1.96	4.34

Tab. 2. Descriptive statistics for the absolute difference of theoretical and measured results of a spherical array consisting of two waveguide-fed apertures – MODEL II.

Fig.5a)					
INTERVALS (deg)	**MEAN (dB)**	**STD (dB)**	**MEDIAN (dB)**	**P25 (dB)**	**P75 (dB)**
-90≤θ≤+90	1.81386	2.02812	0.97	0.4	2.27
-58≤θ≤+2	1.37337	2.49723	0.525	0.21	0.82
-90≤θ<-58 and +2<θ≤+90	2.02742	1.76143	1.55	0.82	3.11
Fig.5b)					
-90≤θ≤+90	4.16662	5.05019	2.97	0.91	4.47
-30≤θ≤+30	1.07933	0.94081	0.91	0.597	1.24
-90≤θ<-30 and +30<θ≤+90	5.90322	5.60351	4.08	1.7	6.7058

Tab. 3. Descriptive statistics for the absolute difference of theoretical and measured results of a spherical array consisting of three waveguide-fed apertures – MODEL II.

Fig.6a)					
INTERVALS (deg)	**MEAN (dB)**	**STD (dB)**	**MEDIAN (dB)**	**P25 (dB)**	**P75 (dB)**
-90≤θ≤+90	3.41388	3.48686	2.14	1.02	5.3
-58≤θ≤+2	3.81063	3.43463	2.12	1.1	5.94
-90≤θ<-58 and +2<θ≤+90	3.22152	3.54834	2.44	0.76	4.99
Fig.6b)					
-90≤θ≤+90	1.71	3.26349	1.71	0.99	5
-2≤θ≤+58	1.53875	1.60089	1.115	0.5	1.5
-90≤θ<-2 and +58<θ≤+90	4.16548	3.52857	2.33	1.42	6.88

Tab. 4. Descriptive statistics for the absolute difference of theoretical and measured results of a spherical array consisting of six waveguide-fed apertures – MODEL II.

Fig.7a)					
INTERVALS (deg)	**MEAN (dB)**	**STD (dB)**	**MEDIAN (dB)**	**P25 (dB)**	**P75 (dB)**
-90≤θ≤+90	1.86159	1.77157	1.65	0.77	2.17
-30≤θ≤+30	1.50029	1.79233	1.03	0.77	1.65
-90≤θ<-30 and +30<θ≤+90	2.05353	1.75838	1.785	0.76	2.5
Fig.7b)					
-90≤θ≤+90	3.29388	2.79373	2.92	0.88	5.1
-30≤θ≤+30	1.25118	1.30449	0.88	0.05	2.3
-90≤θ<-30 and +30<θ≤+90	4.37906	2.77541	4.365	1.63	6.65

WSN Implementation in the Greenhouse Environment Using Mobile Measuring Station

Simon János
Subotica Tech, Department of Informatics
simon@vts.su.ac.rs

Goran Martinović
Faculty of Electrical Engineering, J.J. Strossmayer University of Osijek
goran.martinovic@etfos.hr

István Matijevics
University of Szeged, Department of Informatics
mistvan@inf.u-szeged.hu

Abstract *– Continuous advancements in wireless technology and miniaturization have made the deployment of sensor networks to monitor various aspects of the environment increasingly flexible. The function of a greenhouse is to create the optimal growing conditions for the full life of the plants. Using autonomous measuring systems helps to monitor all the necessary parameters for creating the optimal environment in the greenhouse. The robot equipped with sensors is capable of driving to the end and back along crop rows inside the greenhouse. This paper deals with the implementation of mobile measuring station in greenhouse environment. It introduces a wireless sensor network that was used for the purpose of measuring and controlling the greenhouse application.*

Keywords *– WSN, Sun SPOT, embedded system, PIC, mobile robot, greenhouse*

1. INTRODUCTION

Mobile robotics is a young field of research. Its roots include many engineering and science disciplines, from mechanical, electrical and electronics engineering to computer, cognitive and social sciences. The Board Of Education is a complete, low-cost development platform equipped with the needed sensors for humidity, temperature, light, etc. As shown in Figure 1, the Boe-Bot is a great tool with which to get started with robotics.

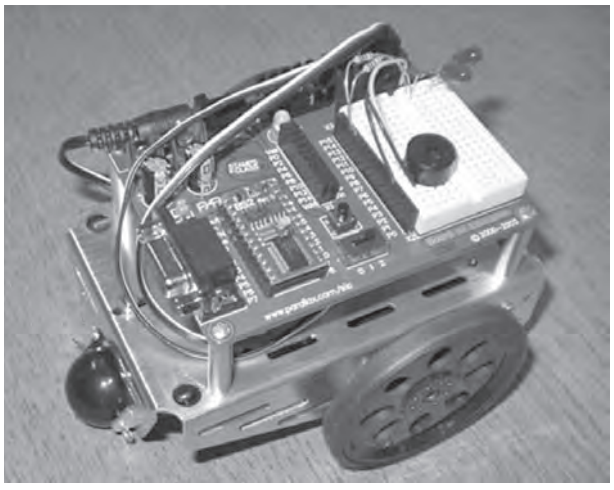

Fig. 1. Assembled Boe-Bot

The SunSPOT WSN module makes it possible for the Boe-Bot robot's BASIC Stamp 2 microcontroller brain to communicate wirelessly with a web based user interface running on a nearby PC. The BASIC Stamp microcontroller runs a small PBASIC program that controls the Boe-Bot robot's servos and optionally monitors sensors while it communicates wirelessly with the web server.

2. CONTROL SCHEME FOR MOBILE ROBOTS

A mobile robot needs locomotion mechanisms that enable it to move throughout its known or unknown environment. But there are a large variety of possible ways to move, and so the selection of a robot's approach to locomotion is an important aspect of mobile robot design. Figure 2, presents the control scheme for mobile robot systems. In the laboratory, there are research robots that can walk, jump, run, slide, skate, swim, fly, and, of course, roll. Any of these activities has its own control algorithm [16].

Locomotion is the complement of manipulation. In manipulation, the robot arm is fixed but moves objects in the workspace by imparting force to them. In locomotion, the environment is fixed and the robot moves by imparting force to the environment. In both cases, the scientific basis is the study of actuators that gen-

erate interaction forces, and mechanisms that implement desired kinematical and dynamic properties. The wheel has been by far the most popular mechanism in mobile robotics and in man-made vehicles in general. It can achieve very good efficiencies, and does so with a relatively simple mechanical implementation. In Figure 3, the kinematics of the mobile robot is depicted. In addition, balance is not usually a research problem in wheeled robot designs, because wheeled robots are almost always designed so that all wheels are in ground contact at all times [15].

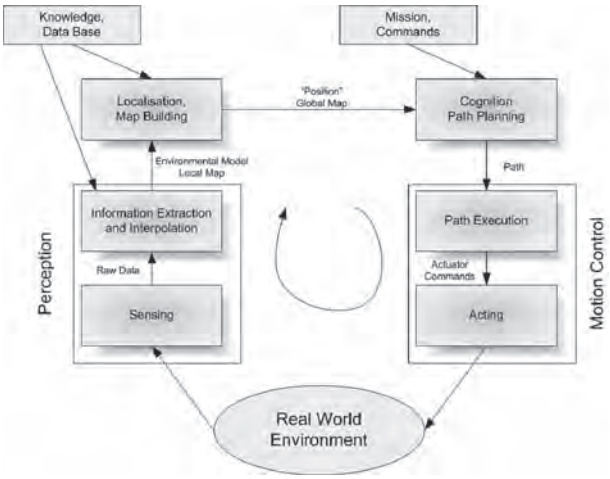

Fig. 2. Reference control scheme for mobile robot systems

Thus, three wheels are sufficient to guarantee stable balance, although, as we shall see below, two-wheeled robots can also be stable [12]. When more than three wheels are used, a suspension system is required to allow all wheels to maintain ground contact when the robot encounters uneven terrain. Motion control might not be an easy task for this kind of systems. However, it has been studied by various research groups, and some adequate solutions for motion control of a mobile robot system are available [16].

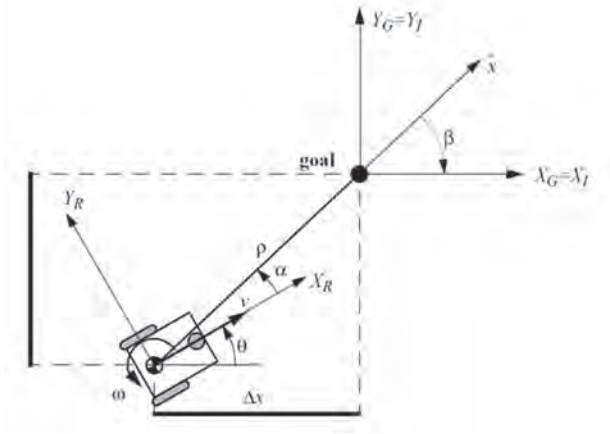

Fig. 3. Robot kinematics and its frames of interests

3. WSN AND EVENT-BASED SYSTEM FOR GREENHOUSE CLIMATE CONTROL

A wireless sensor network (WSN) is a computer network consisting of spatially distributed autonomous devices using sensors to cooperatively monitor physical or environmental conditions, such as temperature, sound, vibration, pressure, motion or pollutants, at different locations [1]. The development of wireless sensor networks was originally motivated by military applications such as battlefield surveillance. Figure 4, presents the sensor node architecture. However, wireless sensor networks are now used in many civilian application areas, including environment and habitat monitoring, healthcare applications, home automation, and traffic control.

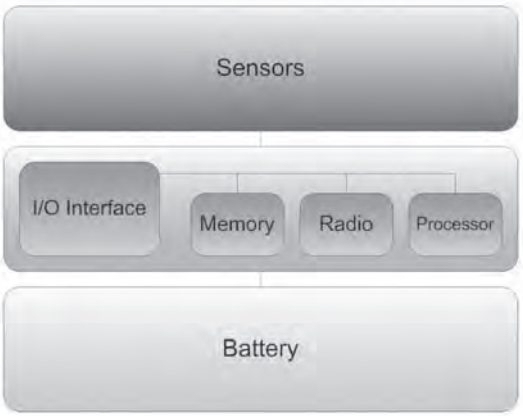

Fig. 4. Sensor Node Architecture

In addition to one or more sensors, each node in a sensor network is typically equipped with a radio transceiver or other wireless communications device, a small microcontroller, and an energy source, usually a battery. Figure 5 shows the typical wireless sensor network.

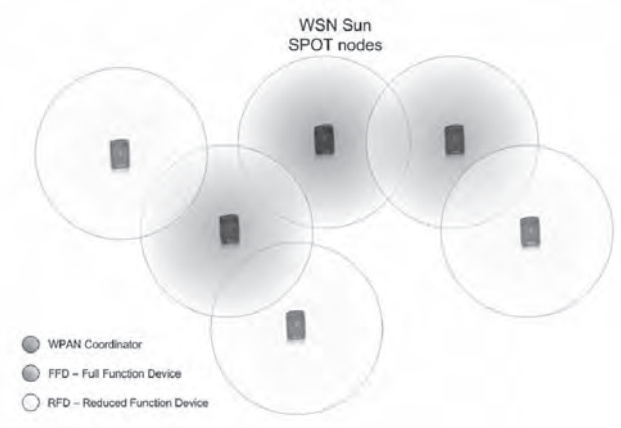

Fig. 5. Typical wireless sensor network (WSN)

The size a single sensor node can vary from shoebox-sized nodes down to devices the size of grain of dust [2]. The cost of sensor nodes is similarly variable, ranging

from hundreds of dollars to a few cents, depending on the size of the sensor network and the complexity required of individual sensor nodes. Size and cost constraints on sensor nodes result in corresponding constraints on resources such as energy, memory, computational speed and bandwidth. In computer science, wireless sensor networks are an active research area with numerous workshops and conferences arranged each year [4].

As commented above, this paper is devoted to analyzing diurnal and nocturnal temperature control with natural ventilation and heating systems, and humidity control as a secondary control objective. Under diurnal conditions, the controlled variable is the inside temperature and the control signal is the vent opening. The use of natural ventilation produces an exchange between the inside and outside air, usually provoking a decrease in the inside temperature of the greenhouse. The controller must calculate the necessary vent opening to reach the desired setpoint. The commonest controller used is a gain scheduling PI scheme where the controller parameters are changed based on some disturbances: outside temperature and wind speed. In the case of nocturnal temperature control, forced-air heaters are used to increase the inside temperature and an on/off control with dead/zone was selected as heating controller.

Nowadays, commercial systems present more flexibility in the implementation of control algorithms and sampling techniques, especially WSN, where each node of the network can be programmed with a different sampling algorithm or local control algorithm with the main goal of optimizing the overall performance.

4. SOLUTION

Building and programming a robot is a combination of mechanics, electronics, and problem solving. What you're about to learn while doing the activities and projects in this text will be relevant to "real world" applications that use robotic control, the only difference being the size and sophistication. Robotics has come a long way, especially for mobile robots. In the past, mobile robots were controlled by heavy, large, and expensive computer systems that could not be carried and had to be linked via cable or wireless devices. As shown in Figure 8, the mobile measuring station is navigating inside the greenhouse. Today, however, we can build small mobile robots with numerous actuators and sensors that are controlled by inexpensive, small, and light embedded computer systems that are carried on-board the robot.

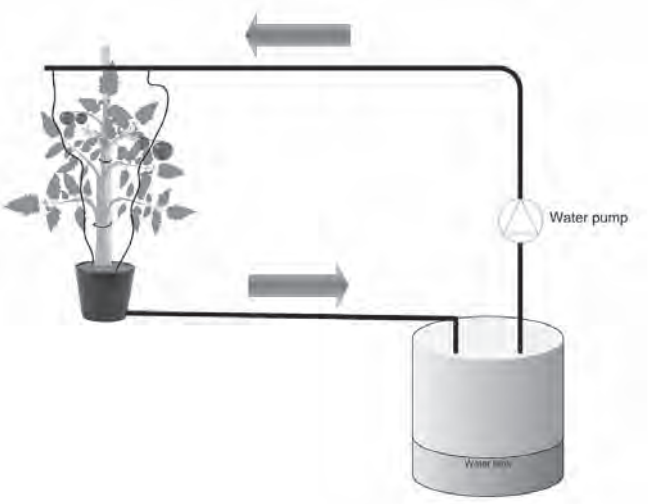

Fig. 6. Humidity control

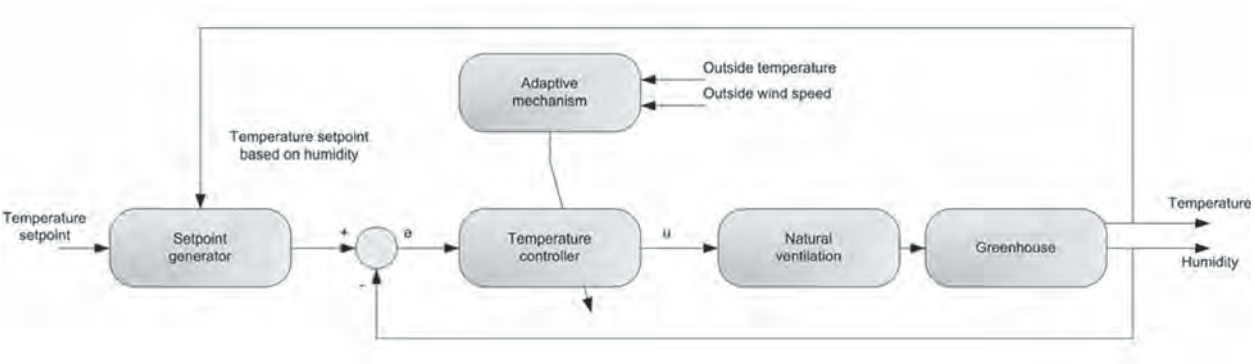

Fig. 7. Temperature controller

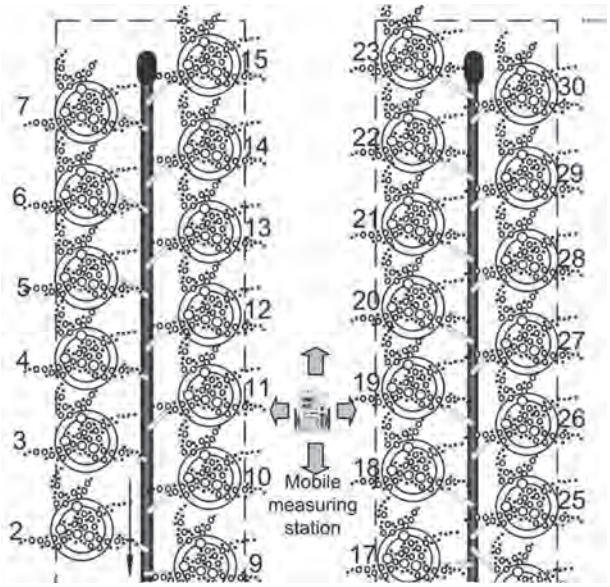

Fig. 8. Greenhouse top view with the mobile measuring station

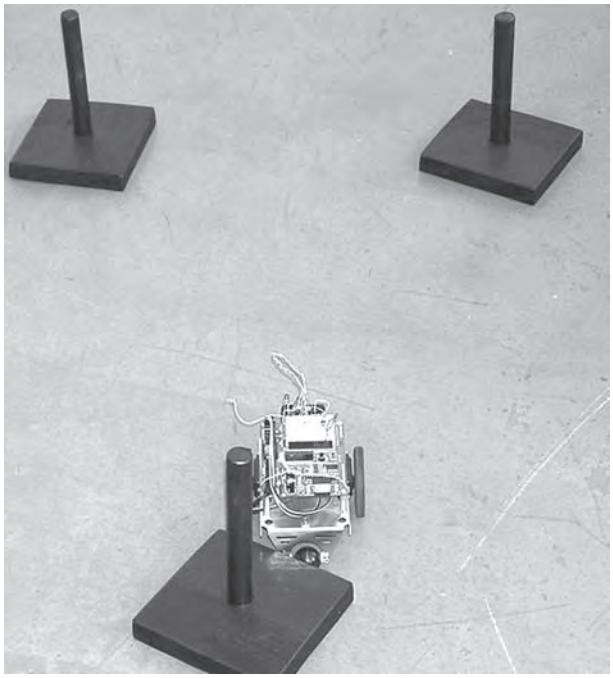

Fig. 10. Boe-bot with SunSPOT mounted

The mechanical principles, example program listings, and circuits you will use are very similar to, and sometimes the same as, industrial applications developed by engineers. In this project we have used SunSPOT-s to achieve remote control over a Boe-Bot. For this project we have used 2 SunSPOT-s from the kit (free range and base station module) as depicted in Figure 9. SunSPOT's wireless protocol is Zigbee based protocol [6].

The Hardware basically centers around Sun SPOT and DC Motors controlled by Basic Stamp. The Sun SPOT base station will send data to Sun SPOT on the mobile measuring station which will drive the Basic Stamp controller to DC IO pins [7]. The microcontroller will drive the Motors which will run the measuring station. Figure 10 shows the testing phase of the mobile measuring station.

5. EXPERIMENTAL RESULTS

The applications for WSNs are many and varied. They are used in commercial and industrial applications to monitor data that would be difficult or expensive to monitor using wired sensors. They could be deployed in wilderness areas, where they would remain for many years (monitoring some environmental variable) without the need to recharge/replace their power supplies. They could form a perimeter about a property and monitor the progression of intruders (passing information from one node to the next). There are a many uses for WSNs [8].

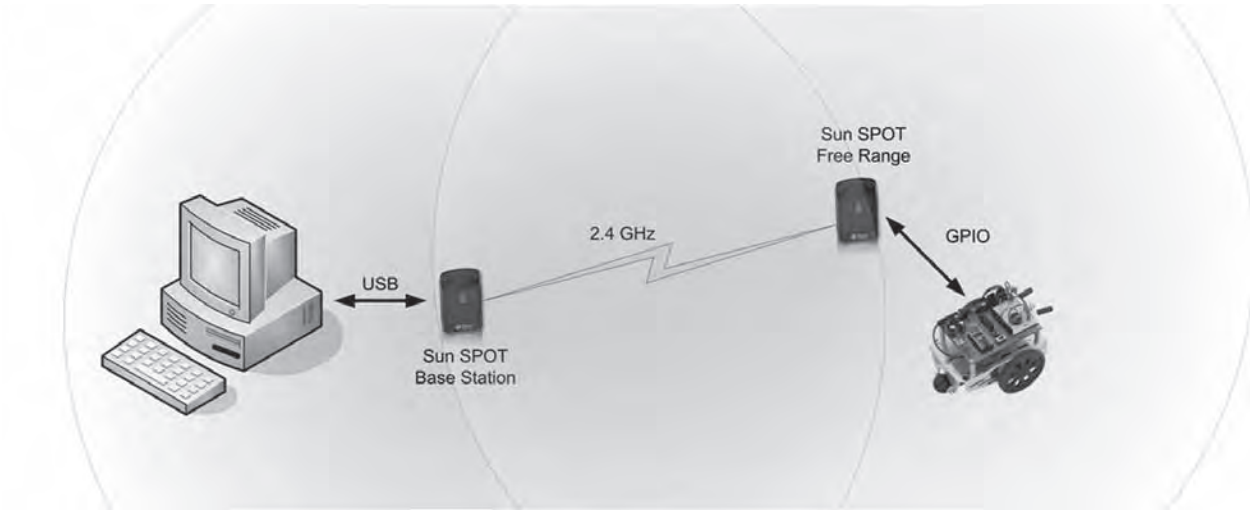

Fig. 9. Connection of the system

Fig. 11. Crops in greenhouse

Typical applications of WSNs include monitoring, tracking, and controlling. Some of the specific applications are habitat monitoring, object tracking, nuclear reactor controlling, fire detection, traffic monitoring, etc. In a typical application, a WSN is scattered in a region where it is meant to collect data through its sensor node. Figure 12 shows the complete control system of the greenhouse. The WSN-based controller has allowed a considerable decrease in the number of changes in the control action and made possible a study of the compromise between quantity of transmission and control performance.

The limit of the level crossing sampling has presented a great influence on the event based control performance where, for the greenhouse climate control problem, the system has provided promising results.

Fig. 11. Capsicum

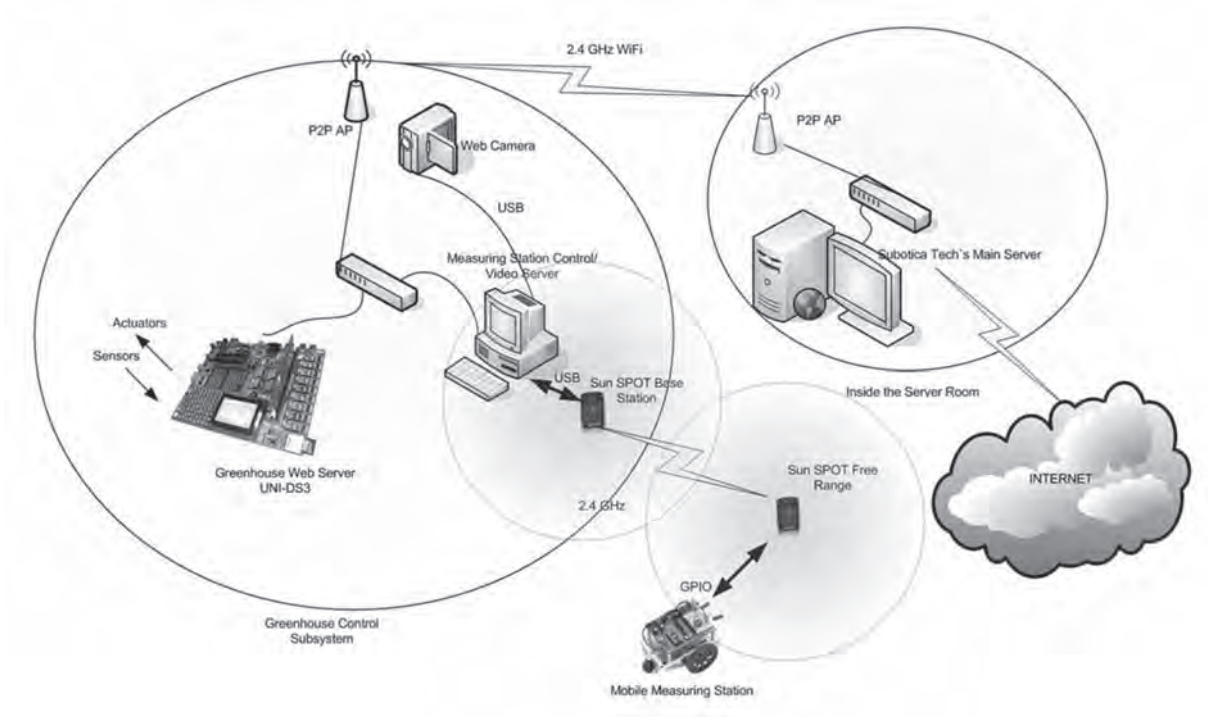

Fig. 12. Greenhouse control system

Motion control of mobile robots is a very important research field today, because mobile robots are a very interesting subject both in scientific research and practical applications. In this paper the object of the remote control is the Boe-Bot. The vehicle has two driving wheels and the angular velocities of the two wheels are independently controlled [9]. When the vehicle is moving towards the target and the sensors detect an obstacle, an avoiding strategy is necessary. The host system connects to the mobile robot with the SunSPOT module. A remote control program has been implemented as shown in Figure 14.

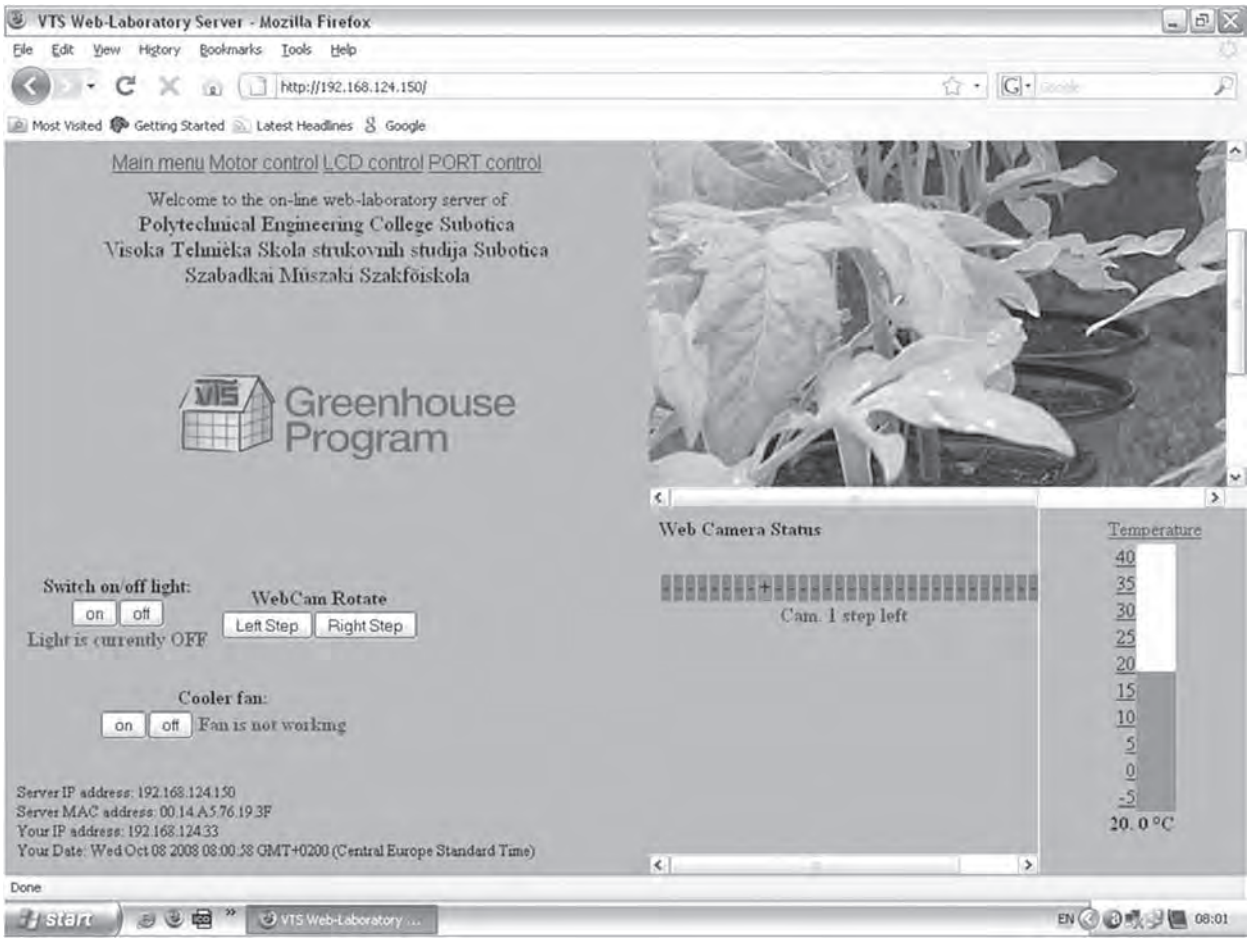

Fig. 14. Screenshot of the system

The code snippet below gives an example of testing the communication devices in broadcast mode as we can see in Figure 15. It is written in Java and runs on SunSPOT modules. Each SPOT is assigned its own address and can broadcast or unicast to the other SPOTs. This code is implemented for testing purposes only.

The Sun SPOT is a Java programmable embedded device designed for flexibility. The basic unit includes accelerometer, temperature and light sensors, radio transmitter, eight multicolored LEDs, 2 push-button control switches, 5 digital I/O pins, 6 analog inputs, 4 digital outputs, and a rechargeable battery. Java imple-

```
    protected void startApp() throws MIDletStateChangeException {
        System.out.println(„Broadcast Counter MIDlet”);
        //showColor(color);
        //switches[0].addISwitchListener(this);
        //switches[1].addISwitchListener(this);
        try {
            tx = (RadiogramConnection)Connector.open(„radiogram://broadcast:123”);
            xdg = (Radiogram)tx.newDatagram(20); //transmitting the radiogram
            RadiogramConnection rx = (RadiogramConnection)Connector.
open(„radiogram://:123”);
            Radiogram rdg = (Radiogram)rx.newDatagram(20);
            //outs[0].setHigh();
            while (true) {
                try {
                    rx.receive(rdg);
```

```
                    int cmd = rdg.readInt();
                    //int newCount = rdg.readInt();
                  //int newColor = rdg.readInt();
                    /*if (cmd == CHANGE_COLOR) {
                        System.out.println(„Received packet from „ + rdg.getAddress());
                        //showColor(newColor);
                    } else {
                        //showCount(newCount, newColor);
                    }*/
                    switch (cmd){
                        case 0: outs[demo.H0].setLow(); outs[demo.H1].setLow(); leds[0].
setRGB(200, 0, 0); leds[0].setOn(); leds[1].setOff();leds[2].setOff();leds[3].setOff();
break;
                        case 4: outs[demo.H0].setHigh(); outs[demo.H1].setLow(); leds[1].
setRGB(200, 0, 0); leds[1].setOn(); leds[0].setOff();leds[2].setOff();leds[3].setOff();
break;
                        case 3: outs[demo.H0].setLow(); outs[demo.H1].setHigh(); leds[2].
setRGB(200, 0, 0); leds[2].setOn(); leds[1].setOff();leds[0].setOff();leds[3].setOff();
break;
                        case 1: outs[demo.H0].setHigh(); outs[demo.H1].setHigh(); leds[3].
setRGB(200, 0, 0); leds[3].setOn(); leds[1].setOff();leds[2].setOff();leds[0].setOff();
break;
//setting up the diagnostic leds
                        default: leds[4].setRGB(200, 0, 0); leds[4].setOn(); break;
                    }
                } catch (IOException ex) {
                    System.out.println(„Error receiving packet: „ + ex);
                    ex.printStackTrace(); // Error detection
                }
            }
        } catch (IOException ex) {
            System.out.println(„Error opening connections: „ + ex);
            ex.printStackTrace(); // Error detection
        }
    }
```

Fig. 15. Sending broadcast packets via WSN from base station

mentation and programming the Sun SPOT is surprisingly easy. Experimental testing has demonstrated the validity of our approach.

6. COMPARISON OF THE FRUIT PRODUCTION

Tomatoes are a warm season vegetable crop. They grow best under conditions of high light and warm temperatures. Low light in a fall or winter greenhouse, when it is less than 15% of summer light levels, greatly reduces fruit yield when heating costs are highest. For this reason, it is difficult to recommend that a greenhouse operator should grow and harvest fruit from December 15 to February 15. Based on few years of experience, tomato production is most successful in the spring. Excellent light, moderate heating costs and good prices annually demonstrate this is the best time for greenhouse tomato production. Tomato plants grow best when the night temperature is maintained at 16 - 18 °C. Temperatures below 16 °C will prevent normal pollination and fruit development. In warm or hot outdoor conditions, tomato greenhouses must be ventilated to keep temperatures below 35 °C. High temperatures not only affect the leaves and fruit, but increased soil temperatures also reduce root growth. Table 1 gives an overview of effectiveness of the control system.

Table 1. The average total weight and number of fruit harvested

Tested plants	Average weight of fruit (with WSN control)	Average weight of fruit (without WSN control)	Average number of fruit per plant (with WSN control)	Average number of fruit per plant (without WSN control)
Tomato	210 g	180 g	17	11
Capsicum	135 g	110 g	15	12
Cucumber	70 g	60 g	13	10

Success in greenhouse plants depends completely on fruit yield. Yields of 20 – 25 % gain per plant are very good for annual costs.

7. CONCLUSION

The system and its implementation have been successful; however there are still possibilities for further development. The first cycle of plant development has just passed, and it has provided numerous valuable data. For the next cycle better conditions will be provided, with more experienced staff. With further developments the application of professional industrial electronics will also have to be taken into consideration, which would significantly decrease possible problems.

ACKNOWLEDGEMENTS

This research was partially supported by the TAMOP-4.2.2/08/2008-0008 program of the Hungarian National Development Agency.

REFERENCES

[1] Sun Microsystems Inc., "Sun™ Small Programmable Object Technology (Sun SPOT)" Owner's Manual Release 3.0, 2007

[2] Sun Microsystems Inc., "Sun Spot Developer's Guide", 2005

[3] Sun Microsystems Inc., "Demo Sensor Board Library", 2005

[4] S. Scaglia, "The Embedded Internet", 2008

[5] J. Gosling, "The Java™ Language Specification" Third Edition, 2005

[6] I. Matijevics, J. Simon, „Advantages of Remote Greenhouse Laboratory for Distant Monitoring", Proceedings of the Conference ICoSTAF 2008, pp 1-5, Szeged, Hungary, 2008

[7] J. Simon, I. Matijevics, "Distant Monitoring And Control For Greenhouse Systems Via Internet", Zbornik radova konferencije Yuinfo 2009, pp. 1-3, Kopaonik, Srbija, 2009

[8] I. Matijevics, J. Simon, "Comparison of various wireless sensor networks and their implementation", Proceedings of the Conference SIP 2009, pp 1-3, Pécs, Hungary, 2009

[9] A. Pawlowski, J. Luis Guzman, F. Rodríguez, M. Berenguel, J. Sánchez and S. Dormido "Simulation of Greenhouse Climate Monitoring and Control with Wireless Sensor Network and Event-Based Control" Proceedings of the Conference ,2009

[10] L. Gonda, C. Cugnasca, "A proposal of greenhouse control using wireless sensor networks" In Proceedings of 4thWorld Congress Conference on Computers in Agriculture and Natural Resources, Orlando, Florida, USA, 2006

[11] X. Feng, T. Yu-Chu, S. Yanjun, S. Youxian "Wireless Sensor/Actuator Network Design for Mobile Control Applications. Sensors", Proceedings of the Conference, 2007

[12] Roland Siegwart and Illah R., "Introduction to Autonomous Mobile Robots", Nourbakhsh, 2004

[13] J. Vasu, L. Shahram, "Comprehensive Study of Routing Management in Wireless Sensor Networks- Part-1", 2008

[14] J. Simon, G. Martinović, "Web Based Distant Monitoring and Control for Greenhouse Systems Using the Sun SPOT Modules", Proceedings of the Conference SISY 2009, pp. 1-5, Subotica, Serbia, 2009

[15] Gy. Mester, "Wireless Sensor-based Control of Mobile Robot Motion", Proceeding of the IEEE SISY 2009, pp 81-84, Subotica, Serbia 2009

[16] Gy. Mester, "Intelligent Wheeled Mobile Robot Navigation", Proceedings of the Conference Európai Kihívások V, pp. 1-5, SZTE, Szeged, Hungary, 2009

[17] P. Kucsera, „Sensors For Mobile Robot Systems" , Academic and Applied Research in Military Science, Volume 5, Issue 4, p.645-658,Hungary, 2006

[18] P. Kucsera, "Industrial Component-based Sample Mobile Robot System" , Acta Polytechnica Hungarica, Volume 4 Issue 4 Number 4, Hungary, 2006

Power Loss Minimizing Control of Cascaded Multilevel Inverter with Efficient Hybrid Carrier Based Space Vector Modulation

Chinnathambi Govindaraju
Department of Electrical and Electronics Engineering
Government College of Engineering, Salem, Anna University-Chennai, India
govindcraju@rediffmail.com

Kaliaperumal Baskaran
Department of Computer Science and Engineering
Government College of Technology, Coimbatore, India
baski_101@yahoo.com

Abstract *– This paper presents a power loss minimization technique for a cascaded multilevel inverter using hybrid carrier based space vector modulation. The proposal in this paper combines the features of carrier based space vector modulation and the fundamental frequency modulation strategy. The main characteristic of this modulation is the reduction of switching loss and energy efficiency improvements with better harmonic performance. In order to implement this hybrid modulation scheme and deliver the hybrid PWM pulses to the appropriate switches, a TMS320F2407 digital signal processor (DSP) and a Complex Programmable Logic Device (CPLD) are used. The inverter offers lower harmonic distortion and operates with equal thermal stress among the power devices. Using simulation and experimental results, the superior performance of a new PWM method is shown.*

Keywords *– carrier-based space vector modulation, cascaded multilevel inverter, digital signal processor, power loss analysis, total harmonic distortion*

1. INTRODUCTION

Multilevel pulse width modulation inversion is an effective solution for increasing power and reducing harmonics of AC waveforms. A multilevel inverter has four main advantages over the conventional bipolar inverter. First, the voltage stress on each switch is decreased due to series connection of the switches. Therefore, the rated voltage and consequently the total power of the inverter could be safely increased. Second, the rate of change of voltage is decreased due to a lower voltage swing of each switching cycle. Third, harmonic distortion is reduced due to more output levels. Fourth, lower acoustic noise and electromagnetic interference (EMI) is obtained [1]. Various multilevel converter structures are reported in the literature, and the cascaded multilevel converter appears to be superior to other multilevel converters in application at high power rating due to its modular nature of modulation, control and protection requirements of each full bridge inverter [2]. The power circuit for a five-level cascaded inverter topology shown in Fig.1 is used to examine the proposed PWM technique.

Modulation control of any type of a multilevel inverter is quite challenging, and much of the reported research is based on somewhat heuristic investigations. Switching losses in high power converters represent an issue and any switching transitions that can be eliminated without compromising the harmonic content of the final waveform are considered advantages [3]. Most of the modulation methods developed for multilevel inverters is based on multiple-carrier arrangements with pulse width modulation (PWM). The carriers can be arranged with vertical shifts (phase disposition, phase opposition disposition, and alternative phase opposition disposition PWM), or with horizontal displacements (phase-shifted PWM) [4].

Space-vector modulation is also extended for the multilevel inverter operation [5]. These high frequency methods produce high frequency stepped voltage waveforms that are easily filtered by the load and, therefore, they present very good reference tracking and low current harmonic distortion. However, this is also the reason for high switching losses, which is undesirable in high-power applications. As a result, low-frequency methods have been presented.

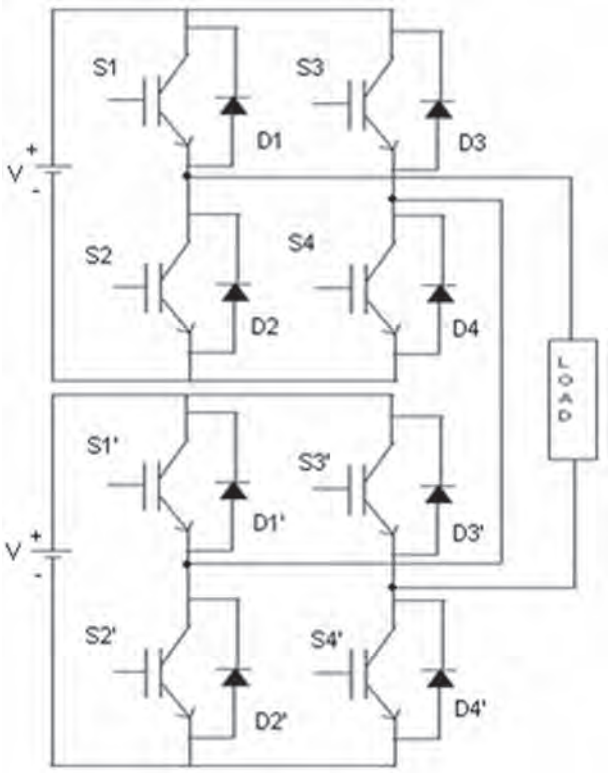

Fig. 1. Schematic diagram of the inverter topology (one phase leg) used to verify the proposed five-level hybrid carrier based space vector modulation.

Multilevel space-vector control reduces switching losses but has a variable magnitude error for the fundamental component [6]. Selective harmonic elimination (SHE) is also extended for multilevel inverters [7]. Nevertheless, offline calculations are necessary, making dynamic operation and closed loop implementation not straightforward. In addition, selective harmonic elimination becomes unfeasible with the increase of the number of levels, since it is directly related to the number of angles, hence equations that need to be solved. Carrier based space vector modulation was developed first for bipolar PWM and then extended to a multilevel inverter [8]. Wenxi Yao proposed that these techniques are harmonically equivalent, with the best spectral performance being achieved when the nearest three space vector states are selected with the middle two vectors centered in each half carrier switching interval [9]. This strategy is known as carrier based space vector modulation (CBSVM).

In this paper, a new modulation technique is presented to addresses reduction of switching losses in a cascaded multilevel inverter, with an improved harmonic performance. This modulation is a combination of fundamental frequency modulation and carrier based space vector modulation. The paper is organized in the following way. Section 2 describes carrier based space vector modulation suitable for the cascaded multilevel inverter. The proposed hybrid carrier based space vector modulation is discussed in detail in Section 3. Section 4 presents power loss minimizing control and an analysis of a cascaded multilevel inverter with this proposed modulation. Section 5 illustrates simulation and experimental results of different operating points including the discussion on the results. Finally, some conclusions are presented in Section 6.

2. REVIEW OF CARRIER BASED SPACE VECTOR MODULATION

Space vector modulation (SVM) offers low harmonic distortion for three phase inverters by placing the most unwanted harmonics power on triplen harmonics. SVM is intrinsically a non-carrier based digital technique for generating switching angles. However, due to a constant sampling rate used in SVM, the equivalent carrier based techniques have been developed. CBSVM is appropriate for inverters with more than five levels, where the computational overhead for conventional SVM is exceeding due to many output states. CBSVM is derived from the addition of a common offset voltage to the three phase references it will center the active space-vectors in the switching period, and hence match carrier modulation to get optimized space vector modulation [10].

Generally, carrier based PWM of a multilevel inverter can only select four switching states at most, but SVM can select more. Selection of switching states has more freedom in multilevel SVM than in multilevel carrier based PWM. In order to solve that problem, multilevel SVM can also be decomposed into several two level carrier based PWM cells. This method effectively increases the number of switching in a multilevel SVM scheme greater than in a conventional PWM scheme, but the additional switching is mainly added in the area the modulated wave is steep, where the output wave may be distorted most seriously, so it is more effective to improve the output voltage by using a multilevel SVM scheme than by increasing frequency of carrier waves directly. Furthermore, more freedom of switching selection of multilevel SVM is also propitious to power balance of H-bridge cells in a cascaded multilevel inverter. The optimal switching sequence can be achieved by using a proper offset voltage.

The appropriate offset voltage for v_{off}' multilevel operation can be expressed by the following equations so that the comparison between multicarriers and references generates the optimized switching sequence.

$$V_{off} = -\frac{\max(V_a,V_b,V_c)+\min(V_a,V_b,V_c)}{2}\sqrt{a^2+b^2} \qquad (1)$$

$$V_k' = (V_k + V_{off} + V_{dc}) \bmod \left(\frac{2V_{dc}}{N-1}\right),\ k = a,b,c \qquad (2)$$

$$V_{off}' = \frac{V_{dc}}{N-1} - \frac{\max(V_a',V_b',V_c')+\min(V_a',V_b',V_c')}{2} \qquad (3)$$

where v_{dc} is 1 p.u. Addition of a proper offset voltage to phase voltage references v_a, v_b, or v_c generates modified references, and CBSVM signals for each phase leg switches can be generated throughout the comparison between the respective modified references and phase disposition carriers.

3. PROPOSED HYBRID CARRIER BASED SPACE VECTOR MODULATION

The proposed hybrid carrier based space vector modulation is a combination of fundamental frequency PWM and carrier based space vector modulation. The basic principle behind the proposed scheme, the four power devices in each full bridge of a cascaded inverter are operated at two different frequencies, two being commutated at the fundamental frequency of the output, while the other two power devices are pulse width modulated at CBSVM. This arrangement causes the problem of differential switching losses among the switches. This technique is optimized with a sequential signal and the resultant hybrid CBSVM pulses overcome this problem. In this modulation strategy, three base PWM signals are required for each converter in a cascaded multilevel inverter. A sequential signal (A) is a square signal with 50% duty ratio and it has half of the fundamental frequency. This signal makes every power switch operating at CBSVM and low frequency PWM sequentially.

Fundamental frequency PWM (B) is a square wave signal synchronized with the modulation waveform, and it is defined as B=1 during the positive half cycle of the modulation signal, and as B=0 during the negative half cycle of the modulation signal. CBSVM is based on the comparison of a modified sinusoidal reference signal ($v_k + v_{off}\ v_{off}'$) with each carrier to determine the voltage level that the inverter should switch to. In this carrier based N level PWM operation consists of N-1 different carriers, where all carriers are in phase. A sequential switching signal and low frequency PWM signals are the same for all full bridge converter cells. The base PWM signals (A, B, C and D) for a hybrid PWM controller are shown in Fig. 2.

A hybrid PWM controller is implemented using a simple combinational logic, and hence, it can be processed very quickly. The functions of the combinational logic for a five-level hybrid PWM are expressed as

$$S1 = A\,B\,C + \overline{A}\,B \qquad S1' = A\,B\,D + \overline{A}\,B$$
$$S2 = \overline{A}\,B\,C + \overline{A}\,\overline{B} \qquad S2' = \overline{A}\,B\,D + \overline{A}\,\overline{B}$$
and
$$S3 = \overline{A}\,\overline{B}\,C + A\,\overline{B} \qquad S3' = \overline{A}\,\overline{B}\,D + A\,\overline{B}$$
$$S4 = \overline{A}\,B\,C + A\,B \qquad S4' = \overline{A}\,B\,D + A\,B$$

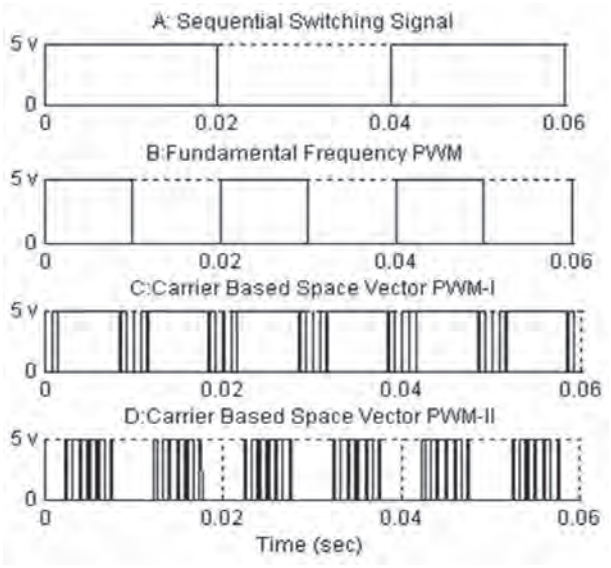

Fig. 2. Base PWM signals for five-level hybrid carrier-based space vector modulation

In Fig. 3, it is shown that each gate signal is composed of both low frequency PWM and CBSVM signals. If sequential switching signal A=1, S1 and S2 in converter 1 and S1′ and S2′ in converter 2 are operated with CBSVM while S3 and S4 in converter 1 and S3′, S4′in converter 2 are operated at fundamental frequency. If sequential switching signal A=0, S1 and S2 in converter 1 and S1′ and S2′ in converter 2 are operated at fundamental frequency while S3 and S4 in converter 1 and S3′, S4′in converter 2 are operated with CBSVM. Since A is a sequential signal, the average switching frequency amongst the four switches and power loss are equalized. Thermal stress of power switches in each inverter bridge is also inherently equalized with this modulation.

For completeness, the generalized formulation that suits for an N-level inverter and for any number of switching transitions is presented. The proposed algorithm for an N-level inverter is as follows:

1. Obtain the number of inverter cells K=N-1/2.
2. Modify the peak amplitude of phase reference voltages v_a, v_b and $v_c$based on modulation index $M=A_m/K\,A_c$, where Am is the amplitude of a modulation signal and Ac is the amplitude of a carrier signal.
3. Identify the instantaneous values of three phase reference voltages v_a, v_b, and v_c and determine the values of v_{off} and v_{off}'.
4. A modified sinusoidal reference signal is obtained by $v_k' = v_k + v_{off} + v_{off}'$.
5. Comparison of a modified sinusoidal modulating signal with each phase disposition carrier signal separately to generate a K number of carrier based space vector modulation signals.

6) A common sequential signal and fundamental frequency PWM signals for each phase are obtained in synchronization with a modulating signal.

7) An independent hybrid controller (combinational logic circuit) is used to mix low frequency PWM and the corresponding carrier based SVM for each inverter cell.

$$Sx1 = A\ B\ X + \overline{A}\ B;\ Sx2 = \overline{A}\ B\ X + \overline{A}\ \overline{B};$$
$$Sx3 = \overline{A}\ \overline{B}\ X + A\ \overline{B};\ Sx4 = \overline{A}\ B\ X + A\ B$$

8) Similarly, hybrid PWM pulses are developed for all cells in any level cascaded inverter. Totally 4K gate pulses per phase are developed to operate an N-level cascaded multilevel inverter.

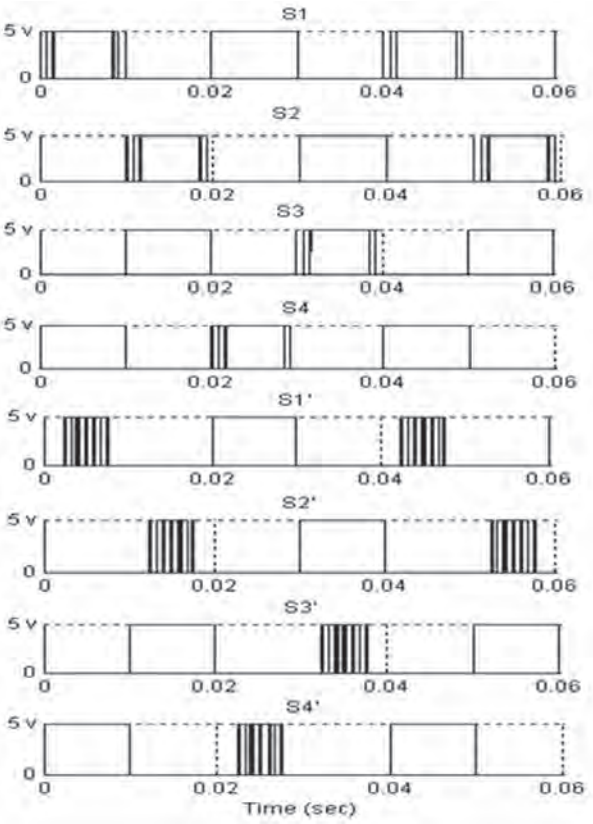

Fig.3. Hybrid carrier based space vector modulation signals for a five-level cascaded multilevel inverter

4. POWER LOSS MINIMIZING CONTROL AND ANALYSIS

Power loss optimization is achieved in this paper by the proposed modulation technique in which

1. Proper offset voltage v_{off} and v_{off}' are developed and added to the phase reference voltages to get an optimized CBSVM.
2. CBSVM is combined with fundamental frequency PWM using a hybrid PWM control algorithm, so that the number of commutations of semiconductors per unit time in the operation of multilevel inverters is reduced.
3. An optimized sequential signal is added to hybrid PWM signals to balance the power loss among the power devices. Each power device present in the cascaded inverter operates with fundamental frequency PWM (two commutations per cycle) and CBSVM (the number of commutations proportional to switching frequency) for one fundamental period. So the number of semiconductor switching is half of the conventional space vector modulation. This technique is also designed to get the optimum number of switching events based on the modulation index and the phase angle between voltage and current fundamentals.

The losses in power converters can be classified as: conduction loss, switching loss, snubber loss, and off-state loss. Since the leakage current during the off state of the device is negligibly small, the power loss during the off state can be neglected. Snubber losses can be important in some kinds of power devices, such as gate turn-off thyristors [11]. Thus, only conduction and switching losses are considered in this paper. New high power devices can switch faster. Since switching losses are directly related to the switching frequency, these losses are usually greatest in PWM power converters.

MATLAB-Simulink model of a five-level inverter has been developed to study the power loss. The carrier frequency f_s is 2 kHz and each converter cell is connected to a 200 V DC supply. The IGBTs selected are FF150R12KT3G, in which their maximum ratings are a forward current of 150 A and a direct voltage of 600 V. The semiconductor power losses can be estimated from the curves ($V_{sat}(\theta)$ x $I_1(\theta)$) and ($E(\theta)$ x $I_1(\theta)$), presented in the datasheet of each device, where : V_{sat} is the on-state saturation voltage ($V_{ce}(\theta)$ for the IGBT and $V_F(\theta)$ for the diode); $E(\theta)$represent energy losses in one commutation ($E_{on}(\theta)$ if it is a turn-on commutation, $E_{off}(\theta)$ if it is a turn-off commutation and $E_{rec}(\theta)$ if it is a diode reverse recovery process). These curves are used in a Matlab script developed to determine the power losses. Mathematical models are found using points extracted from datasheets of each semiconductor device. Mathematical models obtained for the IGBT module FF150R12KT3G are given by

$$V_F = 1.2\, e^{0.002\, I_1(\theta)} - 0.7258\, e^{-0.0475\, I_1(\theta)}$$

$$V_{ce} = 1.15\, e^{0.0026\, I_1(\theta)} - 0.6654\, e^{-0.044\, I_1(\theta)}$$

$$E_{rec} = 0.01806\, e^{-0.000412\, I_1(\theta)} - 0.0157\, e^{-0.00736\, I_1(\theta)}$$

$$E_{on} = 0.0051\, e^{0.0064\, I_1(\theta)} - 0.0037\, e^{-0.00811\, I_1(\theta)}$$

$$E_{off} = 0.0643\, e^{0.00121\, I_1(\theta)} - 0.0647\, e^{-0.00107\, I_1(\theta)}$$

$$I_1(\theta) = M \bullet I_{max} \sin(\theta - \phi)$$

where $I_1(\theta)$is the load current, M is the modulation index and φ is the load displacement angle.

Conduction and switching power losses are calculated based on mathematical models for each semiconductor device of the inverter. The sum of all results is computed to obtain the total power losses. The total power losses are the sum of conduction and switching losses.

$$P_{Total} = P_{cond} + P_{sw}$$

Switching losses are generated during the turn-on and turn-off switching processes of power devices. In such processes, the voltages and currents can take significant values simultaneously. Therefore, their instantaneous power can reach high values. Fortunately, these processes only last for short periods, although they are repeated several times within a second. For this reason, they are directly related to the switching frequency. Switching losses are obtained by identifying every turn-on and turn-off instant during one reference period.

$$P_{sw} = \frac{1}{T} \sum (E_{on} + E_{off} + E_{rec})$$

Conduction power losses are those that occur while a semiconductor device is conducting current. Conduction losses of transistors are obtained from linearization of the static characteristics of power switches. The calculation of conduction power losses are given by

$$P_{cond\_IGBT} = \frac{1}{2\pi} \int_0^{2\pi} V_{ce}(\theta) \bullet I_1(\theta) \bullet V_{cmd}(\theta)\, d\theta$$

$$P_{cond\_D} = \frac{1}{2\pi} \int_0^{2\pi} V_F(\theta) \bullet I_1(\theta) \bullet V_{cmd}(\theta)\, d\theta$$

$$P_{cond} = P_{cond\_IGBT} + P_{cond\_D}$$

where $V_{cmd}(\theta)$ is the PWM signal of the IGBT

For a full range of a modulation index and the relative angle of the output currents, Fig.4 (c) shows the ratio of total power losses for a five-level inverter with the proposed modulation strategy versus the conventional CBSVM technique. Note that the surface is always below one, which means that power losses are significantly smaller for the proposed method. The mean value of the loss ratio is found to be approximately 0.73, which implies the power loss reduction of about 27%. The best case is produced for a unity power factor and a modulation index of one. In a practical high power system, switching losses are higher than conduction losses. Therefore, saving switching losses becomes important for improvement of the system efficiency.

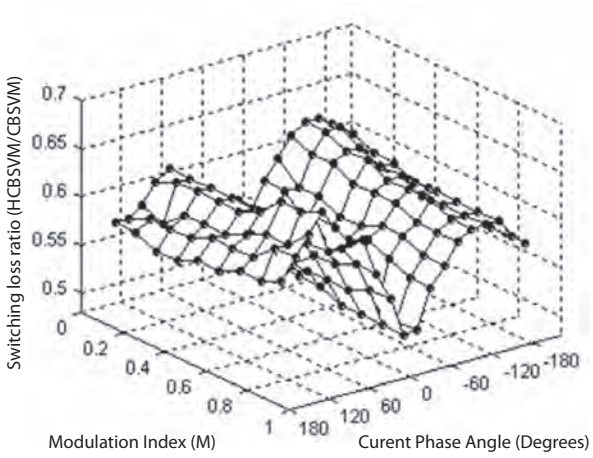

(a)

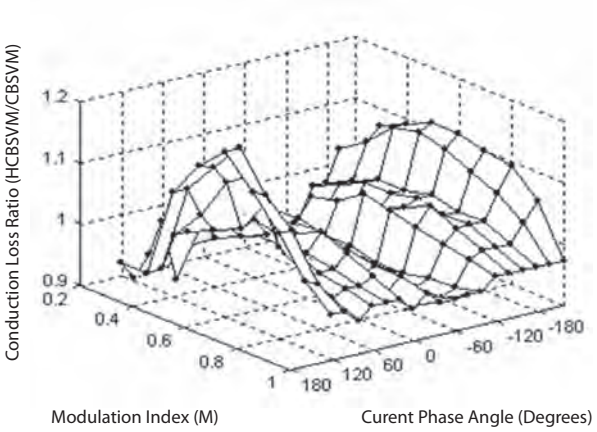

(b)

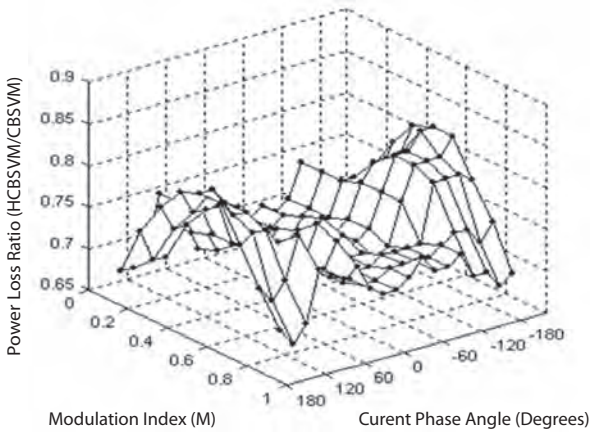

(c)

Fig.4. Ratio of the losses of hybrid carrier based space vector modulation and conventional CBSVM fed five-level cascaded inverters.
(a) Switching Losses.
(b) Conduction Losses.
(c) Total Power Loss.

5. RESULTS AND DISCUSSION

5.1. SIMULATION RESULTS

In order to verify that the proposed modulation can be practically implemented in a cascaded inverter, simulations were performed by using MATLAB/Simulink. It also helps to confirm the PWM switching strategy which can be implemented in a digital signal processor (DSP) and a complex programmable logic device (CPLD). The performance index, namely total harmonic distortion (THD), is chosen for quantification of the proposed hybrid CBSVM. The total harmonic distortion of a signal is the ratio of the sum of the powers of all harmonic frequencies above the fundamental frequency to the power of the fundamental frequency. The THD is calculated using (4) and plotted in Fig.5 and it is taken into account up to the 50th order of harmonics. The low pass filter and the nature of the highly inductive load will take care of the higher order of harmonics. It is obviously found that the proposed PWM offers a lower THD compared to the conventional one, thus the superiority. Furthermore, it is also noticed that the higher value of the modulation index (M) the lower the value of THD and for the increased frequency ratio.

$$THD = \frac{\sqrt{\sum_{n=2}^{50} V_n^2}}{V_1} \times 100 \qquad (4)$$

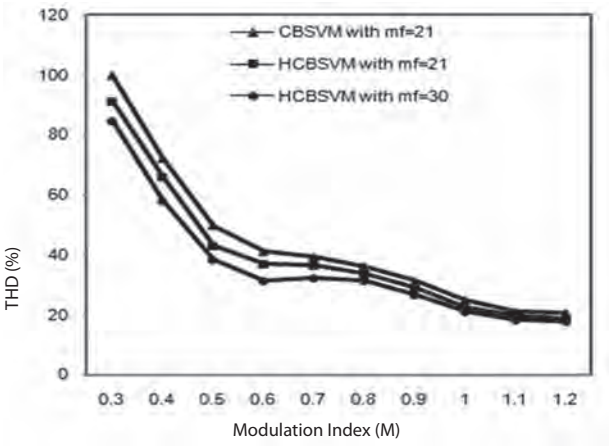

Fig. 5. THD comparision of a five-level cascaded inverter with the proposed modulation

The inverter is operated with the proposed modulation in a linear modulation range and the corresponding voltage waveform with the FFT analysis is shown in Fig.7. It can be seen that all the lower order harmonics are absent and the fundamental is controlled at the predefined value. It is interesting to note that the next significant harmonic will be the 35th for a frequency ratio of 21. The significant harmonics are 35, 39, 41, and 45, which are of high frequency, with the rms values under 11% of the fundamental term. The compared conventional PWM operation is shown in Fig.6, the FFT spectrum of the proposed inverter output voltage gives superiority.

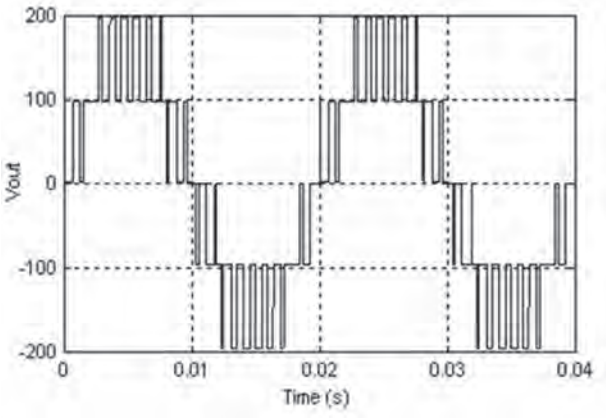

(a)

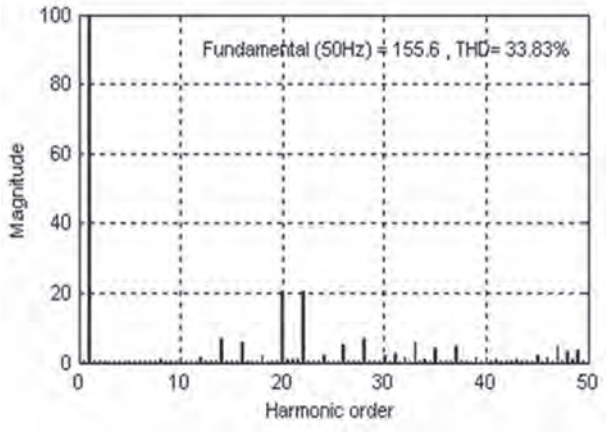

(b)

Fig. 6. Simulation results of conventional CBSVM operation in a linear modulation region (M=0.8, fo =50 Hz, fc =1050 Hz)
(a) Output phase voltage waveform.
(b) Spectrum of the output voltage waveform.

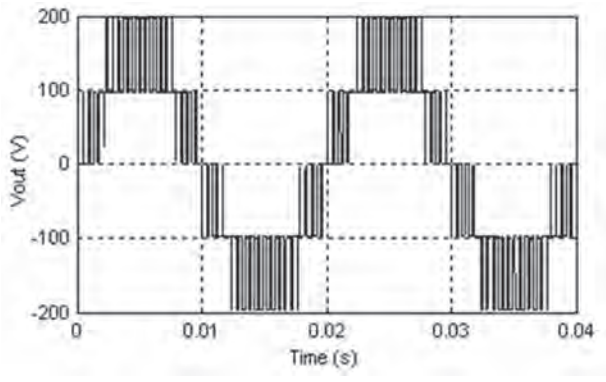

(a)

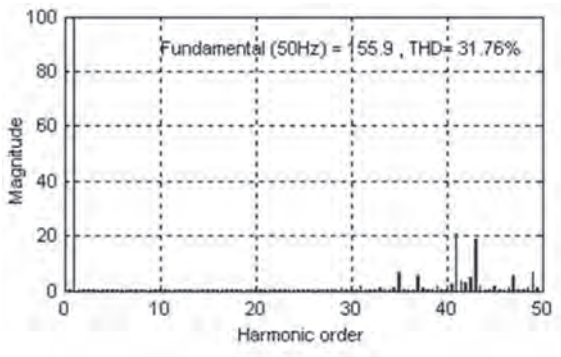

(b)

Fig. 7. Simulation results of hybrid CBSVM operation in a linear modulation region (M=0.8, fo =50 Hz, fc =1050 Hz)
(a) Output phase voltage waveform.
(b) Spectrum of the output voltage waveform.

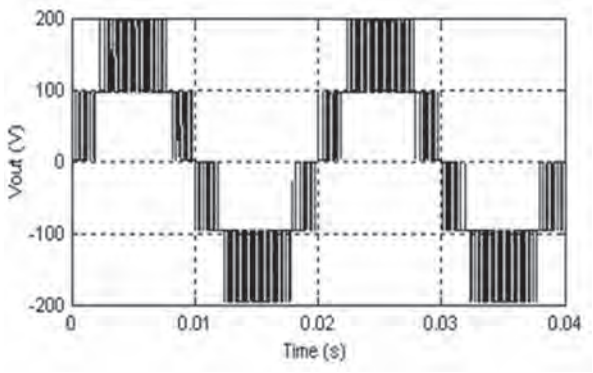

(a)

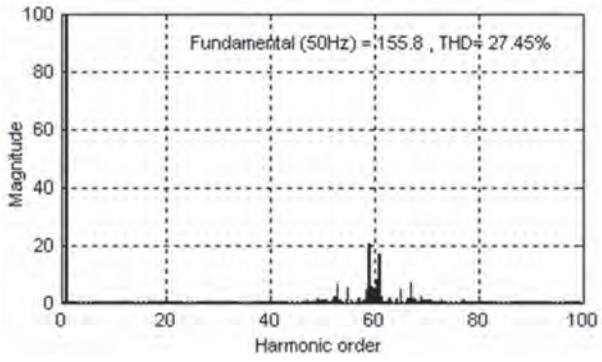

(b)

Fig. 8. Simulation results of hybrid CBSVM operation in a linear modulation region (M=0.8, fo =50 Hz, fc =1500 Hz)
(a) Output phase voltage waveform.
(b) Spectrum of the output voltage waveform.

5.2. EXPERIMENTAL RESULTS

A functional block diagram of hybrid modulation controller implementation for a five-level cascaded inverter is shown in Fig.9. The inverter is made with eight insulated gate bipolar transistor (IGBT) switches with internal anti-parallel diodes. Texas instruments TMS320F2407 digital signal processor (DSP) is chosen for base PWM generation as it has dedicated PWM units that utilize high speed counters/timers with accompanying compare registers. The structure of CBSVM is very simple and it requires only a few mathematical operations in order to provide modulation signals. The PWM unit is initialized by defining parameters such as symmetric carrier, switching frequency, PWM polarity, and to modulation signals for compare registers. The appropriate offset components are calculated based on phase voltage references. After adding zero sequence signals to fundamental signals, modulation signals are ready to be loaded into compare registers of a PWM unit. A sequential signal is also generated to operate each IGBT with fundamental frequency PWM and CBSVM sequentially to equalize power losses, heating among the devices.

The proposed hybrid modulation algorithm is implemented using Xilinx CPLD XC95108 IC. A CPLD controller combines fundamental frequency PWM, sequential signal and CBSVM to generate hybrid CBSVM pulses. XC95108 IC is used to develop a control algorithm which is suited for this application that has features of a better response for high frequency input signals, narrow pulse width pulses and no jitter of the delay in the circuit. A switching dead time of 600 ns is introduced in the CPLD hardware. Optically coupled isolators MCT2E are used to provide an electrical isolation between the Xilinx CPLD controller board and the power circuit. Four high voltage high speed IGBT drivers (IR2112) are used to provide proper and conditioned gate signals to power switches.

A digital real time oscilloscope (Tektronix TPS2024) is used to display and capture the output waveforms and with the feature of the fast Fourier transform (FFT), the spectrum of the output voltage is obtained for different operating points as discussed hereafter. Selected experimental results for a five-level inverter were obtained and validated the simulation results.

Specifically, Fig.10 (a) shows the line to a neutral voltage waveform of the proposed five-level CBSVM operation in a standard modulation and the associated spectrum is presented in Fig.10 (b). It is confirmed that the harmonic cancellation up to sidebands around double the carrier frequency is achieved in the voltage waveform and the first significant harmonic is the 17th, as predicted. The over-modulation operation for the proposed method is also experimentally verified and results are presented in Fig.11. As expected, the spectrum shows that a lower order harmonic (5th) is introduced with a lower magnitude in addition to side-band harmonics. This shows that the hybrid PWM modulator is capable of taking the system from a linear mode to an over-modulation mode smoothly.

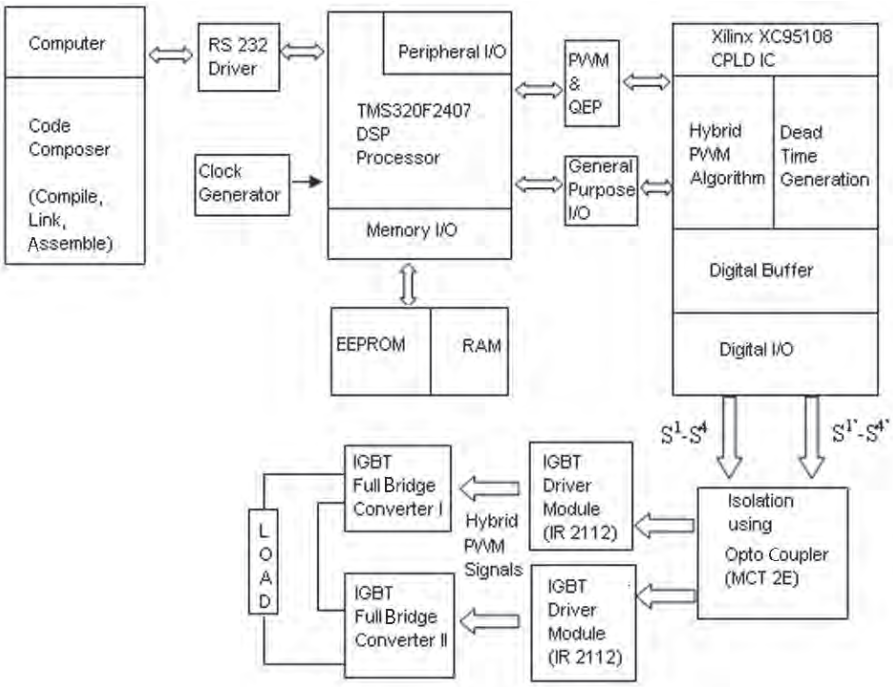

Fig. 9. Functional block diagram of hybrid CBSVM implementation (one phase)

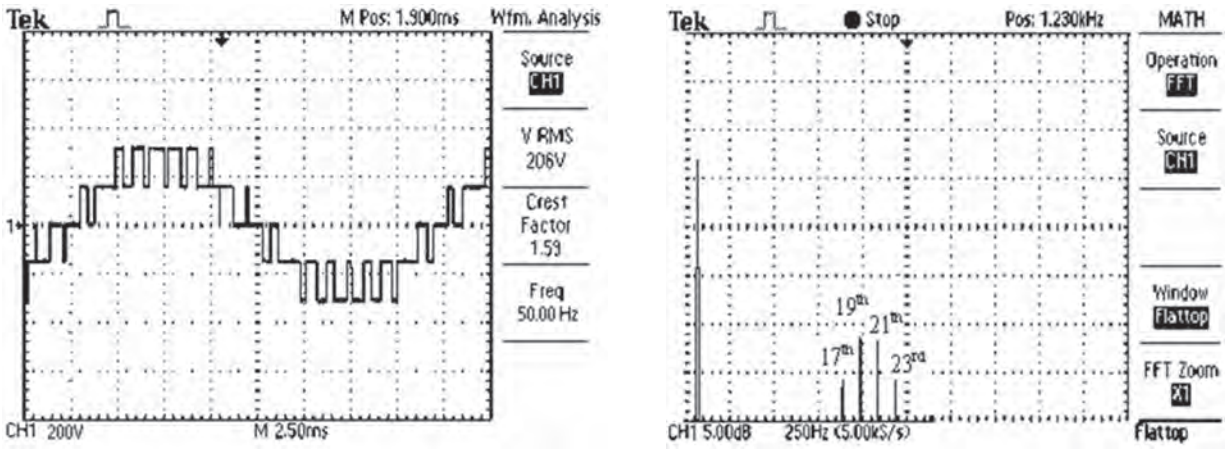

(a) (b)

Fig.10. Experimental results of hybrid CBSVM operation in linear modulation (a) phase voltage waveform. (b) Spectrum of the phase voltage waveform

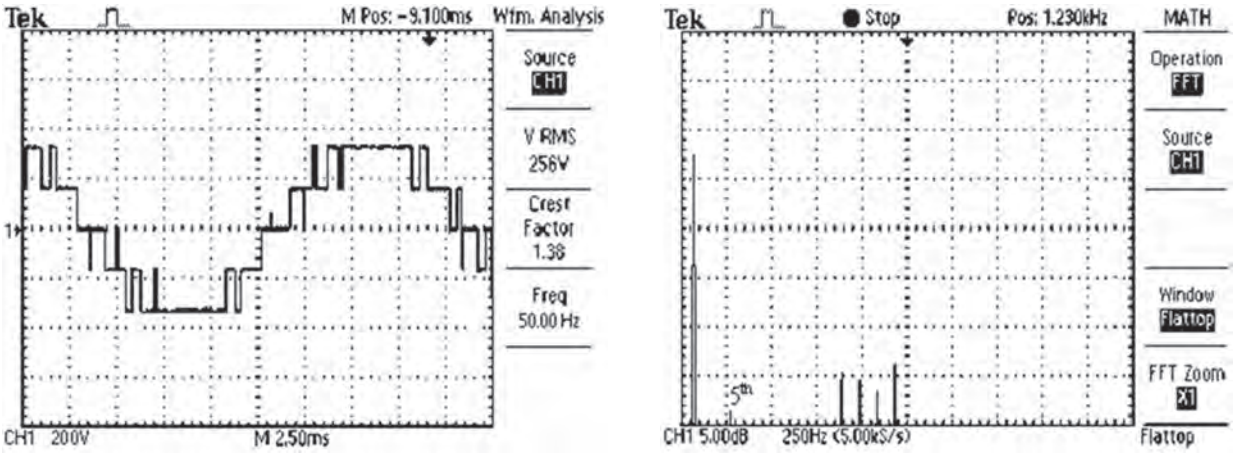

(a) (b)

Fig. 11. Experimental results of the hybrid CBSVM in over-modulation range. (a) Output voltage waveform. (b) Spectrum of the output voltage waveform.

6. CONCLUSION

This paper proposed an energy efficient hybrid carrier based space vector modulation for a cascaded multilevel inverter. The hybrid PWM control algorithm is developed to derive the features of fundamental frequency PWM and carrier based space vector modulation for an inverter operation, with the same physical structure. Compared to conventional CBSVM, a reduced number of commutations of semiconductors per unit time is obtained while achieving the same fundamental voltage tracking and it offers 27% of power loss saving. Better harmonic performance of the proposed PWM strategy compared to its CBSVM in the entire range of the modulation index is shown. The proposed technique can be applied easily to higher level inverters through the generalization process. The presented strategy and its results represent an illustration of the advantages that can be obtained by applying power loss minimizing control to multilevel inverters.

REFERENCES

[1] J. Rodríguez, J. S. Lai, F. Z. Peng, "Multilevel inverters: A survey of topologies, controls and applications", IEEE Trans. Ind. Electron., Vol. 49, No. 4, pp. 724–738, 2002.

[2] D. G. Holmes and B. P. McGrath, "Opportunities for harmonic cancellation with carrier based PWM for two-level and multi-level cascaded inverters", IEEE Trans. Ind. Applicat., Vol. 37, pp. 574–582, 2001.

[3] B. P. McGrath and D. G. Holmes, "Multicarrier PWM strategies for multilevel inverters", IEEE Trans. Ind. Electron., Vol. 49, No. 4, pp. 858–867, 2002.

[4] N. Celanovic and D. Boroyevich , "A fast space-vector modulation algorithm for multilevel three-phase converters", IEEE Trans. Ind. Appl., Vol. 37, No. 2, pp. 637–641, 2001.

[5] J. Chiasson, L.M. Tolbert, K. McKenzie, Z. Du, "A complete solution to the harmonic elimination problem", IEEE Trans. Power Electron., Vol. 19, No. 2, pp. 491–499, 2004.

[6] V.G. Agelidis, A. Balouktsis, I. Balouktsis, C. Cossar, "Multiple sets of solutions for harmonic elimination PWM bipolar waveforms: Analysis and experimental verification", IEEE Trans. Power Electronics, Vol. 21, No. 2, pp. 415–421, 2006.

[7] A. Gupta, A. Khambadkone, "A space vector PWM scheme for multilevel inverters based on two-level space vector PWM", IEEE Trans. Ind. Electron., Vol. 53, No. 5, pp. 1631–1639, 2006.

[8] Y. Lee, D. Kim, and D. Hyun, "Carrier based SVPWM method for multilevel system with reduced HDF," in Proc. IEEE IAS Annu. Meeting, pp. 1996–2003, 2000.

[9] B. P. McGrath, D. G. Holmes, and T. Lipo, "Optimized space vector switching sequences for multilevel inverters," IEEE Trans. Power Electron., Vol. 18, No. 6, pp. 1293–1301, Nov. 2003.

[10] D. G. Holmes, "A general analytical method for determining the theoretical harmonic components of carrier based PWM strategies," In: Proc. IEEE Industry Applications Society (IAS) Ann. Meeting, Vol. 2, pp. 1207–1214, Oct. 1998.

[11] T.J. Kim, D.W. Kang, Y.H. Lee, D.S. Hyun, "The analysis of conduction and switching losses in multilevel inverter system", In: Proc. of the 32nd Power Electronics Specialists Conference and Applications, pp. 1363-1368, 2001.

INTERNATIONAL JOURNAL OF ELECTRICAL AND COMPUTER ENGINEERING SYSTEMS

Published by Faculty of Electrical Engineering, Josip Juraj Strossmayer University of Osijek, Croatia.

About this Journal

The International Journal of Electrical and Computer Engineering Systems publishes original research in the form of full papers, case studies, reviews and surveys. It covers theory and application of electrical and computer engineering, synergy of computer systems and computational methods with electrical and electronic systems, as well as interdisciplinary research.

Topics of interest include, but are not limited to:

- Power systems
- Renewable electricity production
- Power electronics
- Electrical drives
- Industrial electronics
- Communication systems
- Advanced modulation techniques
- RFID devices and systems
- Signal and data processing
- Image processing
- Multimedia systems
- Microelectronics
- Instrumentation and measurement
- Control systems
- Robotics
- Modeling and simulation
- Modern computer architectures
- Computer networks
- Embedded systems
- High-performance computing
- Parallel and distributed computer systems
- Human-computer systems
- Intelligent systems
- Multi-agent and holonic systems
- Real-time systems
- Software engineering
- Internet and web applications and systems
- Applications of computer systems in engineering and related disciplines
- Mathematical models of engineering systems
- Engineering management
- Engineering education

Paper Submission

Authors are invited to submit original, unpublished research papers that are not being considered by another journal or any other publisher. Manuscripts must be submitted in doc, docx, rtf or pdf format, and limited to 30 one-column double-spaced pages. All figures and tables must be cited and placed in the body of the paper. Provide contact information of all authors and designate the corresponding author who should submit the manuscript to www.etfos.hr/ijeces. The corresponding author is responsible for ensuring that the article's publication has been approved by all coauthors and by the institutions of the authors if required. All enquiries concerning the publication of accepted papers should be sent to ijeces@etfos.hr.

The following information should be included in the submission:

- paper title;
- full name of each author;
- full institutional mailing addresses;
- e-mail addresses of each author;
- abstract (should be self-contained and not exceed 150 words). Introduction should have no subheadings;
- manuscript should contain one to five alphabetically ordered keywords;
- all abbreviations used in the manuscript should be explained by first appearance;
- all acknowledgments should be included at the end of the paper:
- authors are responsible for ensuring that the information in each reference is complete and accurate. All references must be numbered consecutively and citations of references in text should be identified using numbers in square brackets. All references should be cited within the text;
- each figure should be integrated in the text and cited in a consecutive order. Upon acceptance of the paper, each figure should be of high quality in one of the following formats: EPS, WMF, BMP and TIFF;
- corrected proofs must be returned to the publisher within 7 days of receipt.

Peer Review

All manuscripts are subject to peer review and must meet academic standards. Submissions will be first considered by an editor-in-chief and if not rejected right away, then they will be reviewed by anonymous reviewers. The submitting author will be asked to provide the names of 5 proposed reviewers including their e-mail addresses. The proposed reviewers should be in the research field of the manuscript. They should not be affiliated to the same institution of the manuscript author(s) and should not have had any collaboration with any of the authors during the last 3 years.

Author Benefits

The corresponding author will be provided with a .pdf file of the article or alternatively one hardcopy of the journal free of charge.

Units of Measurement

Units of measurement should be presented simply and concisely using System International (SI) units.

Bibliographic Information

Commenced in 2010.
ISSN: 1847-6996
e-ISSN: 1847-7003

Published: semiannually

Copyright

Subscription Information

The annual subscription rate is 50€ for individuals, 25€ for students and 150€ for libraries.

Postal Address

International Journal of Electrical and Computer Engineering Systems (**IJECES**)
Faculty of Electrical Engineering
Josip Juraj Strossmayer University of Osijek
Kneza Trpimira 2b
31000 Osijek
Croatia

IJECES Copyright Transfer Form

(Please, read this carefully)

This form is intended for all accepted material submitted to the IJECES journal and must accompany any such material before publication.

TITLE OF ARTICLE (hereinafter referred to as "the Work"):

COMPLETE LIST OF AUTHORS:

The undersigned hereby assigns to the IJECES all rights under copyright that may exist in and to the above Work, and any revised or expanded works submitted to the IJECES by the undersigned based on the Work. The undersigned hereby warrants that the Work is original and that he/she is the author of the complete Work and all incorporated parts of the Work. Otherwise he/she warrants that necessary permissions have been obtained for those parts of works originating from other authors or publishers.

Authors retain all proprietary rights in any process or procedure described in the Work. Authors may reproduce or authorize others to reproduce the Work or derivative works for the author's personal use or for company use, provided that the source and the IJECES copyright notice are indicated, the copies are not used in any way that implies IJECES endorsement of a product or service of any author, and the copies themselves are not offered for sale. In the case of a Work performed under a special government contract or grant, the IJECES recognizes that the government has royalty-free permission to reproduce all or portions of the Work, and to authorize others to do so, for official government purposes only, if the contract/grant so requires. For all uses not covered previously, authors must ask for permission from the IJECES to reproduce or authorize the reproduction of the Work or material extracted from the Work. Although authors are permitted to re-use all or portions of the Work in other works, this excludes granting third-party requests for reprinting, republishing, or other types of re-use. The IJECES must handle all such third-party requests. The IJECES distributes its publication by various means and media. It also abstracts and may translate its publications, and articles contained therein, for inclusion in various collections, databases and other publications. The IJECES publisher requires that the consent of the first-named author be sought as a condition to granting reprint or republication rights to others or for permitting use of a Work for promotion or marketing purposes. If you are employed and prepared the Work on a subject within the scope of your employment, the copyright in the Work belongs to your employer as a work-for-hire. In that case, the IJECES publisher assumes that when you sign this Form, you are authorized to do so by your employer and that your employer has consented to the transfer of copyright, to the representation and warranty of publication rights, and to all other terms and conditions of this Form. If such authorization and consent has not been given to you, an authorized representative of your employer should sign this Form as the Author.

Authors of IJECES journal articles and other material must ensure that their Work meets originality, authorship, author responsibilities and author misconduct requirements. It is the responsibility of the authors, not the IJECES publisher, to determine whether disclosure of their material requires the prior consent of other parties and, if so, to obtain it.

- The undersigned represents that he/she has the authority to make and execute this assignment.
- For jointly authored Works, all joint authors should sign, or one of the authors should sign as authorized agent for the others.
- The undersigned agrees to indemnify and hold harmless the IJECES publisher from any damage or expense that may arise in the event of a breach of any of the warranties set forth above.

_____

Author/Authorized Agent

_____

Date

CONTACT
International Journal of Electrical and Computer Engineering Systems (IJECES)
Faculty of Electrical Engineering
Josip Juraj Strossmayer University of Osijek
Kneza Trpimira 2b
31000 Osijek, Croatia
Phone: +38531224600,
Fax: +38531224605,
e-mail: ijeces@etfos.hr

International Journal of Electrical and Computer Engineering Systems
ISSN 1847-6996